FUEL REFORMATION AND HYDROGEN GENERATION IN DIRECT DROPLET IMPINGEMENT REACTORS

A Dissertation
Presented to
The Academic Faculty

by

Mark Jordan Varady

In Partial Fulfillment
of the Requirements for the Degree
Doctor of Philosophy in the
School of Mechanical Engineering

Georgia Institute of Technology
December 2010

FUEL REFORMATION AND HYDROGEN GENERATION IN DIRECT DROPLET IMPINGEMENT REACTORS

Approved by:

Dr. Andrei G. Fedorov, Advisor
School of Mechanical Engineering
Georgia Institute of Technology

Dr. F. Levent Degertekin, Advisor
School of Mechanical Engineering
Georgia Institute of Technology

Dr. Alexander Alexeev
School of Mechanical Engineering
Georgia Institute of Technology

Dr. Tom Fuller
School of Chemical & Biomolecular Engineering
Georgia Institute of Technology

Dr. Christopher W. Jones
School of Chemical & Biomolecular Engineering
Georgia Institute of Technology

Date Approved: November 4, 2010

ACKNOWLEDGEMENTS

I would like to first thank my wife, Christine Varady, for her steadfast support and sacrifice throughout my graduate studies. Without her none of my accomplishments would have been possible.

Secondly, my most sincere gratitude and respect go to my thesis advisor Andrei Fedorov, who provided outstanding technical guidance throughout my time as a graduate student, which fostered my growth as an engineer and researcher. More importantly, he proved to be a great mentor and friend, who provided valuable advice and support when I needed it the most.

Finally, I would like to acknowledge the many fellow students and labmates with whom I have formed lasting bonds and who enriched my experience at Georgia Tech.

TABLE OF CONTENTS

Page

LIST OF TABLES

Page

LIST OF FIGURES

Page

LIST OF SYMBOLS AND ABBREVIATIONS

Symbols

c_p	specific heat [J/kg-K]
C	molar concentration [gmol/m^3]
D	mass diffusion coefficient [m^2/s]
f	frequency of droplet injection into reactor [1/s]
ΔH^0_{298}	heat of reaction at standard conditions [kJ/mol]
H_{cell}	distance from droplet injection location to catalyst interface [m]
H_{cat}	thickness of catalyst bed in axial direction [m]
$h_{f,c}$	depth of penetration of accumulated liquid film into catalyst [m]
$h_{f,g}$	thickness of accumulated liquid film outside of catalyst [m]
$\dot{m}_d$	mass flow rate of droplet stream injected into DDIR unit cell [kg/s]
$\dot{m}_{ev,d}$	total evaporation rate from a single droplet [kg/s]
$\dot{m}_{ev,d,i}$	evaporation rate of species *i* from a single droplet [kg/s]
q_c	convective heat transfer rate to droplet [W]
q''	heat flux applied at catalyst interface [W/m^2]
Q_T	total heat rate applied to DDIR unit cell [W]
r	radial coordinate [m]
r_I	volumetric reaction rate for reaction *i* [gmol/m^3-s]
R	radius [m]
T	temperature [K]
u	gas phase axial velocity [m/s]
V	velocity [m/s]
w	gas phase radial velocity [m/s]
W/F	ratio of catalyst mass to molar flow rate of fuel [kg-s/gmol]
x_i	mole fraction of species *i*
y_i	mass fraction of species *i*
z	axial coordinate

Greek Letters

γ	activity coefficient
ε	porosity (void fraction) in catalyst bed [m^3/m^3]
λ	fraction of methanol undergoing steam reforming reaction
μ	dynamic viscosity [kg/m-s]
ν	kinematic viscosity [m^2/s]
ν_{ik}	stoichiometric coefficient of species *i* in reaction *k*.
ρ	mass density [kg/m^3]
ω	power density [kW/cm^3]

Subscripts

cell	Refers to DDIR unit cell
d	Refers to droplet
ev	Refers to evaporated or vaporized liquid
f	Refers to accumulated liquid film at catalyst interface
g	Refers to gas phase
int	Refers to catalyst interface
l	Refers to liquid phase
s	Refers to solid phase (catalyst particles)
sat	Refers to saturation conditions
w	Refers to DDIR unit cell boundary

Abbreviations

AR	aspect ratio (H_{cat}/R_{cell})
DDIR	Direct Droplet Impingement Reactor
MPOX	Methanol Partial Oxidation
MSR	Methanol Steam Reforming
PFR	Plug Flow Reactor

SUMMARY

Research into hydrogen fuel cells as a portable power source has increased significantly over the past decade as demand for higher energy density sources has risen. However, the difficulties and dangers associated with transporting hydrogen in highly compressed form has led to the idea of on-board reforming of hydrogen rich, high energy density liquid fuels. Experimental studies have largely focused on miniaturizing large scale unit operations reactor designs, which proves inadequate for smaller scale portable applications ranging from 1 – 1000 W. In these applications size minimization is among the most critical design goals, and the concept of multifunctional reactors in which the various components are intimately coupled and carry out multiple unit operations has proven fruitful. Such a reactor is studied in this work and is dubbed a direct droplet impingement reactor (DDIR). Here, the liquid fuel is delivered by a regularly spaced array of droplet generators, which have dual functions of atomization and fuel pumping. The droplets impinge, vaporize, and react on a heated catalyst layer, which acts as both the fuel vaporizer and reaction chamber.

Previous studies have investigated similar reactor designs, but with irregular sprays of droplets, making a rational study of the reactor performance near impossible. Precise control over droplet characteristics and regular spacing of the array has led to the idea of studying the DDIR on a unit cell basis. A theoretical model of the DDIR unit cell is developed, which considers the coupled processes of 1) droplet transport, heating, evaporation, and impingement with 2) liquid accumulation, capillary penetration, and vaporization on the heated catalyst interface, and 3) gas phase transport and reaction. The

components of this model are validated by comparison with relevant literature results. Furthermore, an experimental apparatus approximating a unit cell of the DDIR is used to directly compare against model predictions, providing additional confidence in the validity of the model.

A demonstration unit of the DDIR for methanol steam reforming capable of supplying a 100 W fuel cell is constructed and tested. Comparison with literature results confirms the viability of the DDIR concept in comparison with other proposed portable reformers at this scale. Additionally, stable autothermal reforming of methanol is demonstrated.

Using methanol steam reforming as a case study, the unit cell model is used to investigate the effects of various parameters on the reactor performance. Specifically, the influence of the unit cell aspect ratio, throughput, droplet parameters, and heat losses are investigated. The interplay between back diffusion of products and thermal resistance in the catalyst bed suggests an optimal design configuration that maximizes selectivity to the steam reforming reaction. It is also found that to avoid hotspots, a given reactor throughput should be achieved using unit cells with the lowest practically achievable throughput. Criteria for droplet impingement are also developed, which is critical for proper operation of the reactor and also place limitations on the minimum unit cell throughput depending on the capabilities of the droplet generator. Finally, possible directions for future research are made on both the experimental and modeling fronts.

CHAPTER 1

INTRODUCTION

Increasing power demands from portable electronic devices has sparked numerous investigations into improving the energy density of portable power sources over that of state of the art battery technology [1]. One approach has been to improve battery technology by refining existing devices, particularly lithium ion batteries [2-4]. Portable hydrogen fuel cells have also received a lot of attention, but the low volumetric energy density of hydrogen gas severely limits the application of this technology [5]. To improve the energy density, the hydrogen can be carried in the form of a metal hydride [6] or a liquid hydrocarbon [7-19] and released on board as demanded by the electronic device(s). This work focuses on a novel method for portable catalytic reforming of liquid fuels by atomizing the liquid with precise control over droplet characteristics, having the droplets impinge in a well controlled manner on a heated catalyst to react and produce hydrogen. This fuel reforming technology is dubbed a direct droplet impingement reactor (DDIR).

Many proposed portable liquid fuel reforming methods are simply scaled down versions of a traditional large scale unit operations reactor as shown schematically in Figure 1.1 [20-23]. In this approach, the primary design goal is to maximize the energy efficiency of the system. However, in portable systems minimizing overall size is a primary design goal, and this often conflicts with maximizing component efficiency, as shown by Mitsos et al. [24]. To address this design challenge, the concept of multifunctional reactors, in which a single component accomplishes two or more

functions, has been put forward to reduce system size and to simplify the design [25]. This is done in the DDIR by using the catalyst as both the reaction chamber and fuel vaporizer, and a fuel ejector that simultaneously atomizes and pumps the fuel. Others have investigated similar reactor designs, most notably the work by Schmidt's group at the University of Minnesota [26, 27]. However, poor control over the droplet characteristics in these studies prevented a careful empirical examination of the influence of operating parameters, and rational design of this reactor. By achieving superior control over droplet characteristics, not only are empirical studies facilitated, but a theoretical model can be developed to predict and optimize reactor performance.

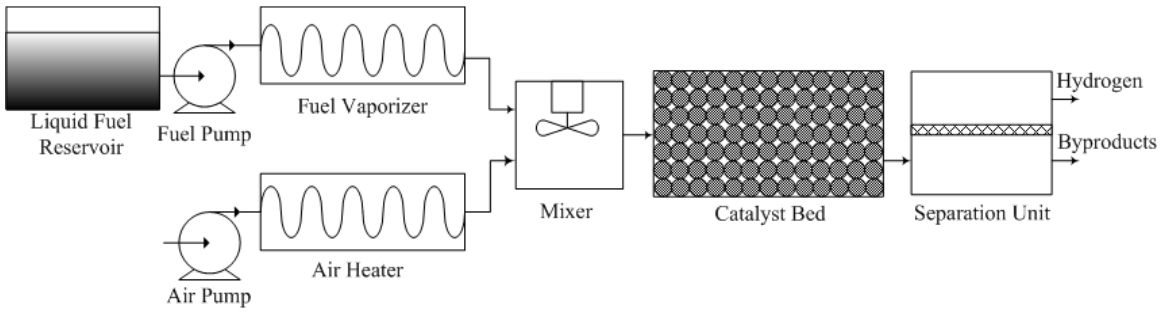

Figure 1.1. Schematic of unit operations reactor for hydrogen generation from a liquid hydrocarbon fuel.

As a case study for the DDIR this thesis focuses on methanol steam reforming, which is widely studied as one of the most viable methods for distributed hydrogen generation [28] because of its relatively mild reforming conditions. Of primary importance for reactor design is development of comprehensive regime maps showing how the controllable parameters translate to the particular mode of reactor operation and corresponding performance. This in turn is supported by experimental evidence showing the utility of these maps in DDIR design. The tools developed in this thesis are general

enough for application of the DDIR reactor design to a wider range of reactions in which a liquid feed is vaporized and converted over a solid catalyst.

Chapter 2 reviews the state of the art in portable fuel reforming devices. The DDIR concept is explained with a focus on how it addresses shortcomings of previous fuel reforming devices and how it enables the execution of a careful parametric study. Most importantly the reactor can be conceptualized as an array of unit cells, each consisting of its own droplet generator, which enables scaling by adding or subtracting unit cells to match a particular application. Additionally, several possible embodiments of the reactor design are presented in connection with possible applications.

A detailed model of a unit cell of the DDIR is developed in Chapter 3. This model consists of three major parts: the transit of the droplet to the catalyst layer, impingement of the droplet and accumulation/vaporization of liquid at the catalyst interface, and gas phase transport and reaction, which are all intimately coupled to each other. A multi-level iterative method for model solution is also outlined and implemented using the commercial computational fluid dynamics software Fluent.

The validation of the model results is presented in Chapter 4. The main processes of droplet transport, film accumulation and capillary penetration into the catalyst bed, and gas phase transport and reaction are compared to relevant literature results. Additionally, an experimental apparatus designed to approximate a unit cell of the reactor is described along with the stroboscopic technique used to visualize the droplet impingement and film growth. Experiments are performed showing droplet transport, film growth, and reaction under various conditions and compared to model results. Finally, a bench scale DDIR constructed from an ultrasonic atomizer array and an electrically heated catalyst bed is

employed to generate hydrogen sufficient to supply a 100 W fuel cell. Autothermal operation is also demonstrated.

In Chapter 5 the performance of the DDIR in steady-state operation is investigated using the model implementation described in Chapter 3. The influence of operating parameters including unit cell aspect ratio and throughput are investigated. Reactor performance is gauged using several performance metrics such as conversion, selectivity, and power density while considering design tradeoffs. Recommendations are also made regarding droplet delivery parameters to achieve a desired throughput.

Chapter 6 summarizes this thesis work including the original contributions to the field of portable fuel reforming and the most important conclusions drawn from both the experimental and modeling work. Finally, possible directions for future research are suggested.

CHAPTER 2

PORTABLE FUEL REFORMING AND CONCEPT DEVELOPMENT

2.1 Review of Portable Fuel Reforming Devices

Distributed hydrogen production from high energy density liquid fuels has received much attention over the past decade primarily because of the various potential uses of hydrogen fuel cells in automobiles [28-30], military field operations [8, 15], and portable consumer electronics [1, 31]. The basic functions of such a portable fuel reformer are to 1) store the fuel, 2) feed the fuel to the reaction chamber, 3) vaporize the fuel, and 4) convert the fuel to hydrogen, all within a compact package commensurate with the overall size of the devices that are being powered. Auxiliary functions such as incorporating a CO cleanup reactor stage [32, 33] and catalytic combustion of some of the generated hydrogen for heat supply [34] are also possible. Relevant design considerations for such systems are discussed along with some specific examples of portable fuel reforming devices from the literature.

2.1.1 Selection of Fuel and Reaction Pathway

Many liquid hydrocarbon fuels have been considered for supplying portable hydrogen fuel cells including ethanol [35], octane [13], and diesel and jet fuel [28]. The primary reaction pathways to hydrogen for these fuels are steam reforming and partial oxidation over Ni or Ni/Pd catalysts at temperatures above 700^{o}C [36]. As a result of the high temperature at which these reactions proceed, a large amount of CO is present in the product stream, which is a poison for the PEM fuel cell anode catalyst [9]. Additionally,

the high operating temperature leads to increasingly significant heat losses as the size of the system decreases and the surface area to volume ratio increases.

Methanol offers the advantages of high volatility, low reaction temperatures, and high H/C ratio compared to the above mentioned fuels and thus has been the most widely studied for distributed hydrogen production [37-39]. Again, the two primary competing reaction pathways for distributed conversion of methanol to hydrogen are steam reforming (MSR) and partial oxidation (MPOX), each offering their own unique advantages.

$$\text{MSR: } CH_3OH+H_2O \rightleftharpoons 3H_2+CO_2 \quad \Delta H^0_{298} = 49.5 \text{ kJ/mol} \tag{2.1}$$

$$\text{MPOX: } CH_3OH+ \tfrac{1}{2}(O_2+3.76N_2) \rightleftharpoons 2H_2+CO_2+1.88N_2 \quad \Delta H^0_{298} = -192 \text{ kJ/mol} \tag{2.2}$$

Both of these reactions are carried out via heterogeneous catalysis usually over a fixed bed of $CuO/ZnO/Al_2O_3$ particles [40], although other catalyst formulations have demonstrated high activity such as Sn-Mo-O for partial oxidation [41] and Pd/ZnO for steam reforming [42]. Partial oxidation is exothermic and autothermal operation has been demonstrated [43], whereas steam reforming requires additional external heat input to vaporize the water in the feed as well as drive the endothermic reaction. However, steam reforming yields more hydrogen per unit of fuel consumed and its products are not diluted by excess nitrogen as in partial oxidation, which requires air. This is important for efficient on-the-spot removal and storage of carbon dioxide from the product stream, which has recently been proposed to counteract the increasing levels of atmospheric greenhouse gases [44]. Combining steam reforming and partial oxidation in what is termed autothermal reforming or oxidative steam reforming has also been demonstrated [43, 45].

Methanol decomposition (MD) and water gas shift (WGS) are the two secondary reactions that must be considered in either steam reforming or partial oxidation of methanol.

$$\text{MD: } CH_3OH \rightleftharpoons 2H_2 + CO \quad \Delta H^0_{298} = 90 \text{ kJ/mol} \tag{2.3}$$

$$\text{WGS: } H_2O + CO \rightleftharpoons H_2 + CO_2 \quad \Delta H^0_{298} = -47 \text{ kJ/mol} \tag{2.4}$$

These reactions account for the appearance of carbon monoxide in the products, which is found to increase from 1-2% at bed temperatures around 200^{o}C to over 10% above 320^{o}C [46]. Above 300^{o}C, catalyst deactivation accelerates rapidly due to sintering [47, 48] and the catalyst is unusable for long periods at these elevated temperatures.

The discussion from this point forward will focus solely on methanol reforming and some important design considerations are investigated.

2.1.2 Heat Supply

External heat input is required to vaporize the liquid fuel feed and drive the endothermic steam reforming reaction. One option is to route some of the electrical power generated by the fuel cell into resistance heaters in thermal contact with a vaporizer and reaction chamber. Pattekar and Kothare and Shin and Besser [49] both utilized microfabrication processes to pattern Pt resistance heaters on a substrate with microchannels etched on the opposite side. The liquid feed was vaporized and reacted in these microchannels and good control over the reactor temperature was demonstrated. It should be noted that in both of these cases, the reactors were not integrated with a fuel cell and so it is assumed the electricity was supplied from the wall. Consideration must also be given to the variation in heating load over the reactor because the reaction rate,

and thus the rate of heat consumption, is greatest at the reactor inlet and decreases dramatically towards the reactor outlet. To minimize temperature gradients in the reactor, it is necessary to spatially match the heat dissipated in the electrical heater with that consumed in the reaction by a) varying the spatial density of the heaters, and/or b) varying the heater resistance by decreasing the conductor cross-sectional area in regions of high heat load.

Another approach is to supply the required heat from exothermic chemical reaction. For autothermal reforming, it is possible to adjust the feed ratios such that the amount of heat generated is sufficient to both vaporize the feed and to drive the steam reforming reaction. Assuming that a fraction, λ, of the molar flow rate of methanol, $\dot{n}_M$, undergoes steam reforming, overall energy conservation for an autothermal reforming reactor gives

$$\begin{aligned}&(1-\lambda)\dot{n}_M \Delta H_{MPOX} = \\ &\sum_{i=M,W} \dot{n}_i \left[h_{fg} + c_{p,l}\left(T_{sat} - T_f\right) + c_{p,g}\left(T_{rxn} - T_{sat}\right) \right]_i + \lambda \dot{n}_M \Delta H_{MSR} + q_{loss}\end{aligned} \tag{2.5}$$

where the subscripts M and W denote methanol and water respectively, and q_{loss} is the heat lost to the surroundings. Along with the stoichiometric relations $\dot{n}_W = \lambda \dot{n}_M$, $\dot{n}_O = 0.5(1-\lambda)\dot{n}_M$, and $\dot{n}_{air} = 4.76\dot{n}_O$, the quantities λ, $\dot{n}_W$, and $\dot{n}_{air}$ can be calculated for a desired throughput. Successful implementation of this scheme requires good thermal contact between the reaction chamber and vaporizer.

Another approach considered for methanol steam reforming is to catalytically combust a portion of the methanol feed in a separate reaction chamber thermally contacted with the steam reforming chamber. Stefanidis and Vlachos [50] performed a

detailed numerical study of methanol steam reforming and catalytic combustion in co-current flow in two channels separated by a wall. By using a co-current flow configuration, the spatial regions of high heat generation and high heat consumption are matched. This study determined appropriate catalyst loadings and feed rates in both channels to maintain the reactor operating temperature for a desired throughput. Kawamura et al. [21] constructed a layered microchannel reactor in which a methanol catalytic combustor is sandwiched between a methanol steam reformer and a fuel vaporizer. Experimental characterization of this reactor showed control over the operating temperatures of the reformer and vaporizer via the supply rate to the methanol catalytic combustor.

Since not all of the hydrogen generated by the liquid feed is utilized by the fuel cell (80% utilization is typical), many researchers have attempted to catalytically combust the unused hydrogen to supply heat to the reactor. Such a methanol steam reformer coupled with a hydrogen catalytic combustor was constructed by Kim [34], producing enough hydrogen to power a 4.5 W PEM fuel cell. In these experiments, the hydrogen supplied to the reactor was set equal to the estimated unutilized hydrogen for the given flow rate of methanol (2 ml/h). It should be noted however, that the hydrogen was supplied from a pressurized cylinder and not from the actual products from the steam reformer. Schuessler et al. [51] integrated a carbon monoxide and hydrogen oxidation stage with a methanol autothermal reformer and vaporizer. This reactor consisted of two layers such that the vaporizer and oxidation stage were adjacent to each other and the heat from the oxidation went into vaporizing the liquid feed. In this case, oxidation of the products occurs before feeding to the fuel cell, so it is critical to control the oxygen feed

to control consumption of the hydrogen rich feed before reaching the fuel cell.

2.1.3 Elimination of CO in Products

Because CO is a poison to the fuel cell anode at very low concentrations (~ 100 ppm), it is necessary to take steps to reduce CO concentration from the 2-3 mol % expected at typical reactor operating conditions. A common solution to this problem is to preferentially oxidize CO over a platinum based catalyst to reduce the CO concentration to below 100 ppm while leaving the hydrogen unreacted. For example, Pan and Wang [52] integrated a multi-stage CO preferential oxidation (PrOX) reactor consisting of a monolithic Pt catalyst following a methanol steam reformer. In their experiments, it was demonstrated that the CO concentration was reduced from ~ 2% at the outlet of the reformer stage to about 20 ppm at the outlet of the preferential oxidation reactor.

Another interesting solution is to incorporate a selectively permeable membrane in the reaction chamber to remove the hydrogen at the point of production, so that none of the CO in the products makes it to the fuel cell anode. These so-called membrane reactors provide the added benefit of increased conversion rates so that a smaller reactor volume can be used for a given throughput. Most often, the hydrogen selective membrane is a metallic alloy consisting of 77% Pd/23% Ag. Nair and Harold [53] presented a steam reforming reactor consisting of a packed bed of catalyst particles with an interspersed array of tubes, each of which is comprised of a porous support with a thin film of Pd on its outer edge. The results clearly show an increase in methanol conversion over a normal packed bed reactor of the same volume operated under identical conditions.

2.1.4 Liquid Feed Delivery Method

A significant challenge in all of the above described fuel processors is the liquid

fuel delivery method, and integration of this component has largely been neglected in the literature. Typically, a syringe pump is used when testing fuel reformers in the laboratory, which is not a realistic solution for smaller scale applications due to its disproportionately large size compared to the overall system. Even with the flow control offered by a syringe pump, the vaporizing liquid feed in small channels creates large pressure drops and flow rate oscillations that lead to significant variations in the feed flow rate. Kandlikar offers an excellent review of this problem and identifies the formation of confined, stabilized vapor slugs in microchannels as the primary cause of these problems [54]. This challenge can be addressed by including a section of large pressure drop upstream of the vaporizing section, so that the fluid is pushed downstream. For example, Pattekar and Kothare [55] modified their original microchannel reactor design so that the liquid flows radially outward as it boils and the flow cross-section continuously increases.

The solution to this problem presented by the DDIR is an example of a multifunctional reactor in which two or more unit operations are synergistically integrated into a single component. Specifically, this is accomplished by bringing the liquid feed, heat supply, and entrance to the catalyst bed to the same location. In other words, for reactions involving heterogeneous catalysis of a vaporized liquid feed over a fixed porous solid bed, multifunctionality can be achieved by atomizing the liquid feed followed by liquid vaporization directly on the hot catalyst bed. This solves the problem of flow instabilities caused by vaporizing the liquid feed in small channels since the liquid is vaporized directly at the catalyst surface and is not constrained inside a channel. Variations on this concept have been studied for a few applications. The most

commercially successful example is that of a fluid catalytic cracking (FCC) riser reactor, in which a heavy hydrocarbon fuel is sprayed into a fluidized bed of heated catalyst particles where collisions cause the fuel droplets to rapidly vaporize and react on the catalyst particle surface. Control of droplet size distribution is a major issue since this determines vaporization rate, and thus conversion and selectivity [56, 57]. Another example in an early phase of development is catalytic combustion of liquid hydrocarbons as a portable power source by electrospraying directly onto a catalyst coated mesh [58, 59]. The primary problem with electrospraying is the high voltage required (> 1 kV), which could present a problem for small-scale portable applications.

An example of a DDIR-type design for generating hydrogen from liquid fuels is one developed by Schmidt's group at the University of Minnesota, in which a standard automotive fuel injector sprays liquid hydrocarbon fuels directly onto a catalyst plug. Schmidt has termed this process "reactive flash volatilization". The reactor was used for autothermal partial oxidation of ~400 μm diameter droplet sprays of ethanol [27, 60], soy-oil, and glucose-water solutions [26] mixed with air over Rh-Ce catalyst supported on alumina foam. Experiments were carried out at various temperatures and air-fuel feed ratios, aiming to identify optimal conditions for both conversion and selectivity. The authors also stress the need to improve modeling of the droplet impingement, vaporization and reaction processes to gain better fundamental understanding and control reactor performance. However, the automotive fuel injector used in these experiments is inadequate because the wide droplet size distribution, spray angle, and irregularity of impingement location makes it difficult to carry out a rational study of the effect of the various operating parameters on reactor performance.

The reactor studied in this work requires exactly this precise control over droplet size, velocity, impingement location and angle, enabling model development to study the effect of various operating parameters on reactor performance. Any modeling effort must be accompanied by supporting experiments to gain confidence in the validity of the model and to provide practical relevance of the simulation results. The ultrasonic atomizer array designed by our research group [61-63] achieves the desired control over droplet characteristics while operating at low power in a compact package. This device, shown in Figure 2.1, operates by piezoelectric excitation of a liquid filled cavity at one of its resonance frequencies. The resulting standing pressure wave created in the fluid is amplified by pyramidal nozzles, creating a large pressure gradient at the nozzle exit, forcing ejection of liquid droplets at the operating frequency. The orifice size at the nozzle exit controls the droplet size, giving excellent control over droplet diameter, and the droplet velocity is controlled by the voltage applied to the piezoelectric transducer. Additionally, liquid pumping action has been demonstrated with this device, drawing liquid from a larger secondary storage tank into the reservoir inlet during operation. Thus, this atomizer comprises a complete solution to the fuel delivery problem.

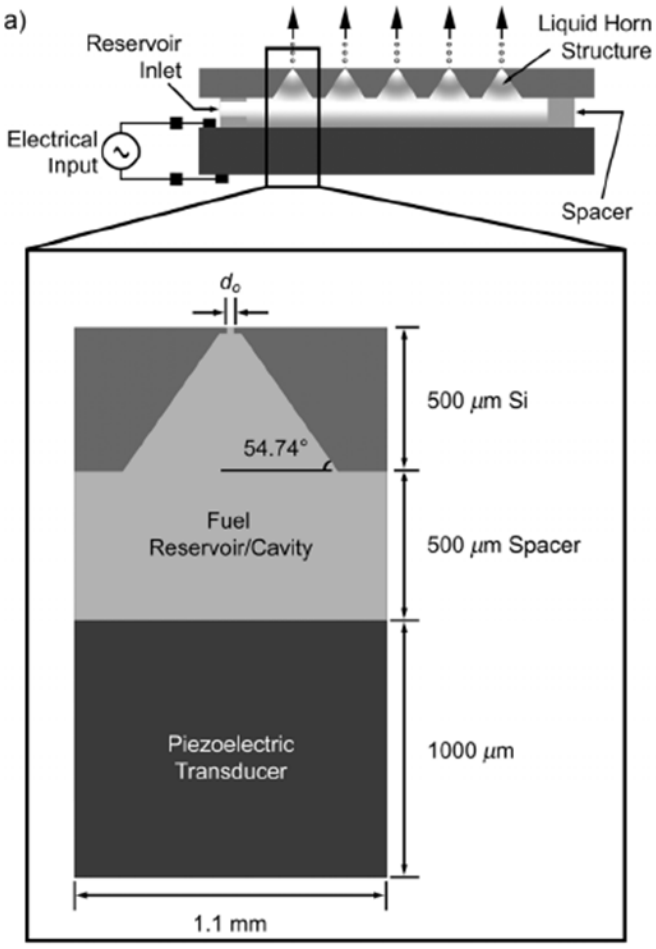

Figure 2.1. Schematic of ultrasonic atomizer array.

2.2 DDIR Design Concept and Specific Embodiments

Three basic components comprise the general DDIR: a liquid fuel reservoir, a droplet generator, and the catalyst layer. This is amenable to a simple layered design that can be easily manufactured in a compact package. The key feature is the array of droplet generators, which must produce a regular pattern of monodisperse droplets at a precise rate for maximum control over reactor performance. This results in a structure in which each droplet generator comprises a unit cell of the overall reactor. Scalability is then enabled by adding or subtracting the number of unit cells of the reactor. Furthermore, the reactor can be modeled and studied on a unit cell basis, leading to a significantly

simplified design approach. Using this basic design as a template, the reactor can be customized for a specific reaction by adding required components.

The simplest embodiment described above is shown in Figure 2.2a, and this layered structure can be generalized to incorporate multiple catalyst layers separated by impermeable, selectively permeable, or completely permeable walls as show in Figure 2.2b. This layered structure also allows for introduction of gaseous species to particular locations by means of a delivery tube, which is perforated at the desired delivery point.

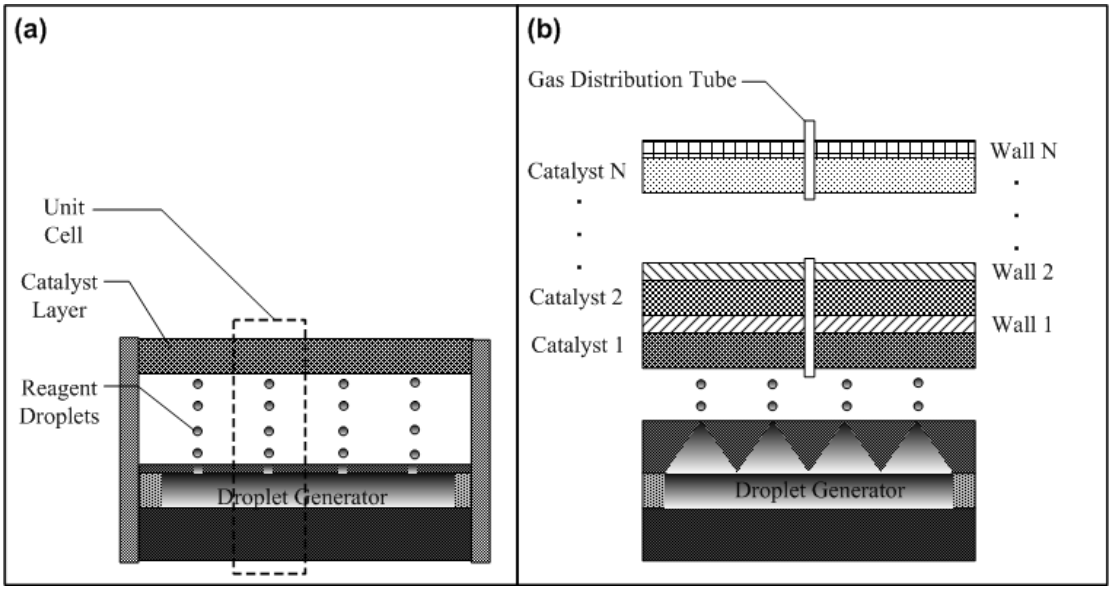

Figure 2.2. (a) Simplest embodiment of DDIR reactor consisting of array of droplet generators and heated catalyst layer. (b) Generalized embodiment of DDIR with multiple catalyst layers each separated by wall layers with different properties, and gas supplied to selected layers with a gas distribution tube.

Consider using a preferential oxidation (PrOX) reactor stage after methanol steam reforming to reduce the small amounts of CO to acceptable level. Here, a PrOX catalyst layer lies directly on top of the MSR catalyst layer as shown in Figure 2.3(a). The required oxygen is delivered via air intake through the delivery tube to the PrOX catalyst layer. In Figure 2.3(b) a hydrogen selective membrane is placed on top of the MSR

catalyst layer to remove the hydrogen as it is generated within the catalyst. In this particular embodiment, the reaction byproducts (primarily CO and CO_2) exit the reactor laterally.

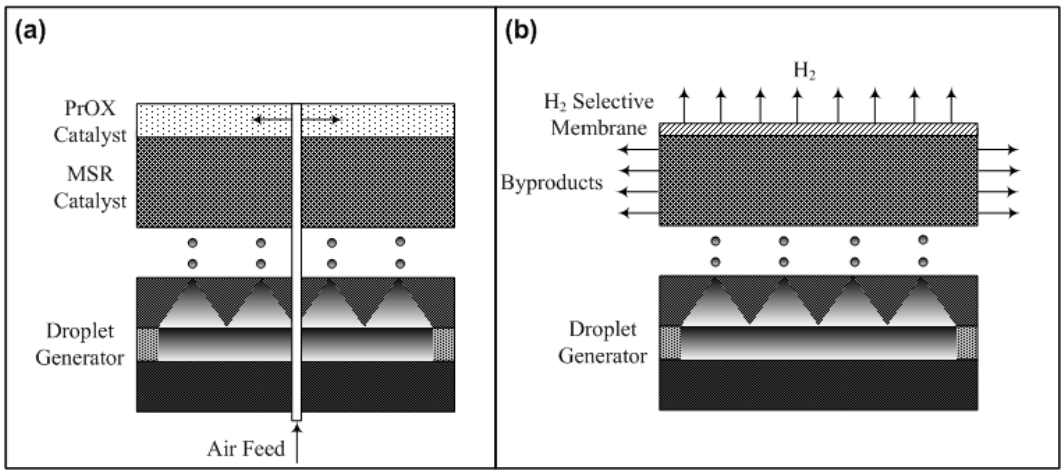

Figure 2.3. Examples of DDIR reactor designs for elimination of excess CO from MSR. a) use of a PrOX catalyst layer with air introduction, b) use of hydrogen selective membrane.

Another method for introducing gaseous species into the reactor is to intersperse gas delivery channels with the liquid nozzles of the droplet generator as shown in Figure 2.4, which improves the distribution and mixing of gaseous reagents. In Figure 2.4(a), the mixing occurs in the space between the droplet generator and catalyst surface. This configuration could be employed, for example, in autothermal reforming or partial oxidation of methanol in which air (or pure oxygen) must mix with the vaporized reagents immediately at the catalyst interface. Alternatively, the gaseous reagents can be directed along an array of distribution tubes that travel through the catalyst layers where they are released at the desired location as shown in Figure 2.4(b). Again, this configuration could be employed for selectively introducing air to a PrOX catalyst layer with an improved spatial distribution of the gaseous reagents.

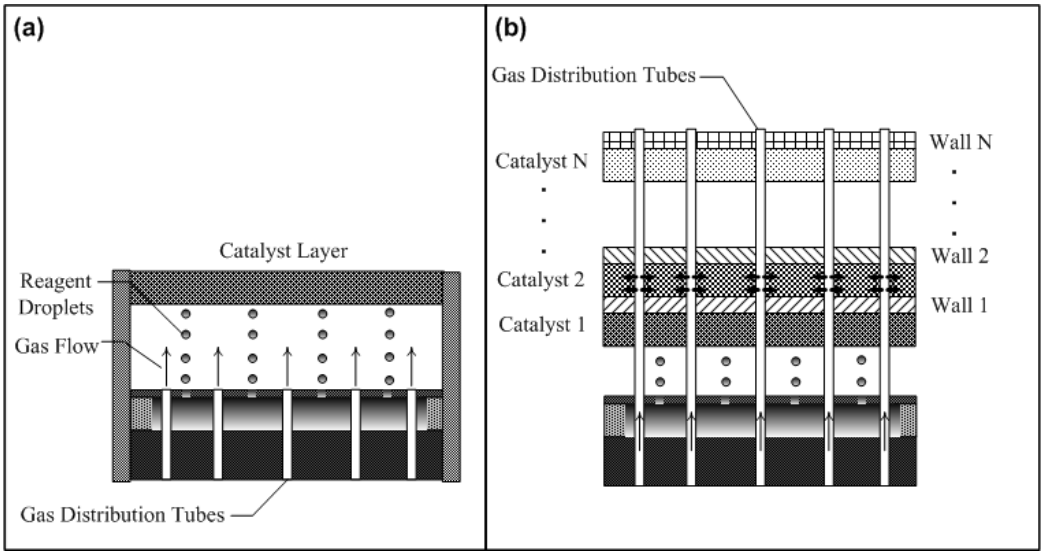

Figure 2.4. Improved distribution of gaseous species in DDIR. (a) Gas released at same plane as droplets. (b) Gas distribution tubes extend up into the catalyst layer(s) with gas selectively released at desired location(s).

Heater deployment is another important design consideration for the DDIR. One option is to deploy an electrical heater at the plane of droplet impingement on the catalyst layer to vaporize the impinging droplets as shown in Figure 2.5(a). This heater can also supply heat to the adjacent catalyst if an endothermic reaction is occurring. However, if the thermal conductivity of the catalyst layer is low or the layer is relatively thick, significant temperature gradients can result, negatively effecting reactor performance. To alleviate this, heaters can also be deployed throughout the catalyst layer as shown in Figure 2.5(b). One way to do this is to use a separate catalyst filled tube heated at the periphery for each unit cell. In this arrangement, the interface heater is dedicated to vaporizing the impinging droplets and the periphery heaters handle the heat load for the reaction. Since heat is provided locally to each unit cell, temperature gradients in the catalyst layer are avoided. Such heater arrangements would even be useful for startup of autothermal reactions where the heaters would only be powered when needed and turned off once reaction is supplying sufficient heat to be self-sustaining.

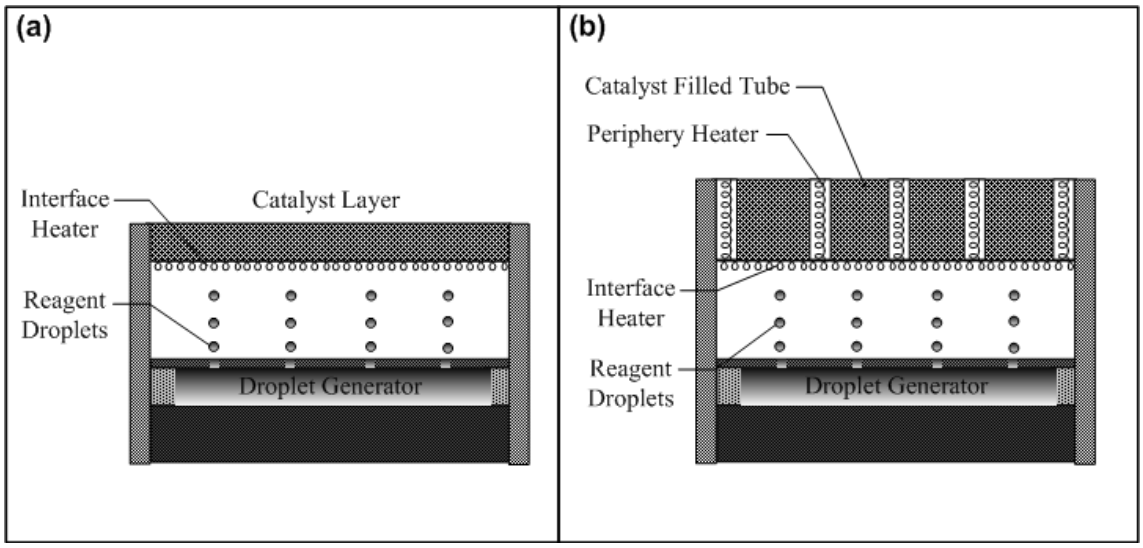

Figure 2.5. Deployment of electrical heaters in DDIR (a) Heater deployed along catalyst interface for vaporizing impinging droplets. (b) Additional heaters deployed in catalyst layer.

Another way to supply heat for an endothermic reaction is to carry out an exothermic reaction in adjacent cells as shown in Figure 2.6(a). In this embodiment, there are separate feeds for the exothermic and endothermic unit cells, which are separated by impermeable boundaries, but are in good thermal contact. In this configuration, the spatial regions of high heat generation and high heat consumption are at the catalyst interface.

A concept for integration of the fuel cell anode with the reaction chamber is depicted in Figure 2.6(b). Here, tubes consisting of a supported hydrogen permeable membrane outer wall are deployed within the catalyst bed, similar to the configuration described in [53]. However, in this embodiment, the fuel cell anode features interdigitated fingers that extend into the membrane coated tubes so that the hydrogen can react directly at the point of permeation.

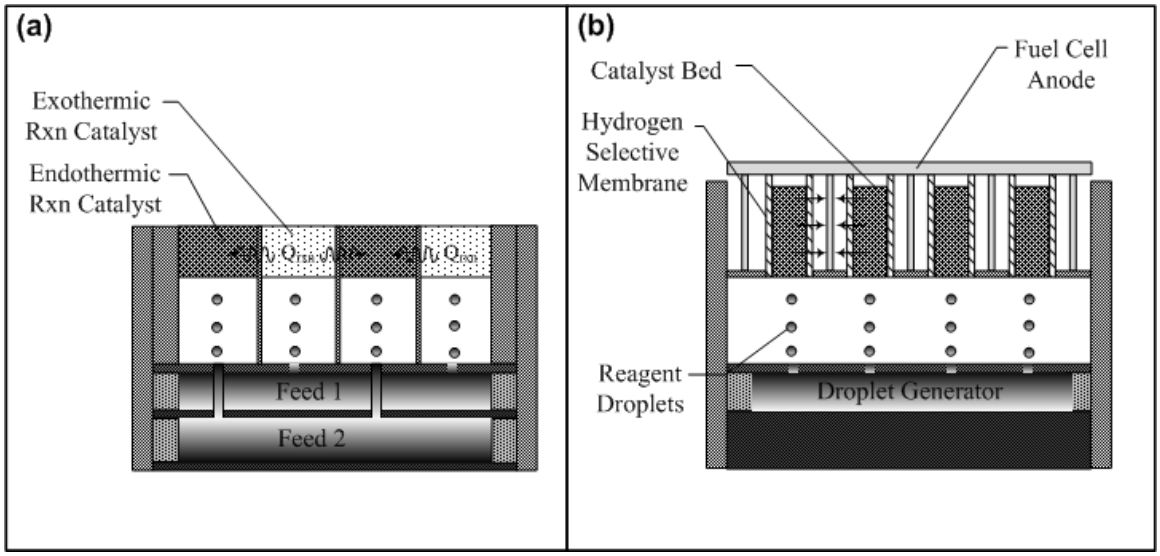

Figure 2.6. (a) Heat supply for endothermic reaction from adjacent cells in thermal contact executing exothermic reaction. Boundaries are impermeable so there is no mixing of chemical species between adjacent unit cells. (b) Integration of hydrogen selective membrane in interior of catalyst bed with interdigitated fuel cell anode directly at hydrogen permeation location.

2.3 Identification of Processes Occurring in DDIR

Before developing a detailed model of the DDIR, the processes occurring in the reactor must be identified along with the possible operating regimes. These processes are 1) droplet transit to the catalyst interface, 2) droplet impingement at the catalyst interface and accumulation of a liquid film, and 3) gas phase transport and reaction in the porous catalyst layer. These processes all influence one another, so that the model must consider the coupling between these processes in order to correctly predict performance.

As the droplets travel toward the catalyst interface they can lose some of their mass due to evaporation and have their trajectory altered by the surrounding gas phase flow. For example, if there is significant backward directed flow due to vaporization at the catalyst interface, a droplet can be deflected before impinging at the droplet interface. This phenomenon, known as the Leidenfrost effect, has been well documented in the literature [64-66]. Most studies of this effect have been confined to a single droplet under

the influence of gravity on a solid surface, although Chandra and Avedisian [67] have established the Leidenfrost temperature as 673 K for a single droplet on a porous alumina surface. The DDIR differs since there is a stream of droplets impinging, one after the other, so a higher interface heat flux would be necessary to maintain this temperature to keep each successive droplet from impinging on the catalyst interface. The motion of the droplet stream can also induce a flow in the gas phase not only due to evaporation, but also due to viscous forces. Thus, it is critical to consider the coupling between the droplet motion and evaporation and the flow in the gas phase.

If droplet impingement does occur, then several possibilities must be considered. First, it is possible that splashing of the liquid occurs, which could lead to loss of some of the liquid feed as it leaves the vicinity of the catalyst interface. Wachters and Westerling established the threshold above which splashing occurs as $We = 2\rho V^2 R/\sigma > 80$, and it is desirable to operate the reactor below this threshold. When the droplet impinges it is also subjected to greatly increased heat fluxes as a result of the liquid/solid thermal contact. If the heat flux into the droplet is sufficiently high, then the impinging droplet could completely vaporize before arrival of the next droplet, and this is termed flash evaporation. On the other hand, another droplet could impinge before the first is completely vaporized, leading to an accumulation of liquid at the catalyst interface. Since the liquid accumulates on a porous catalyst bed, capillary forces can also draw the liquid into the bed interior as the liquid is being vaporized. This complicated interplay between transport processes must be properly modeled to correctly predict reactor performance.

CHAPTER 3

MODEL DEVELOPMENT AND IMPLEMENTATION

This work is focused on the steady-state operation of the DDIR. However, a general transient model is first developed and then reduced to the steady state model case. This makes the model development logically easier to follow and it also lays the foundation for future transient studies. The steady-state model is implemented in the CFD software Fluent and validation studies are carried out independently for each major component of the model.

3.1 Model Formulation

The DDIR unit cell is represented by a two-dimensional axisymmetric model as shown in Figure 3.1 below. The unit cell has a uniform radius of R_{cell} and consists of a droplet transit zone of length H_{cell} and a catalyst layer of length H_{cat}, in which the reaction occurs. Droplets are introduced into the unit cell at the origin ($z = r = 0$) with given initial axial velocity, $V_{d,0}$, radius, $R_{d,0}$, and temperature, $T_{d,0}$, with a frequency, f. A droplet's distance from the ejection point is Z_d, and its velocity, V_d, can change due to drag and pressure forces, its radius, R_d, can change by evaporation, and its temperature, T_d, can change as heat is exchanged with the surroundings. In the scenario depicted in Figure 3.1, droplets impinge on the interface and a liquid film accumulates at the catalyst interface.

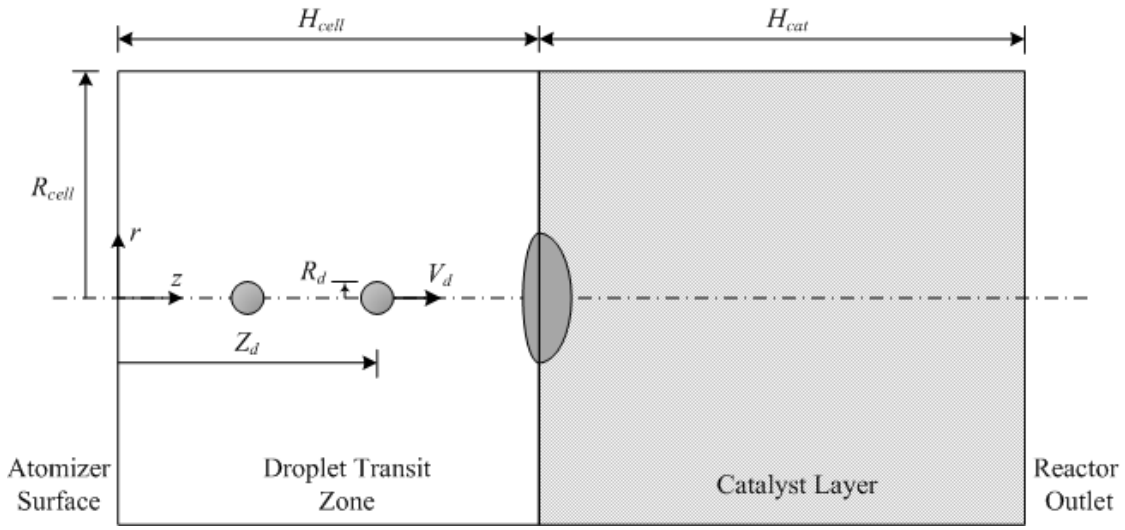

Figure 3.1. Schematic of DDIR unit cell used in developing model.

3.1.1 Droplet Transit Equations

A single droplet can be tracked from its ejection point at $z = r = 0$ with a set of 1st order ordinary differential equations assuming the droplet motion is one dimensional along the centerline of the unit cell, the droplet temperature is spatially uniform, and the droplet remains spherical.

$$\frac{dZ_d}{dt} = V_d \tag{3.1}$$

$$\frac{dV_d}{dt} = \frac{3F_d}{4\pi\rho_l R_d^3} \tag{3.2}$$

$$\frac{dR_d}{dt} = \frac{\dot{m}_{ev,d}}{4\pi\rho_l R_d^2} \tag{3.3}$$

$$\frac{dT_d}{dt} = \frac{3}{4\pi\rho_l c_{p,l} R_d^3}\left(q_c + \sum_i \dot{m}_{ev,d,i} h_{fg,i}\right) \tag{3.4}$$

$$Z_d(0) = 0, \quad V_d(0) = V_{d,0}, \quad R_d(0) = R_{d,0}, \quad T_d(0) = T_{d,0} \tag{3.5}$$

Here, F_d is the net force on the droplet, $\dot{m}_{ev,d}$ and $\dot{m}_{ev,d,i}$ are the overall and species i mass evaporation rates respectively, q_c is the heat transfer rate to the droplet from the

surroundings, $h_{fg,i}$ is the heat of vaporization of species i, ρ_l is the liquid density, and $c_{p,l}$ is the liquid specific heat.

The only forces on the droplet considered in this analysis are viscous drag and pressure forces from the surrounding gas phase with the gravitational force neglected. Taking the ratio of the drag force to the gravitational force gives a criterion for neglecting the gravitational force.

$$\frac{F_{grav}}{F_{drag}} = \frac{2}{9}\frac{\rho_l}{\rho_g}\left(\frac{R_{d,0}V_{d,0}}{\nu_g}\right)\left(\frac{gR_{d,0}}{V_{d,0}^2}\right) \sim \frac{\rho_l}{\rho_g}\frac{Re_d}{Fr^2} << 1 \tag{3.6}$$

For the cases considered in this work, the maximum droplet radius considered is 30 μm and a typical droplet velocity is 10 m/s, which gives $(\rho_l/\rho_g)(Re_d/Fr^2)$ = 0.08, which satisfies the criteria for neglecting gravitational force on the droplet. The force on a single droplet can then be written as follows.

$$F_d = -6\pi f_1 \mu_g R_d \left(V_d - u\right) - \frac{\partial p}{\partial z}\left(2R_d\right)\pi R_d^2 \tag{3.7}$$

Where u is the local z-component of gas velocity, p is the local gas pressure, and ρ_g is the gas density. The factor f_1 is a correction accounting for the effect of evaporating liquid and deviation from Stokes flow [68].

$$f_1 = \frac{1 + 0.0545\,Re_d + 0.1\,Re_d^{1/2}\left(1 - 0.03\,Re_d\right)}{1 + a\left|Re_e\right|^b} \tag{3.8}$$

Where Re_d is the droplet Reynolds number based on the velocity difference between gas and droplet: $Re_d = 2R_d\left|V_d - u\right|\rho_g/\mu_g$, Re_e is the droplet Reynolds number based on the velocity of the evaporating vapor leaving the droplet surface, $Re_e = 2R_d V_e \rho_g/\mu_g$, with $a = 0.09 + 0.077\,exp\left(-0.4\,Re_d\right)$, and $b = 0.4 + 0.77\,exp\left(-0.04\,Re_d\right)$. The velocity V_e is

given by the overall mass evaporation rate as $V_e = \dot{m}_{ev,d} \big/ 4\pi\rho_g R_d^2$. This correction is valid for $0 < Re_d < 100$ and $0 < Re_e < 10$.

The convective heat transfer from the gas to droplet, $q_c = f_2 h\left(4\pi R_d^2\right)\left(T_g - T_d\right)$, has a correction, $f_2 = \beta \big/ \left(e^{\beta} - 1\right)$, similar to the correction for drag to account for the effect of evaporating liquid [68]. The coefficient β is a dimensionless droplet surface area regression rate given by

$$\beta = -\frac{\rho_l c_{p,g}}{2k_g} \frac{d\left(R_d^2\right)}{dt} \tag{3.9}$$

The convective heat transfer coefficient, *h*, is given in terms of the droplet Nusselt number, $Nu_d = 2 + 0.552\, Re_d^{1/2}\, Pr_g^{1/3}$ [68]. Finally, the mass evaporation rate from the droplet, $\dot{m}_{ev,d}$, is given by the D^2-law [69] modified to include convective effects. The evaporation rate can be either heat transfer or mass transfer limited. The mass-transfer-limited case is described by Abramzon and Sirignano [70].

$$\dot{m}_{ev,d} = -2\pi R_d \rho_g D_g Sh_d \, ln\left(\frac{1 - y_{f,\infty}}{1 - y_{f,s}}\right) \tag{3.10}$$

where ρ_g is the average gas phase density between the droplet surface and far-field, D_g is the corresponding average diffusion coefficient, $y_{f,\infty}$ is the mass fraction of the fuel mixture in the far-field away from the droplet, $y_{f,s}$ is the mass fraction of the fuel mixture at the droplet surface, and $Sh_d = 2 + 0.552\, Re_d^{1/2}\, Sc_g^{1/3}$. For heat transfer limited evaporation, the rate is [70]

$$\dot{m}_{ev,d} = -2\pi R_d \frac{k_g}{c_{p,g}} Nu_d \, ln\left(\frac{c_{p,g}\left(T_\infty - T_d\right)}{h_{fg}} + 1 \right) \tag{3.11}$$

where k_g is the average gas thermal conductivity, $c_{p,g}$ is the average gas specific heat, and T_∞ is the far-field temperature of the gas surrounding the droplet. Note that the mass transfer limited evaporation law is only valid if the fuel surface mass fraction, $y_{f,s}$, is less than 1; that is if the droplet temperature is less than the saturation temperature of the fuel mixture. Once the droplet reaches the mixture saturation temperature, mass transfer can no longer limit the droplet evaporation process and $\dot{m}_{ev,d}$ is always heat transfer limited.

In this model the liquid droplet is a binary fuel mixture, so it is possible to have different evaporation rates for the two components. Sirignano [71] presents two limiting cases depending on the relative rates of droplet evaporation and species diffusion in the liquid, which bypasses the need to solve transport equations in the droplet interior. When fuel diffusion in the liquid is much faster than droplet evaporation, the composition throughout the droplet can be treated as uniform, but varying with time as the relative rates of evaporation of the two components is determined by their relative vapor pressures at the droplet surface. At the other extreme, droplet evaporation is much faster than component diffusion in the liquid, so that the composition in the droplet remains unchanged throughout the droplet lifetime. In this case, the liquid composition only varies in a very thin (vanishing in the limit) layer near the droplet surface. Since the composition doesn't vary in the bulk of the droplet, mass conservation requires the relative evaporation rates of each species to be in proportion to their initial concentrations. To determine what limit is applicable, time scales for liquid diffusion, τ_{ld}, and droplet evaporation, τ_{de}, are defined as follows:

$$\tau_{ld} = \frac{R_{d,0}^2}{D_l}, \qquad \tau_{de} = \frac{R_{d,0}^2}{K} \tag{3.12}$$

Where D_l is the diffusion coefficient in the liquid, and K is the evaporation constant in the D^2 law. For the case $\tau_{ld} >> \tau_{de}$, the evaporation rate of each species can change and depends on the species vapor pressure at the surface and liquid phase composition. For mass transfer limited evaporation, K is given by the following expression:

$$K = \frac{\rho_g D_g}{\rho_l} Sh_d \, ln\left(\frac{1 - y_{f,\infty}}{1 - y_{f,s}}\right) \tag{3.13}$$

If the droplet evaporation is heat transfer limited, then K is given by

$$K = \frac{k_g}{\rho_l c_{p,g}} Nu_d \, ln\left(\frac{c_{p,g}\left(T_\infty - T_d\right)}{h_{fg}} + 1\right) \tag{3.14}$$

The liquid diffusion coefficient of species A (e.g. A = methanol), $D_{l,A}$, is given by the following expression for concentrated non-electrolyte solutions [72]:

$$D_{l,A}\mu_m = \left(D_{AB}^0 \mu_B\right)^{x_B} \left(D_{BA}^0 \mu_A\right)^{x_A} \left(1 + \frac{\partial\left(ln\,\gamma_A\right)}{\partial\left(ln\,x_A\right)}\right) \tag{3.15}$$

Here, D_{AB}^0 is the diffusion coefficient for an infinitely dilute solution of species A in solvent B, x_A, γ_A, and μ_A are the mole fraction, activity coefficient, and viscosity of species A in the liquid (A + B) solution, respectively, and μ_m is the mean viscosity of the liquid solution.

Varanasi et al. [73] presented a method for calculating the evaporation rate of each species, $\dot{m}_{ev,d,i}$, in the droplet for the case $\tau_{ld} >> \tau_{de}$.

$$\dot{m}_{ev,d,i} = \dot{m}_{ev,d} \frac{y_{i,s}}{\sum_j y_{j,s}} \tag{3.16}$$

Here, the summation is only over those species contained in the liquid droplet. Assuming sufficiently low operating pressures, the gaseous species mole fractions at the droplet surface, $\chi_{i,s}$, can be calculated using the Clausius-Clapeyron equation to find the mole fraction if the droplet consists of pure i, $\chi^*_{i,s}$, coupled with Raoult's law, which is modified by the activity coefficient for the species in the liquid mixture.

$$\chi^*_{i,s} = \frac{p_{atm}}{p} exp\left[\frac{h_{fg,i}}{\Re_i} \left(\frac{1}{T_{sat,i}} - \frac{1}{T_d} \right) \right] \tag{3.17}$$

$$\chi_{i,s} = \gamma_i \chi_{i,l} \chi^*_{i,s} \tag{3.18}$$

Where $\Re_i$ is the ideal gas constant for species i, $T_{sat,i}$ is the boiling point of species i at standard atmospheric pressure, p_{atm}, and $\chi_{i,l}$ is the mole fraction of species i in the liquid droplet.

3.1.2 Gas Phase Conservation Equations

Turning attention to the gas phase, mass, momentum, heat, and species conservation equations must be solved in both the droplet transit zone and the porous catalyst layer. In the cylindrical coordinate system of the DDIR unit cell shown in Figure 3.1, species conservation satisfies the following equation in both zones.

$$\frac{\partial C_i}{\partial t} + \frac{\partial}{\partial z}\left(uC_i\right) + \frac{1}{r}\frac{\partial}{\partial r}\left(rwC_i\right) = \frac{1}{r}\frac{\partial}{\partial r}\left(rD_{e,i}\frac{\partial C_i}{\partial r} \right) + \frac{\partial}{\partial z}\left(D_{e,i}\frac{\partial C_i}{\partial z} \right) + S_i\left(t,z,r\right) \tag{3.19}$$

Where C_i is the molar density of species i in the gas phase, u and w are the axial and radial components of velocity, respectively, $D_{e,i}$ is the effective diffusion coefficient of

species i in the mixture. In the droplet transit zone, the latter is simply the unmodified gas phase diffusion coefficient, D_i. However, in the catalyst layer this diffusion coefficient must be modified according to $D_{e,i} = (\varepsilon/\tau)D_i$, where ε and τ are the porosity and tortuosity of the catalyst layer, respectively. The volumetric species source term, S_i, arises from droplet evaporation in the droplet transit zone and from chemical reactions in the catalyst zone. Due to the disparity of sizes (i.e. droplet vs. domain), it is assumed that the presence of a droplet results in a point source at its instantaneous location with the strength determined through the droplet transit equations presented above. This results in the following expression for the species source term:

$$S_i(t,z,r) = \begin{cases} \sum_{j=1}^{N_d} \frac{\dot{m}_{ev,d,i}^{(j)}}{MW_i} \delta\left(z - Z_d^{(j)}(t)\right) \frac{\delta(r)}{2\pi r} & 0 < z < H_{cell} \\ \sum_{k=1}^{N_{rxn}} \nu_{ik} r_k & H_{cell} \le z \le H_{cell} + H_{cat} \end{cases} \quad (3.20)$$

Here, the superscript j is an integer index identifying a particular droplet, N_d is the total number of droplets in the droplet transit zone, N_{rxn} is the number of reactions in the mechanism, ν_{ik} is the stoichiometric coefficient of species i in the kth reaction proceeding at a rate r_k.

Energy conservation is also satisfied throughout the entire domain.

$$\frac{\partial}{\partial t}\left[\left(\rho c_p\right)_e T\right] + \frac{\partial}{\partial z}\left[\left(\rho c_p\right)_g uT\right] + \frac{1}{r}\frac{\partial}{\partial r}\left[r\left(\rho c_p\right)_g wT\right] = \frac{1}{r}\frac{\partial}{\partial r}\left(rk_e \frac{\partial T}{\partial r}\right) + \frac{\partial}{\partial z}\left(k_e \frac{\partial T}{\partial z}\right) + S_h(t,z,r) \quad (3.21)$$

Here, k_e is the effective thermal conductivity, which for the droplet transit zone is equal to the gas phase thermal conductivity, k_g. In the catalyst zone local thermal equilibrium between the catalyst and gas is assumed, so only a single thermal energy conservation equation is required. Thus, in the catalyst layer, the effective thermal conductivity has

contributions from both the catalyst and gas phases, $k_e = \varepsilon k_g + (1-\varepsilon)k_c$, where k_c is the thermal conductivity of the solid catalyst. The effective thermal capacity is also the volume average of the gaseous and solid components, $(\rho c_p)_e = \varepsilon(\rho c_p)_g + (1-\varepsilon)(\rho c_p)_c$. The source term S_h in the catalyst layer comes from the heat of reaction, $S_h = \sum_i \Delta H_i r_i$, and in the droplet transit zone, it is the heat absorbed by evaporating droplets. A heat sink term can be written similar to the species source term for droplet evaporation.

$$S_h(t,z,r) = \begin{cases} -\sum_{j=1}^{N_d} q_c^{(j)} \delta\left(z - Z_d^{(j)}(t)\right) \dfrac{\delta(r)}{2\pi r} & 0 < z < H_{cell} \\ \sum_{i=1}^{N_{rxn}} \Delta H_i r_i & H_{cell} \le z \le H_{cell} + H_{cat} \end{cases} \tag{3.22}$$

Momentum conservation in the z and r directions satisfy the following equations, respectively:

$$\frac{\partial(\rho_g u)}{\partial t} + \frac{\partial(\rho_g u^2)}{\partial z} + \frac{1}{r}\frac{\partial(r\rho_g uw)}{\partial r} = -\varepsilon\frac{\partial p}{\partial z} + \frac{1}{r}\frac{\partial}{\partial r}\left(r\mu_g \frac{\partial u}{\partial r}\right) + \frac{\partial}{\partial z}\left(\mu_g \frac{\partial u}{\partial z}\right) + \frac{\varepsilon\mu_g}{K}u + S_{m,z}(t,z,r) \tag{3.23}$$

$$\frac{\partial(\rho_g w)}{\partial t} + \frac{\partial(\rho_g uw)}{\partial z} + \frac{1}{r}\frac{\partial(r\rho_g w^2)}{\partial r} = -\varepsilon\frac{\partial p}{\partial r} + \frac{1}{r}\frac{\partial}{\partial r}\left(r\mu_g \frac{\partial w}{\partial r}\right) + \frac{\partial}{\partial z}\left(\mu_g \frac{\partial w}{\partial z}\right) + \frac{\varepsilon\mu_g}{K}w + S_{m,r}(t,z,r) \tag{3.24}$$

Here, K is the permeability of the porous catalyst, and $S_{m,z}$ and $S_{m,r}$ are momentum sources in the z and r directions, respectively. For the droplet transit zone, $\varepsilon = 1$ and $K = \infty$, eliminating the Darcy term in the momentum equations above. The momentum sources in the droplet transit zone arise from viscous drag acting on the moving droplets and droplet evaporation. Since droplets are confined to move along the z axis, the radial source term only has a contribution from evaporation. The total radial momentum generation rate, $\dot{p}_{d,r}$, from a single droplet (point source) is calculated by integrating over the entire droplet surface.

$$\dot{p}_{d,r} = \int_A \rho_g V_e \left(V_e \sin\theta\right) dA = \frac{\dot{m}_{ev,d}^2}{16\rho_g R_d^2} \tag{3.25}$$

Here, θ is the angle from the unit cell axis, and the total local radial momentum generation rate is calculated similarly to the species source term,

$$S_{m,r}\left(t,z,r\right) = \sum_{j=1}^{N_d} \frac{\dot{m}_{ev,d}^{(j)}}{16\rho_g R_d^{(j)2}} \delta\left(z - Z_d^{(j)}\left(t\right)\right) \frac{\delta\left(r\right)}{2\pi r} \tag{3.26}$$

The axial momentum source term arises from viscous drag between the droplets and the surrounding gas phase.

$$S_{m,z}\left(t,z,r\right) = \sum_{j=1}^{N_d} \frac{6\pi\mu_g f_1 R_d^{(j)}\left(V_d^{(j)} - u\right)}{\rho_g V_d^{(j)}} \delta\left(z - Z_d^{(j)}\left(t\right)\right) \frac{\delta\left(r\right)}{2\pi r} \tag{3.27}$$

3.1.3 Boundary and Initial Conditions

A droplet is introduced into the droplet transit zone with the above specified initial conditions at intervals of $\tau = 1/f$. Introduction of a droplet increases the number of droplets in the domain by one ($N_d = N_d + 1$). A droplet is removed from the computational domain whenever it completely evaporates ($R_d = 0$), stops or reverses direction ($V_d \leq 0$), or it impinges on the catalyst ($Z_d + R_d = H_{cell}$), decreasing the number of droplets in the solution domain by one ($N_d = N_d - 1$). Further conditions associated with droplet impingement are discussed next.

Referring to Figure 3.1, the gas is initially assumed to be stagnant with all species concentrations at specified values and the droplet transit and catalyst zones at uniform, but different temperatures.

$$u(z,r,0)=w(z,r,0)=0,\quad C_i(z,r,0)=C_{i,0},$$
$$T(0<z<H_{cell},r,0)=T_{g,0},\quad T(H_{cell}<z<H_{cell}+H_{cat},r,0)=T_{c,0} \tag{3.28}$$

At the atomizer surface ($z = 0$), an adiabatic impermeable layer is assumed, yielding the following boundary conditions for the gas phase transport equations.

$$u(0,r,t)=w(0,r,t)=\left.\frac{\partial C_i}{\partial z}\right|_{z=0}=\left.\frac{\partial T}{\partial z}\right|_{z=0}=0 \tag{3.29}$$

Symmetry is enforced at the unit cell axis ($r = 0$) and along the boundary ($r = R_{cell}$).

$$w(z,0,t)=w(z,R_{cell},t)=\left.\frac{\partial u}{\partial r}\right|_{r=0,R_{cell}}=\left.\frac{\partial C_i}{\partial r}\right|_{r=0,R_{cell}}=\left.\frac{\partial p}{\partial r}\right|_{r=0}=0 \tag{3.30}$$

It is also possible to specify heat flux on the unit cell boundary $r = R_{cell}$ if heaters are deployed along the unit cell boundary.

$$k_e\left.\frac{\partial T}{\partial r}\right|_{r=R_{cell}}=q''_w(t,z) \tag{3.31}$$

Here, q''_w is taken as positive when heat is transferred from the unit cell boundary to the interior of the domain. At the reactor outlet ($z = H_{cell} + H_{cat}$), the pressure is specified, a heat flux matching condition is enforced, and the molar flux of each species is unchanging.

$$\begin{aligned}&p(H_{cell}+H_{cat},r,t)=p_{out},\\&h\left[T(H_{cell}+H_{cat},r,t)-T_\infty\right]=-k_e\left.\frac{\partial T}{\partial z}\right|_{z=H_{cell}+H_{cat}},\\&\left.\frac{\partial(uC_i)}{\partial z}\right|_{z=H_{cell}+H_{cat}}=0\end{aligned} \tag{3.32}$$

3.1.4 Reaction Kinetics

Kinetic expressions are required for the relevant reactions under study to complete the formulation of the gas phase transport equations presented above. This study is focused on conversion of methanol to hydrogen which can take place via steam reforming or partial oxidation as discussed in Chapter 2. Many kinetic studies have been carried out for the steam reforming of methanol over $Cu/ZnO/Al_2O_3$ catalysts primarily because of the potential of this reaction for onboard hydrogen supply for portable fuel cells. There is still some debate over the reaction mechanism. Some early studies suggested that the steam reforming mechanism is methanol decomposition to form hydrogen and carbon monoxide followed by water gas shift to convert the carbon monoxide to hydrogen and carbon dioxide using the water in the feed [74]. More recent studies have put forward more complicated surface mechanisms involving the formation of many intermediates before the final products are desorbed from the catalyst surface [39, 75]. Here, the kinetic model of Peppley et al. [76] is used to model the reaction in the catalyst zone. This model gives the rates of methanol steam reforming (r_{MSR}), methanol decomposition (r_{MD}), and water gas shift reaction (r_{WGS}) with the rate expressions derived using Langmuir-Hinshelwood type rate expressions considering the formation of several intermediate species on two different types of active sites on the catalyst surface. The model parameters were adjusted to best fit experimental studies performed for 160 ^{o}C < T < 260^{o}C, 1 atm < P < 10 atm, and 4-100% methanol conversion.

$$r_{MSR} = \frac{k_{sr} K^{*}_{CH_3O^{(1)}} \left(p_A / p_D^{1/2}\right)\left(1 - p_D^3 p_C / K_{sr} p_A p_B\right) C_{S_1}^T C_{S_{1a}}^T}{\left(1 + K^{*}_{CH_3O^{(1)}} \left(p_A / p_D^{1/2}\right) + K^{*}_{HCOO^{(1)}} p_C p_D^{1/2} + K^{*}_{OH^{(1)}} \left(p_B / p_D^{1/2}\right)\right)\left(1 + K^{1/2}_{H^{(1a)}} p_D^{1/2}\right)} S_A \qquad (3.33)$$

$$r_{MD} = \frac{k_d K^*_{CH_3O^{(2)}} \left(p_A / p_D^{1/2}\right)\left(1 - p_D^2 p_F / K_d p_A\right) C^T_{S_2} C^T_{S_{2a}}}{\left(1 + K^*_{CH_3O^{(2)}} \left(p_A / p_D^{1/2}\right) + K^*_{OH^{(2)}} \left(p_B / p_D^{1/2}\right)\right)\left(1 + K^{1/2}_{H^{(2a)}} p_D^{1/2}\right)} S_A \tag{3.34}$$

$$r_{WGS} = \frac{k_{wgs} K^*_{OH^{(1)}} \left(p_F p_B / p_D^{1/2}\right)\left(1 - p_D p_C / K_{wgs} p_F p_B\right)\left(C^T_{S_1}\right)^2}{\left(1 + K^*_{CH_3O^{(1)}} \left(p_A / p_D^{1/2}\right) + K^*_{HCOO^{(1)}} p_C p_D^{1/2} + K^*_{OH^{(1)}} \left(p_B / p_D^{1/2}\right)\right)^2} S_A \tag{3.35}$$

In these expressions, the k's are the Arrhenius rate constants [m^2/s-mol], K's are equilibrium constants, C's are surface concentrations of adsorption sites [mol/m^2], S_A is the specific surface area of the catalyst [m^2/m^3], and p's are partial pressures of each of the species [bar] (A = CH_3OH, B = H_2O, C = CO_2, D = H_2, and E = CO). The original paper [76] contains the values of the model parameters to be used in the above rate expressions.

3.1.5 Droplet Impingement and Film Growth

At the interface between the droplet transit and catalyst zones ($z = H_{cell}$), when droplet impingement occurs additional source terms for gas phase species, heat, and momentum result as the liquid fuel vaporizes on the catalyst surface. Accumulation of liquid at the catalyst interface is possible if the time between successive droplet impacts is less than the time it takes for a single droplet to vaporize after impact. Additionally, the liquid can penetrate into the catalyst via capillary suction. In general, tracking the liquid interface under these circumstances is a difficult task, but for this particular problem, all that is required is an estimate of the radial extent of the film and its penetration depth, rather than the detailed structure of the film interface and variation of mass flux over the interface. This allows certain simplifying assumptions to be made, which will prove sufficiently accurate in the model validation presented in chapter 4. The liquid is

assumed to be stagnant (on the time scale of droplet impingement) with a uniform species composition equal to that of the droplet upon impact and that the penetration depth of the liquid into the catalyst, $h_{f,c}$, is uniform across the film radius. This situation is shown schematically in Figure 3.2 with the boundaries of the film outside and inside the catalyst layer defined by $\Gamma_{f,g}$ and $\Gamma_{f,c}$, respectively, and the radius of the film given by R_f.

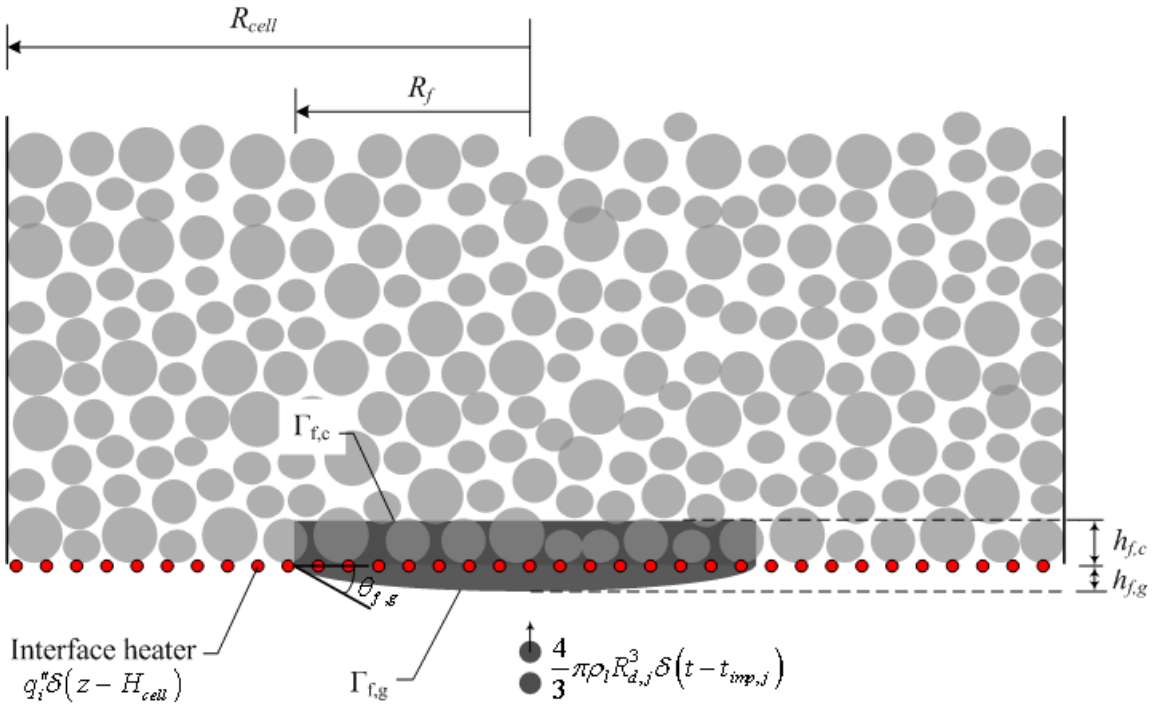

Figure 3.2. Depiction of film accumulation at catalyst interface.

The liquid film is subject to energy conservation, such that its temperature can change due to external heating, internal heating due to embedded wire heaters, droplet impingement, and phase change. Ignoring temperature variations in the liquid film would further simplifies the problem and it is worthwhile to determine the conditions under which this assumption holds. This is done by using a generalized Biot number (Bi) defined as the ratio of thermal resistances inside and outside the liquid film, with the film being treated as isothermal for Bi < 0.1. The ratio of thermal resistances is estimated as

$k_g R_f / k_l R_{cell}$ and using k_g = 0.03 W/m-K and k_l = 0.4 W/m-K, the criteria becomes $R_f / R_{cell} < 1.33$, which is true by definition since the film size cannot exceed the unit cell size. Thus, the liquid film is treated as isothermal for all cases with energy conservation governed by the following equation.

$$\left(\rho c_p\right)_e \frac{dT_f}{dt} = \int_{\Gamma_f} \left(k_e \left.\frac{\partial T}{\partial n}\right|_{int} - \sum_i m''_{ev,f,i} h_{fg,i} \right) dA + q''_{int} \pi R_f^2 \tag{3.36}$$

Here, T_f is the temperature of the liquid film, the integral over the film boundary accounts for external heat transfer and heat lost due to phase change, and the last term is the heat generated within the accumulated liquid by the interface heater.

Just as with the droplets, the evaporation rate at the film interface can be either mass or heat transfer limited. In the mass transfer controlled case, the evaporated species mass flux, $m''_{ev,f,i}$, is defined by the diffusive mass flux in the gas phase at the interface.

$$m''_{ev,f,i} = -\rho_g D_{i,e} \left.\frac{\partial y_i}{\partial n}\right|_{\Gamma_f} \tag{3.37}$$

Once the liquid temperature reaches saturation, vaporization controlled by the heat transfer rate occurs, the left side of eq. (3.36) is set to zero, and the species are assumed to evaporate in proportion to their liquid mass fractions.

The motion of the liquid film boundaries can be found by a mass balance at each interface. In tracking the film boundaries, the influence of gravitational force is neglected in comparison to the surface tension force, which is justified by the low value of the Bond number, *Bo*, for the cases studied here.

$$Bo = \frac{\left(\rho_l - \rho_g\right) g R_f^2}{\sigma} \tag{3.38}$$

Given that the film radius for most cases presented in this work is on the order of 0.001 m or less, *Bo* is on the order of 0.1 or less. A mass balance on the gas side of the film yields the following expression for the boundary motion.

$$\rho_l \frac{d\forall_{f,g}}{dt} = \frac{4}{3}\pi\rho_l R_{d,j}^3 \delta\left(t - t_{imp,j}\right) - \int_{\Gamma_{f,g}} \sum_i m''_{ev,f,i} dA - \dot{m}_p \tag{3.39}$$

Here, $\forall_{f,g} = \left(\pi/6\right) h_{f,g}\left(3R_f^2 + h_{f,g}^2\right)$ is the volume of the liquid film on the gas side of the catalyst interface, assuming that it is in the shape of a hemispherical cap, and $\dot{m}_p$ is the mass flow rate penetrating into the catalyst. Constraints on the liquid film geometry are also enforced due to the size of the unit cell, $0 \le R_f \le R_{cell}$. If $R_f = R_{cell}$, then the liquid film becomes cylindrical and only its height above the catalyst surface is changed.

Conservation of mass and momentum in integral form on the catalyst side of the liquid film give equations for the interface velocities at $z = H_{cell} + h_{f,c}$ and $r = R_f$ as well as the film penetration rate, $\dot{m}_p$. Conservation of mass is split into two equations, (3.40) and (3.41), by introducing the factor α, which is the fraction of $\dot{m}_p$ that contributes to radial growth of the film. Conservation of momentum in the axial and radial directions are given by eqs. (3.42) and (3.43), respectively. Here, it is assumed that the only forces acting on the liquid are Darcy friction and capillary pressure.

$$\varepsilon\pi R_f^2 \rho_l \frac{dh_{f,c}}{dt} + \int_0^{R_f} 2\pi r \sum_i m''_{ev,f,i} dr - \left(1-\alpha\right)\dot{m}_p = 0 \tag{3.40}$$

$$\varepsilon 2\pi R_f h_{f,c}\rho_l \frac{dR_f}{dt} + \int_{H_{cell}}^{H_{cell}+h_{f,c}} 2\pi R_f \sum_i m''_{ev,f,i} dz - \alpha \dot{m}_p = 0 \tag{3.41}$$

$$\frac{(1-\alpha)\dot{m}_p}{\pi R_f^2 \rho_l}\frac{d\forall_{f,c}}{dt} + \frac{1}{\rho_g}\int_0^{R_f} 2\pi r \sum_i m''^2_{ev,f,i} dr = \int_0^{R_f} 2\pi r P_c \varepsilon dr - \frac{\mu}{K}\frac{(1-\alpha)\dot{m}_p}{\pi R_f^2 \rho_l}\forall_{f,c} \tag{3.42}$$

$$\frac{\alpha \dot{m}_p}{2\pi R_f h_{f,c}\rho_l}\frac{d\forall_{f,c}}{dt} + \frac{1}{\rho_g}\int_{H_{cell}}^{H_{cell}+h_{f,c}} 2\pi R_f \sum_i m''^2_{ev,f,i} dz = \int_{H_{cell}}^{H_{cell}+h_{f,c}} 2\pi R_f P_c \varepsilon dz - \frac{\mu}{K}\frac{\alpha \dot{m}_p}{2\pi R_f h_{f,c}\rho_l}\forall_{f,c} \tag{3.43}$$

Here, $\forall_{f,c} = \varepsilon\pi R_f^2 h_{f,c}$ is the volume of liquid penetrated into the catalyst, $A_{f,c} = \pi R_f^2 + 2\pi R_f h_{f,c}$ is the interface area of the film on the catalyst side, and $P_c = 2\sigma\cos\theta_c / R_p$ is the capillary pressure in a pore of radius R_p. Equations (3.39)-(3.43) allow for solution of the interface velocities dR_f/dt, $dh_{f,g}/dt$, and $dh_{f,c}/dt$ along with $\dot{m}_p$ and α. These equations are subject to the constraints that R_f, $h_{f,c}$, $\forall_{f,g} \geq 0$ and $\dot{m}_p = 0$ when $\forall_{f,g} = 0$.

The pore radius is estimated with knowledge of the specific surface area, S_0, and mass density, ρ_s, of the porous catalyst zone.

$$R_p = \frac{2\varepsilon}{(1-\varepsilon)S_0\rho_s} \tag{3.44}$$

There are two scales of pore diameter to consider; "macropores" are defined by the voids between catalyst particles and there are also "micropores" within each catalyst particle. Which pore diameter controls the capillary flow into the catalyst depends upon the lateral extent of the accumulated liquid relative to the macropore diameter. If $R_f < R_p$ then $\dot{m}_p$ is controlled by flow through the micropores, and if $R_f > R_p$, then $\dot{m}_p$ is controlled by flow through the macropores. Another consideration is the effect of inefficient packing and

irregular particle shape and size on macropore controlled capillary flow. Transition from a small pore into a much larger void can stop the capillary flow through that pore. Hapgood et al. [77] developed a simple modification to account for these effects by introducing an effective porosity, $\varepsilon_{eff} = \varepsilon_{cp}\left(1-\varepsilon+\varepsilon_{cp}\right)$, and effective pore radius, $R_{p,eff}$, given by eq. (3.44) with ε replaced with ε_{eff} (ε_{cp} is the porosity of the close-packed bed). Here it is assumed that only a fraction of the total pore volume is useful for capillary driven flow, with the maximum drawing rate achieved when the bed is closely packed and $\varepsilon = \varepsilon_{cp}$. This closely packed porosity depends highly on the size and shape of the particles and must be determined experimentally. It is assumed that these effects can be ignored for liquid flow inside the micropores since the interior of the catalyst particles is well packed.

The contact angle of the liquid on the catalyst surface must also be estimated for the capillary penetration model. Chandra and Avedisian [67] present empirical results showing θ_c in the temperature range 50-200 ^{o}C for methanol on alumina with ε = 0.25. Since this closely approximates the conditions in this work, it is also used for this study.

To close the problem, conditions at the accumulated liquid interface must be supplied for the gas phase species and momentum conservation equations, in addition to those already specified for the energy conservation equation. These conditions are local species equilibrium at the interface between the liquid and gas, and velocity determined by the local evaporation rate. The equilibrium mole fractions for each species are calculated exactly the same as for the droplets in eq. (3.18).

$$C_i = C_T \chi_{i,s}, \quad v_n = \frac{1}{\rho_g}\sum_i m''_{ev,i}, \quad v_t = 0 \quad (z,r) \in \Gamma_{f,g} \cup \Gamma_{f,c} \tag{3.45}$$

3.1.6 Periodic Steady State Equations

Of particular interest is the steady-state behavior of the system after an initial startup period when all dependent variables reach a periodic (in time) steady-state driven by the periodic injection of droplets into the system. The equations describing the periodic steady-state behavior of the system can be found by time averaging the transient equations presented above over the forcing period, assuming each dependent variable, φ, can be represented as the sum of steady-state and time varying portions, $\varphi = \varphi_S + \varphi'$. The time average of any quantity, φ, is represented by $\overline{\varphi} = (1/T)\int_0^T \varphi dt$. For example, the time averaged species transport equation is given by the following equation.

$$\frac{\partial}{\partial z}\left(u_S C_{i,S} + \overline{u'C_i'}\right) + \frac{1}{r}\frac{\partial}{\partial r}\left(r w_S C_{i,S} + r\overline{w'C_i'}\right) = \frac{1}{r}\frac{\partial}{\partial r}\left(rD_{e,i}\frac{\partial C_{i,S}}{\partial r}\right) + \frac{\partial}{\partial z}\left(D_{e,i}\frac{\partial C_{i,S}}{\partial z}\right) + \overline{S_i}(z,r) \quad (3.46)$$

A considerable difficulty in solving the time averaged equations is properly evaluating the terms involving the time average of products of time varying quantities. For this reason, it is interesting to study the conditions for which the time varying portion of the solution is negligible. Physically, the time varying portion of the solution arises from the periodic nature of the droplet introduction into the system. This injection frequency defines a forcing timescale, $\tau_{for} = 1/f$. If this timescale is shorter than the shortest relaxation time for the various transport processes in the presence of the droplet stream, then the time varying portion of each dependent variable will be negligible. In other words, the gas phase dependent variables are disturbed as a droplet passes a given location, and in order for the process to be considered steady state, these disturbances cannot dissipate in the time it takes successive droplets to pass through this given

location. The relevant transport processes in the gas phase that are influenced by the droplets are diffusion (by evaporation), viscous dissipation (by drag forces), and conduction (by heat transfer) for which the relaxation times are $\tau_{diff} = L_s^2 / D$, $\tau_{visc} = L_s^2 / \nu$ and $\tau_{cond} = L_s^2 / \alpha$, respectively. The length scale for each process can be different and is defined as the length over which the relevant dependent variable changes in the presence of the droplet. Taking the length scale as the droplet radius gives the most stringent condition on the minimum droplet delivery frequency required to neglect the transient terms. This condition will change based on reactor operating conditions and its validity must be checked for each individual case.

$$f_{min} = \frac{1}{min\left(\tau_{diff}, \tau_{visc}, \tau_{cond}\right)} \tag{3.47}$$

With the assumption that the transient terms can be ignored, the time-averaged gas phase conservation equations are simplified as follows:

$$\frac{\partial}{\partial z}\left(uC_i\right) + \frac{1}{r}\frac{\partial}{\partial r}\left(rwC_i\right) = \frac{1}{r}\frac{\partial}{\partial r}\left(rD_{e,i}\frac{\partial C_i}{\partial r}\right) + \frac{\partial}{\partial z}\left(D_{e,i}\frac{\partial C_i}{\partial z}\right) + \overline{S_i}\left(z,r\right) \tag{3.48}$$

$$\frac{\partial}{\partial z}\left[\left(\rho c_p\right)_g uT\right] + \frac{1}{r}\frac{\partial}{\partial r}\left[r\left(\rho c_p\right)_g wT\right] = \frac{1}{r}\frac{\partial}{\partial r}\left(rk_e\frac{\partial T}{\partial r}\right) + \frac{\partial}{\partial z}\left(k_e\frac{\partial T}{\partial z}\right) + \overline{S_h}\left(z,r\right) \tag{3.49}$$

$$\frac{\partial\left(\rho_g u^2\right)}{\partial z} + \frac{1}{r}\frac{\partial\left(r\rho_g uw\right)}{\partial r} = -\varepsilon\frac{\partial p}{\partial z} + \frac{1}{r}\frac{\partial}{\partial r}\left(r\mu_g\frac{\partial u}{\partial r}\right) + \frac{\partial}{\partial z}\left(\mu_g\frac{\partial u}{\partial z}\right) + \frac{\varepsilon\mu_g}{K}u + \overline{S_{m,z}}\left(z,r\right) \tag{3.50}$$

$$\frac{\partial\left(\rho_g uw\right)}{\partial z} + \frac{\partial\left(r\rho_g w^2\right)}{\partial r} = -\varepsilon\frac{\partial p}{\partial r} + \frac{1}{r}\frac{\partial}{\partial r}\left(r\mu_g\frac{\partial w}{\partial r}\right) + \frac{\partial}{\partial z}\left(\mu_g\frac{\partial w}{\partial z}\right) + \frac{\varepsilon\mu_g}{K}w + \overline{S_{m,r}}\left(z,r\right) \tag{3.51}$$

In these time-averaged equations, the "*S*" subscript indicating the steady-state part of the variable has been removed to simplify the notation. The time-averaged droplet sources, $\overline{S}$, are found by making the substitution $dt = dZ_d/V_d$ in the integral. For example,

the species source becomes

$$\overline{S_i}(z,r)=\frac{1}{T}\int_{Z_d^{(j)}(0)}^{Z_d^{(j)}(T)}\sum_{j=1}^{N_d}\frac{\dot{m}_{ev,d,i}^{(j)}\left(Z_d^{(j)}\right)}{MW_i}\delta\left(z-Z_d^{(j)}(t)\right)\frac{\delta(r)}{2\pi r}\frac{dZ_d^{(j)}}{V_d^{(j)}\left(Z_d^{(j)}\right)} \tag{3.52}$$

At periodic steady-state, each successive droplet will follow the same trajectory under the same conditions allowing the above integral over a single period for every droplet to be replaced by an integral over the entire trajectory for a single droplet.

$$\overline{S_i}(z,r)=\frac{1}{T}\int_0^{H_{cell}}\frac{\dot{m}_{ev,d,i}(Z_d)}{MW_i}\delta\left(z-Z_d(t)\right)\frac{\delta(r)}{2\pi r}\frac{dZ_d}{V_d(Z_d)}=\frac{\dot{m}_{ev,d,i}(z)f}{MW_iV_d(z)}\frac{\delta(r)}{2\pi r} \tag{3.53}$$

The droplet source terms for the time-averaged heat and momentum conservation equations are found in an identical manner,

$$\overline{S_h}(z,r)=-\frac{q_c(z)f}{V_d(z)}\frac{\delta(r)}{2\pi r} \tag{3.54}$$

$$\overline{S_{m,z}}(z,r)=\frac{6\pi\mu_g f_1 R_d(V_d-u)f}{V_d}\frac{\delta(r)}{2\pi r} \tag{3.55}$$

$$\overline{S_{m,r}}(z,r)=\frac{\dot{m}_{ev,d}f}{16\rho_g R_d^2 V_d}\frac{\delta(r)}{2\pi r} \tag{3.56}$$

At steady-state, it is assumed that the uniform temperature of the liquid film accumulated at the catalyst interface is at the liquid saturation temperature so that the vaporization rate is heat transfer controlled and the energy conservation becomes

$$0=\int_{\Gamma_f}\left(k_e\left.\frac{\partial T}{\partial n}\right|_{int}-\sum_i m''_{ev,f,i}h_{fg,i}\right)dA+q''_{int}\pi R_f^2 \tag{3.57}$$

Determining whether a film forms under steady-state operation and, if so, what its time-averaged dimensions are requires an iterative procedure in which film dimensions are guessed and then updated based on the gas phase solution and resulting film vaporization

rate for that guess. Equations (3.42), and (3.43) describing momentum conservation in the liquid on the catalyst side are time-averaged and are used to calculate $\bar{\dot{m}}_p$ and α.

$$\frac{1}{\rho_g}\int_0^{R_f} 2\pi r \sum_i \bar{m}''^2_{ev,f,i} dr - \frac{\bar{\dot{m}}_p^2}{\rho_l \pi R_f^2} = \int_0^{R_f} 2\pi r \bar{P}_c \varepsilon dr - \frac{\mu}{K}\frac{(1-\alpha)\bar{\dot{m}}_p}{\rho_l}\bar{h}_{f,c} \tag{3.58}$$

$$\frac{1}{\rho_g}\int_{H_{cell}}^{H_{cell}+h_{f,c}} 2\pi \bar{R}_f \sum_i \bar{m}''^2_{ev,f,i} dz = \int_{H_{cell}}^{H_{cell}+h_{f,c}} 2\pi \bar{R}_f \bar{P}_c \varepsilon dz - \frac{\mu}{K}\frac{\alpha\bar{\dot{m}}_p}{2\rho_l}\bar{R}_f \tag{3.59}$$

Two regimes are possible depending on the value of the capillary penetration rate compared to the droplet delivery rate. If $\bar{\dot{m}}_p > (4/3)\pi\rho_l R_d^3 f$, this indicates that each droplet is completely imbibed into the catalyst layer before arrival of the next droplet; but in reality $\bar{\dot{m}}_p$ cannot exceed the droplet delivery rate. This is illustrated in graphical form in Figure 3.3, showing that the penetration rate exceeds the delivery rate, then falls to zero once the droplet is completely imbibed and this cycle repeats upon impingement of each new droplet.

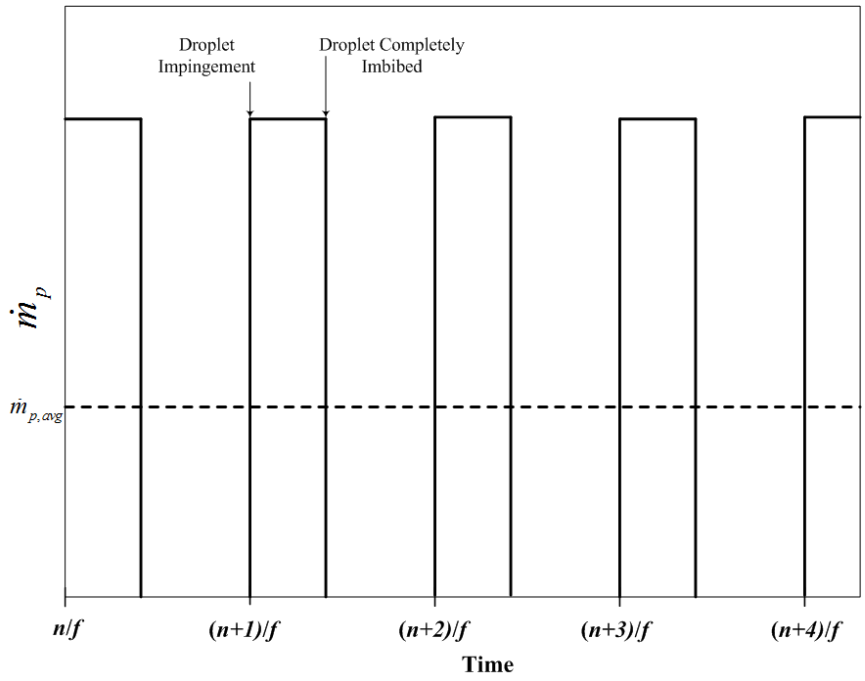

Figure 3.3. Capillary penetration rate as a function of time with periodic impingement of droplets. The instantaneous penetration rate at droplet impingement exceeds the droplet delivery rate, but the average penetration rate must equal the droplet delivery rate.

The actual capillary penetration rate in this case is obtained by time averaging eq. (3.39) and solving for $\bar{\dot{m}}_p$. This is then used to calculate the interface velocities from eqs. (3.40) and (3.41). The other case occurs when $\bar{\dot{m}}_p < (4/3)\pi\rho_l R_d^3 f$ and liquid also accumulates above the catalyst layer. In this case, $\bar{\dot{m}}_p$ calculated from eqs. (3.58) and (3.59) is the correct value and is used in eqs. (3.39)- (3.41) to calculate $dh_{f,g}/dt$, $dh_{f,c}/dt$, and dR_f/dt. In both cases the interface velocities are used to update the guess for the film dimensions using a pseudo timestep and the procedure is repeated until the boundary velocities are zero to within a specified tolerance. If the film grows to the unit cell boundary before convergence, then the catalyst has flooded and the calculation is terminated. In the opposite extreme, if the film dimensions shrink to the size of the impinging droplets, then flash evaporation is occurring.

3.2 Model Implementation

The steady-state model described above is implemented in the commercial computational fluid dynamics (CFD) software Fluent (v. 6.3.26) while Gambit (v. 2.2.30) is used to mesh the computational domain. The representative mesh in Figure 3.4 shows that the domain is divided into four regions, 1) the gas fluid zone, 2) the catalyst fluid zone, 3) the gas side film zone, and 4) the catalyst side film zone. The size of the film zones are initially guessed and then updated as described below. Gas phase conservation equations are only solved in the gas and catalyst fluid zones. The mesh is finer around the film interface, gas/catalyst interface, and axis boundary zones since gradients are expected to be highest in these regions due to film vaporization, interface heat sources, and droplet evaporation, respectively. Further downstream, the reaction rates drop as the conversion increases, so the grid is coarsened in this direction. Details of grid parameters, convergence, and discretization error estimates are presented in Appendix A along with the details of the model implementation.

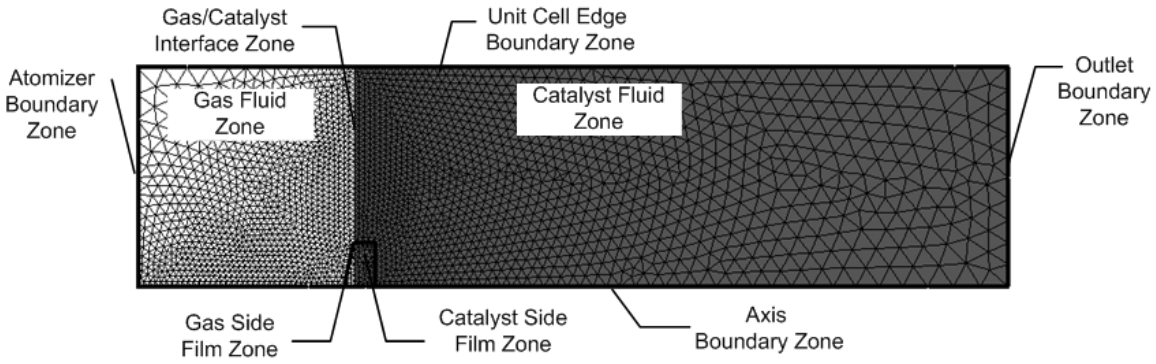

Figure 3.4. Representative mesh of DDIR unit cell model created in Gambit v2.2.30 showing the fluid and boundary zones defined in Fluent.

The solution starts from an initial guess of the gas phase dependent variables and film geometry. A multi-level iterative procedure is employed for determining the droplet trajectory (lowest iteration level), vaporization rate from the film (middle iteration level),

and the steady-state film dimensions (highest iteration level), which is summarized in Figure 3.5. The droplet trajectory (including droplet position, velocity, radius, temperature, and molar composition) is solved for a given solution of the gas phase conservation equations using a 4^{th} order vector Runge-Kutta method to integrate equations (3.1)-(3.5) with surrounding conditions obtained from the current gas phase solution in Fluent. This in turn provides sources for the gas phase conservation equations due to droplet heating, drag, and evaporation. These sources are applied in the computational cells adjacent to the axis boundary zone, and depend on the droplet conditions at the corresponding point along its trajectory. The gas phase conservation equations are solved again with these updated source terms and the procedure is repeated throughout the solution.

Sources for the gas phase conservation equations also arise from vaporization from the accumulated liquid film. These source terms are applied in the computational cells adjacent to the film interface, with the vaporization rate in each cell determined by the net local heat flux at the interface. As an initial guess, the total vaporization rate from the film is set equal to the droplet delivery rate with the sources uniformly distributed over the computational cells adjacent to the interface. At this level of iteration, the gas phase equations are solved until convergence is achieved, the film interface sources are updated and the procedure is repeated until the mass flow rate at the reactor outlet does not change within a specified tolerance.

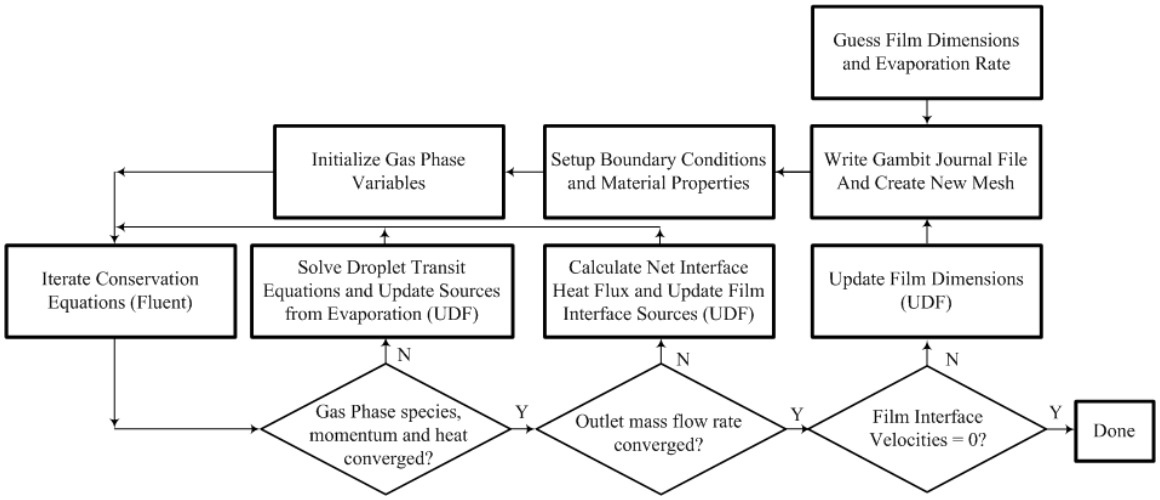

Figure 3.5. Flowchart showing general solution procedure for Fluent implementation of steady-state DDIR model.

Once the solution has converged for a given guess of the steady-state film size, the film interface velocities in equations (3.40) and (3.41) are used along with a pseudo-timestep to update the film dimensions. A new mesh is created with the updated film dimensions and the gas phase solution from the previous film dimensions is mapped onto the new mesh to improve the rate of convergence of the solution for the new mesh. This process is repeated until the interface velocities are zero within a specified tolerance. More specific details of problem setup and solution options are discussed further in appendix A.

CHAPTER 4

MODEL VALIDATION AND EXPERIMENTAL CHARACTERIZATION

4.1 Comparison of Model Results to Literature

Since there are several processes occurring simultaneously in the steady state DDIR model, validation is carried out by considering each of the major processes in isolation. Relevant results in the literature are used as a basis for comparison in validating each process in the model. Additionally, experimental validation studies are independently carried out for reaction/transport in the porous catalyst, and film growth/evaporation and compared with simulation results to provide confidence in applying the model.

4.1.1 Droplet Heating and Evaporation

To validate the droplet heating and evaporation model, the results of Varanasi et al. [73] are used. In this work, the evaporation of a stationary 50% molar heptane/decane droplet is computed numerically. The droplet is initially at 350 K and evaporates in dry nitrogen at 375 K. The latent heat, boiling point, and liquid density of both heptane and decane reported in the paper are used in these DDIR simulations and all other properties are taken from the Fluent materials database. The results in Varanasi et al. are presented in nondimensional form, and based on the data provided, a 45 μm droplet will have a lifetime of 0.041 s. Comparison of the normalized droplet surface area and temperature vs. time predicted by Varanasi et al. and the DDIR simulation is shown in Figure 4.1. The

same qualitative behavior is exhibited by both simulations, in which the more volatile heptane evaporates at a faster rate than the decane, causing the normalized droplet surface area and temperature to drop more quickly at the beginning of the droplet lifetime until the wet bulb temperature of the liquid mixture (~ 315 K) is attained. Once the heptane liquid mass fraction sufficiently decreases, the temperature begins to recover because the evaporation rate slows due to the lower volatility of the decane, as exhibited by the decreased slope of the normalized surface area curve. The DDIR model predicts temperatures about 2–3 K higher in the temperature recovery zone and a lifetime about 5% shorter. These are most likely due to differences in properties used between the two simulations, since Varanasi et al. do not provide a comprehensive list of properties used in their simulations.

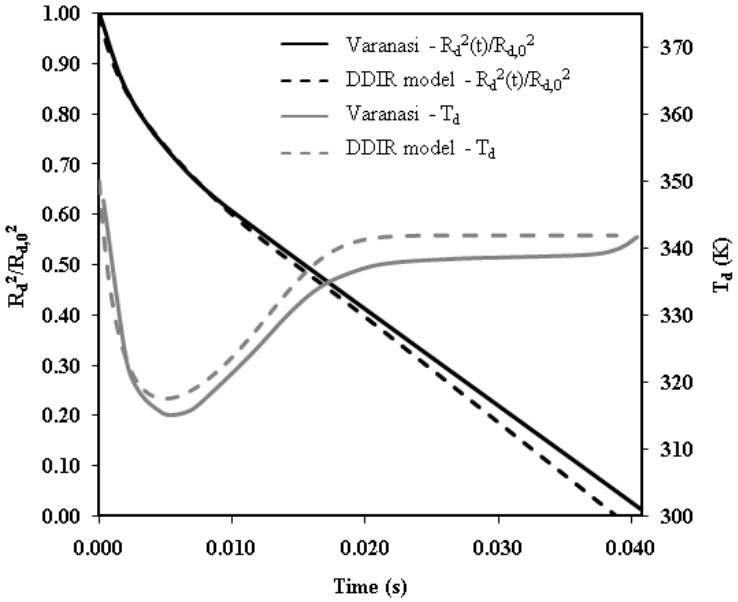

Figure 4.1. Comparison of evaporating droplet surface area and temperature change for 50% heptane/50% decane mixture as a function of droplet lifetime using DDIR model and by Varanasi et al.

4.1.2 Liquid Penetration

The bulk of literature results for capillary penetration of a liquid into a porous medium consider a single volume of liquid initially deposited onto a porous substrate rather than a continuous supply of droplets. Furthermore, simultaneous liquid vaporization due to heating of the porous bed is rarely considered. As a result, the film growth and penetration model must be validated under these simpler conditions. The results of Alleborn and Raszillier [78] are used for comparison with the transient penetration model presented above. In this work, the simultaneous spreading and sorption of a single liquid droplet on a thick porous substrate is considered where momentum conservation in the liquid layer is a balance between pressure and Darcy friction with a constant capillary pressure acting at the liquid interface. The liquid front is tracked using a modified enthalpy method. Initially, the liquid is completely above the surface and is imbibed into a substrate with porosity 0.25, a dimensionless permeability, Pm = $3KR_e^2/h_e^4 = 10^{-5}$, and a dimensionless capillary suction, Su = $P_c R_e^2/\sigma h_e = 5\text{x}10^5$, where h_e and R_e are the equilibrium radius and height of a given volume of liquid on a solid surface with a contact angle θ_c. Their results show that a dimensionless time, $t\sigma h_e^3/3\mu R_e^4 = 0.29$ is required to imbibe 99% of the liquid volume with the profile of the liquid front presented graphically for intermediate times. For the DDIR capillary penetration model, an initial film radius of 5 mm is assumed, from which all other parameters are calculated using the dimensionless groups defined by Alleborn and Raszillier, and assuming the initial dimensionless volumes are equal. The results show that a dimensionless time of 0.22 is required to imbibe 99% of the droplet volume. Additionally, the location of the liquid interface is compared at three different times for

both methods in Figure 4.2, demonstrating that the DDIR model effectively captures the radial spreading of the liquid as it enters the porous layer. Considering the vast computational savings in solving a set of first order ODEs over the 2-D momentum conservation with front tracking, the results obtained with the simplified model are acceptable.

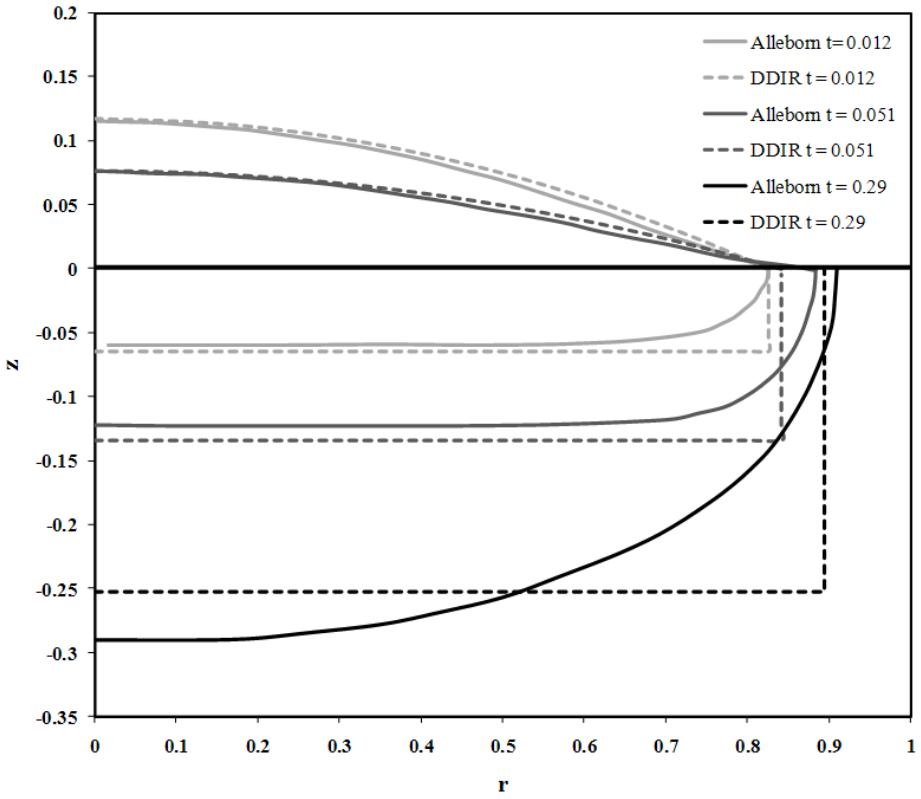

Figure 4.2. Comparison of capillary penetration model used in DDIR studies with numerical results of Alleborn and Raszillier [78] for imbibition of a liquid film into a thick porous substrate. The liquid-gas interface is shown for both methods at three separate times.

4.1.3 Methanol Steam Reforming Reaction

The experimental results of Lee et al. [79] for methanol steam reforming are used to validate the DDIR reaction model. These investigators packed a 0.25 in. diameter stainless steel tube with 1.0 g of commercially available Synetix 33-5 catalyst ground and sieved to a particle size between 0.3 and 0.42 mm. A mixture consisting of 15 mol %

methanol, 15 mol % water vapor, and balance nitrogen (inert sweep) was introduced into the reactor with a total flow rate of 200 sccm. Methanol conversion was reported for temperatures in the range 160-260 ^{o}C. The DDIR simulations were run without droplets, the ejector boundary was changed to an inlet boundary condition with the above composition and flow rate used in the experiments, and the catalyst zone set to a constant temperature, mimicking the experimental conditions. Comparison of the results is shown in Figure 4.3.

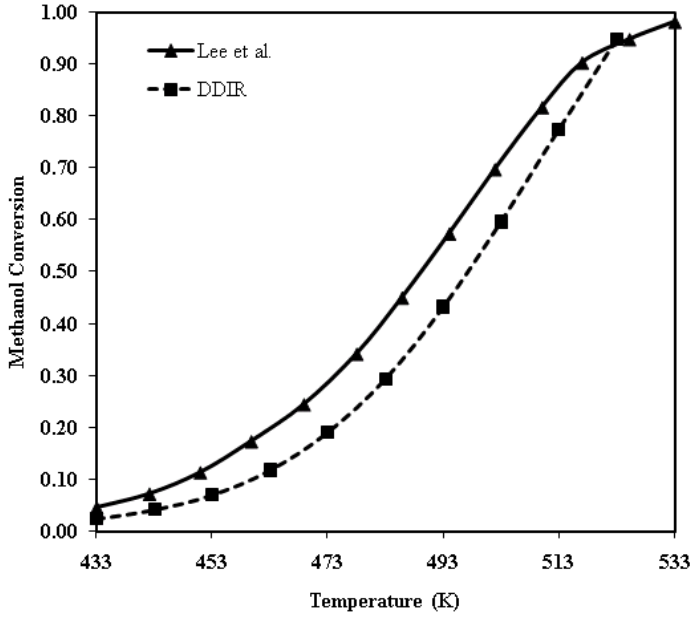

Figure 4.3. Validation of methanol steam reforming reaction kinetics used in steady state DDIR model. Simulation conditions correspond to the experiments of Lee et al., which is the basis for comparison.

The methanol conversion predicted by the DDIR model follows the same trend with temperature as observed experimentally, but displays a lower conversion at a given temperature throughout most of the range. Possible reasons for this deviation are deviations from temperature uniformity in the experiments and differences in catalyst morphology (possibly different specific surface areas and effectiveness factors) between that used by Lee et al. and that used in determining the kinetic expression.

4.2 Experimental Validation Using Unit Cell Reactor

In addition to comparing the results of the different components of the model to relevant literature results, an experimental apparatus is constructed to approximate a unit cell of the DDIR reactor. This apparatus is used to examine the processes of droplet transit, film growth, and reaction and compare them to simulations run under identical conditions to gain confidence in the accuracy of the model results.

4.2.1 Experimental Apparatus

To properly validate the results from the steady-state simulations, the experimental reactor must closely match the conditions of the unit cell model. To ensure this, an experimental reactor was constructed that meets the following design specifications:

- The droplet generator produces a single stream of droplets with a uniform size operating continuously without interruption. Droplet size, flow rate, and delivery frequency can be easily adjusted by a change of atomizer components.
- Impingement of droplets on the catalyst surface is clearly visible by an external camera and resulting images can be recorded on demand.
- Two independent heaters are employed 1) at the impingement interface and 2) along the periphery of the reaction chamber to control the film growth and catalyst bed temperature, respectively.
- The electrical heater at the impingement interface has the power capacity to prevent flooding of the catalyst with droplets of 40 μm diameter impinging at a frequency of 100 kHz.
- The electrical heaters are temperature controlled to prevent burnout in case droplet

generation is interrupted.

- The temperature is monitored at the impingement point and within the bulk of the catalyst.
- Analysis of the gaseous products occurs via mass spectrometry and is displayed in real-time.

The resulting design is a product of multiple iterations and is shown in schematic form in Figure 4.4 along with the instrumentation used to control the reactor and make measurements.

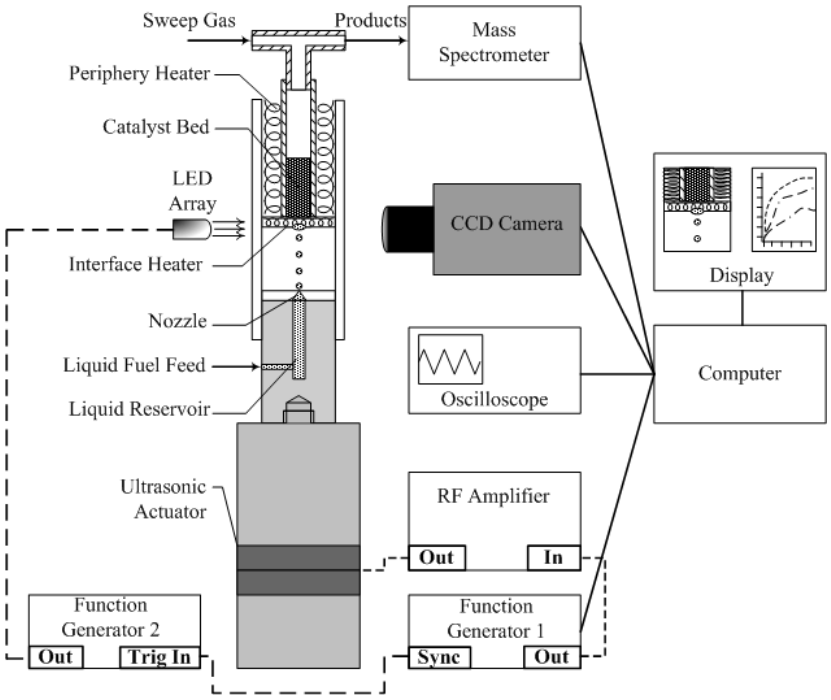

Figure 4.4. Schematic of experimental apparatus of DDIR unit cell showing control and measurement instrumentation used.

Droplets are generated by forcing the liquid fuel through a small opening at elevated pressure, forming a jet that is subsequently broken up into droplets via acoustic excitation of the nozzle structure. The ultrasonic actuator consists of four disk shaped piezoelectric elements sandwiched between titanium rods, having a 5/8 in. diameter and

an overall length of 4 in. A sinusoidal signal is generated by an Agilent 33250A function generator, amplified with an ENI 2100L RF power amplifier and applied across the faces of the piezoelectric elements resulting in axial excitation. A Tektronix TDS2014 oscilloscope attached to the output of the RF amplifier monitors the applied voltage level, frequency, and waveform shape. The liquid reservoir is made of titanium and is attached to the ultrasonic actuator with a ¼"-28 threaded connection and includes a side port for liquid feed. The nozzle structure is exactly the same as that used in the ultrasonic atomizer described in section 2.1.4 and is fixed to the liquid reservoir with Duralco 4525 epoxy from Cotronics Inc., which provides the necessary strength and chemical resistance for working with the pressurized liquid methanol/water mixture.

The catalyst used in all experiments is BASF F3-01, which is comprised of Cu/Zn supported on γ-Al_2O_3. The catalyst is supplied as 1.5 mm x 1.5 mm cylindrical pellets, which are crushed and sieved to obtain the desired average catalyst particle size for each experiment. Before utilizing the catalyst for reaction, it is reduced by heating to ~220 ^{o}C and flowing a mixture of ~200 sccm of argon and ~20 sccm of hydrogen for about 1 hour. Both argon and hydrogen flows are metered using MKS mass flow controllers (MFCs) connected to an interface unit allowing for both control and monitoring of the flow rates (MKS Type 247). The argon MFC (M/N M100B00453CS1BV) has a full scale of 5000 sccm while the hydrogen MFC (M/N 1259-000203V) has a full scale of 20 sccm. The argon flow is additionally monitored using a Cole Parmer 150 mm tube rotameter because of the high relative uncertainty associated with the argon mass flow controller measurement, which is discussed below. The reaction experiment must be carried out immediately following reduction to avoid leaking of air into the system and deactivation

of the catalyst.

A ceramic tube (99% alumina) contains the catalyst, which is heated with two independently controlled heaters: one along the outside of the ceramic tube and the other at the droplet impingement interface. The periphery heater is formed by wrapping 30 AWG nickel-chromium (nichrome) wire tightly around the outer diameter of the ceramic tube. An outer ceramic tube (macor) encases the inner ceramic tube and periphery heater to provide electrical and thermal insulation from the environment. The outer ceramic tube also has rectangular grooves to accommodate lead wires and thermocouple feeds. These wires are fixed into the channels by filling with Resbond 920 ceramic adhesive.

The interface heater, shown in Figure 4.5 is constructed by wrapping 36 AWG nichrome wire toroidally around two thin macor disks, which are sandwiched together using ceramic adhesive, which also serves to electrically insulate the two disks. A copper woven wire mesh (100 mesh) is attached to the bottom using the same ceramic adhesive to hold the catalyst in place. The two sections of the heater are connected in parallel and powered from the wall, using a Variac to control the voltage input.

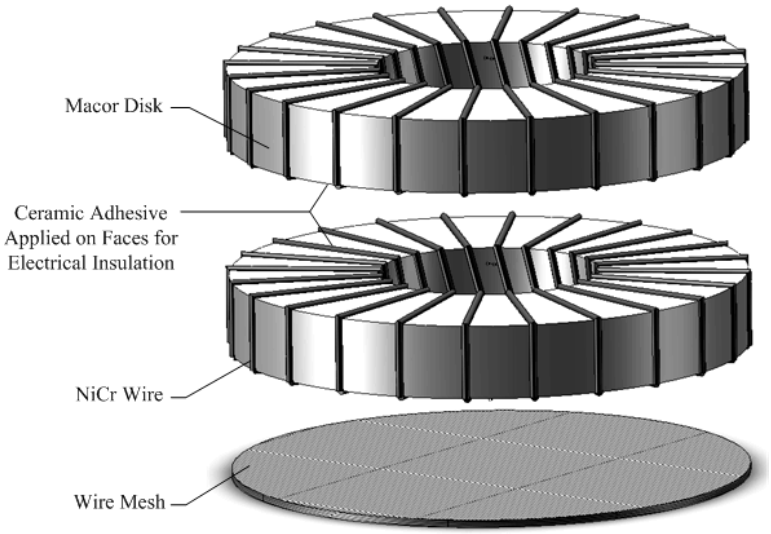

Figure 4.5. Construction of Interface Heaters for DDIR Experimental Apparatus

Temperature is monitored at the wire mesh near the edge of the inner reactor wall as well as at the back end of the interface heater using K-type thermocouples (OMEGA CHAL-0005). The thermocouple at the wire mesh gives a measure of the extent of liquid accumulation along the catalyst interface in addition to the visual method described below. If the temperature measured by the interface thermocouple is at or below saturation for the liquid mixture, this signifies flooding of the catalyst layer is occurring. The thermocouple at the back of the interface heater monitors the maximum temperature in the reactor. A separate J-Type thermocouple is used to measure various points on the reactor surface during testing as a secondary monitor. All thermocouples are routed through an Agilent 34970A data acquisition unit, allowing for real-time monitoring of the relevant reactor temperatures.

Argon is swept across the reactor outlet through a three-way fitting, carrying the product stream to a Hiden Analytical HPR20 quadrupole mass spectrometer for analysis. The sampling capillary on the mass spectrometer is heated, allowing the unreacted condensable methanol and water to be sampled and detected by the mass spectrometer.

To prevent contamination of the pump oil in the system, the pump oil chambers are vented when products are being sampled and for at least 30 minutes after. The three-way fitting used for the sweep gas is designed to create a Venturi effect, lowering the pressure at the reactor outlet and aiding the flow of products.

Visualization of the droplet impingement at the catalyst interface is accomplished with a stroboscopic technique as described in [62]. An array of LEDs is pulsed at the same frequency at which the ultrasonic actuator is powered using a pulse width approximately 10 times less than the driving period. Two separate camera systems were utilized depending on the data acquired. For high magnification images of the droplet transit and impingement, a Redlake MEGAPLUS ES 1.0 CCD camera controlled with a National Instruments IMAQ 1422 image acquisition board captures the images of the droplet impingement. For larger field of view images of film accumulation at the catalyst interface a Keyence VHX-500F digital microscope was utilized. Post-processing is done using National Instruments Vision Assistant software (v. 8.2) using a microscope reticle to obtain a calibration for the length of a pixel at a given magnification, and using this calibration to measure desired features on the captured images.

4.2.2 Measurement Errors and Uncertainty Analysis

The measurements of temperature, flow rates, partial pressures, and visualized feature sizes have associated uncertainties that must be considered when reporting results. The K-Type thermocouples (OMEGA CHAL-0005) have a reported accuracy of ± 2.2 K for the range of temperatures considered in these experiments (150 – 300 ^{o}C).

The flow rate measured by the mass flow controllers has an error equal to +/- 1% of full range, which is +/- 50 sccm for the argon flow meter and +/- 0.2 sccm for the

hydrogen flow meter. The rotameter used as a secondary monitor of the argon flow rate has an estimated error of +/- 20% of the smallest graduation. This results in uncertainties of +/- 5.5 sccm and 6.5 sccm at 200 and 500 sccm, respectively. For this reason, the rotameter reading is used in all calculations.

Estimating the error in the mass spectrometer partial pressure measurements is more difficult. In order to obtain reliable quantitative results, regular calibrations must be performed in the range of compositions expected in the actual experiments. In these calibrations, known feed rates of species are mixed together and sampled by the mass spectrometer after sufficient mixing has occurred. One of these species is always a reference and the ratio of flow rate of any other species, $\dot{\forall}_i$, with the reference , $\dot{\forall}_{ref}$, can then be compared to the ratio of the measured species partial pressure, p_i, to that of the reference, p_{ref}, to obtain correction factors (also called relative sensitivities).

$$RS_i = \frac{p_i / p_{ref}}{\dot{\forall}_i / \dot{\forall}_{ref}} \tag{4.1}$$

In subsequent experiments, the flow rate of any other species can be calculated with knowledge of the reference flow rate and partial pressures of both the species of interest and the reference.

$$\dot{\forall}_i = \frac{p_i / p_{ref}}{RS_i} \dot{\forall}_{ref} \tag{4.2}$$

In the case of the reactor experiments, as stated above, the reference used is argon. It is an easy matter to obtain the calibration for hydrogen relative to argon during the catalyst reduction process. However, it is not practical to perform this calibration for any other species of interest (methanol, water, carbon dioxide, carbon monoxide) with the reactor

online. Given this, the error in the hydrogen partial pressure is taken as +/- 1% and a more conservative estimate of +/- 5% is taken for all other species.

Calibration of the images obtained is performed by capturing the image of a microscope reticle with the same magnification. The reticle used has graduations of 10 μm and a full scale size of 1 mm. The number of pixels between the graduations at the ends of the image is used to obtain the length of one pixel. This one pixel length is also taken as the uncertainty for any measurements taken at the given magnification.

4.2.3 Estimation of Heat Losses

The single unit cell experimental apparatus is subject to heat loss to the surroundings, primarily from the sidewalls of the reactor. Proper estimation of these losses is critical so that the conditions applied in the simulations reasonably closely match those in the corresponding experiments. Heat loss occurs via combined convection and radiation from the outer surface of the reactor. Because the experiments are performed in a fume hood with bulk flow transverse to the buoyancy driven flow, the possibility of the combined effect of forced and natural convection must be considered.

For all experiments, velocity of the bulk flow is 110 LFPM with a temperature of 295 K and the outer diameter of the cylindrical reactor is 0.35 in., giving Re_D = 180. The length of the reactor is 1.75 in., and taking the outer surface temperature as 250 ^{o}C, Gr_L = 9.6x10^5. Thus, Gr_L / Re_D^2 = 30 and forced convection effects are neglected [80]. The natural convection coefficient is estimated from the correlation of Churchill and Chu [80], yielding h_c = 14 W/m^2-K. Radiative losses are accounted for using the radiative heat transfer coefficient, $h_r = \varepsilon\sigma\left(T_o + T_\infty\right)\left(T_o^2 + T_\infty^2\right)$. To calculate the local net heat flux into the reactor, a thermal resistance network is used as depicted in Figure 4.6. Here, the

thermal resistances per unit length are $R_i' = \ln\left(OD_i / ID_i\right)/2\pi k_i$, $R_o' = \ln\left(OD_o / ID_o\right)/2\pi k_o$, $R_c' = 1/\pi\, OD_o h_c$, and $R_r' = 1/\pi\, OD_o h_r$, where OD and ID stand for the outer diameter and inner diameter respectively while the subscripts *o* and *i* denote the outer and inner tubes comprising the unit cell reactor, respectively. The temperature at the inner surface, T_s, is taken from the current iteration of the solution to solve for the local heat transfer rate into the catalyst bed.

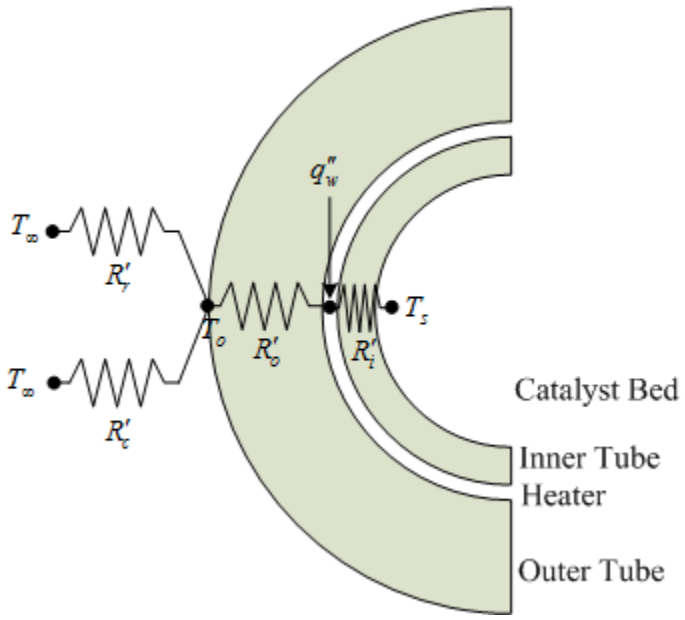

Figure 4.6. Thermal resistance network used for calculating heat losses in simulations accompanying experimental studies of unit cell DDIR.

Employing this thermal resistance network to calculate the heat flux entering the reactor at the inner surface yields

$$q_{in}'' = \frac{q_w' R_{eq,out}' - \left(T_s - T_\infty\right)}{R_{eq,out}' + R_i'} \frac{1}{\pi\left(ID_i\right)} \tag{4.3}$$

where q_w' is the local heat rate per unit length, $R_{eq,out}'$ is the equivalent thermal resistance between the heat input location and the surroundings.

4.2.4 Experimental Validation of Variation of Film Size with Applied Heat Flux

In these experiments, a steady stream of droplets impinged on the catalyst interface and the variation in the lateral extent of the accumulated liquid film was observed with applied power to the interface heater. For all cases, $R_{d,0}$ = 31 µm, f = 30 kHz, and $V_{d,0}$ = 5.1 m/s as depicted in Figure 4.7 (b), verifying the regular, well-controlled nature of droplet delivery to the catalyst interface. The error associated with length measurement (± 1 pixel) was 1.5 µm at this magnification. For the observed droplet conditions, We = 43, which is below the splashing threshold (We > 80), which was also visually confirmed. A wider view is shown in Figure 4.7, clearly demonstrating the growth of a liquid film on the catalyst interface, which is highlighted by illuminating the interface with a red LED.

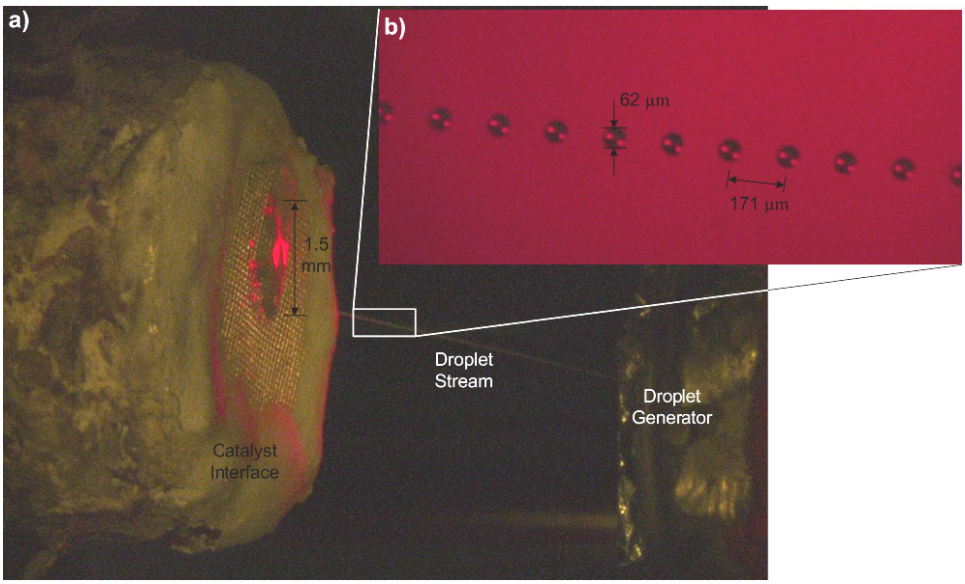

Figure 4.7. a) Impingement of droplet stream and accumulation of liquid film on stainless steel mesh (25 µm opening) holding packed bed of catalyst particles (100 µm average particle diameter). Illumination of the interface with red LED clearly shows the extent of the liquid film. b) Magnified stroboscopic image of droplets in transit (f = 30 kHz).

The total heat supplied at the interface was varied between 6-20 W and the image was recorded at each setting. Approximately 5 minutes was allowed to elapse after

changing the interface heater voltage to ensure steady state had been achieved. The measurement error for the film size (± 1 pixel) was ±0.1 mm for each case since the same magnification was used for each image. Simulations were performed for the same range of applied interface heat, and the resulting radial extent of the film was compared with the experimental results, as shown in Figure 4.8. Below the amount of heat required to completely vaporize the droplet feed, flooding must occur, and this is shown in the hatched region. Decrease in the film size with increasing supplied heat is observed for both the experimental and simulation results as expected and the results correspond with exceptional accuracy.

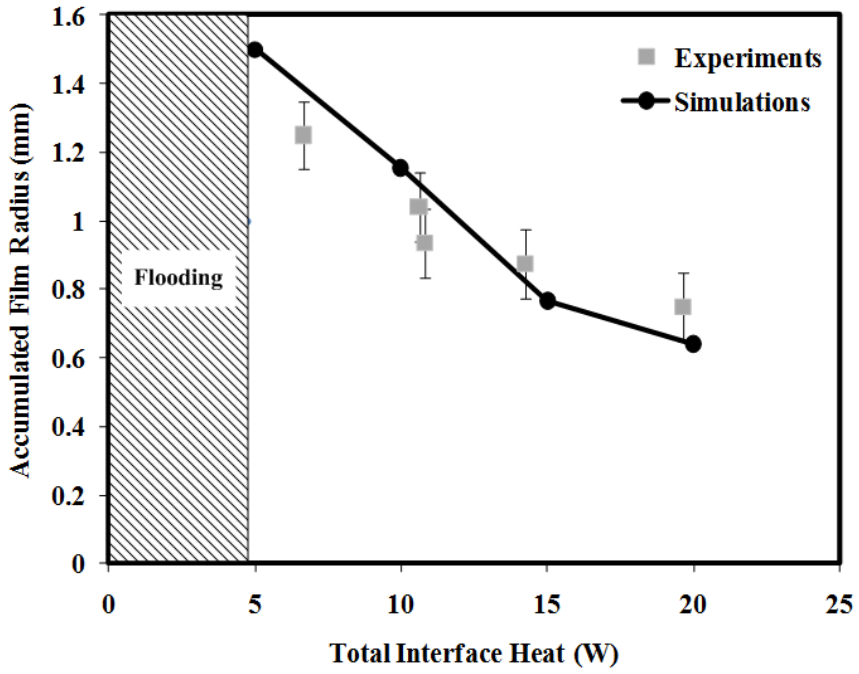

Figure 4.8. Comparison of accumulated liquid film radius observed experimentally with simulation results under identical conditions.

4.2.5 Experimental Validation of Capillary Penetration Model

As stated in section 3.1.6, if the maximum capillary penetration rate is larger than the droplet delivery rate, then each droplet is completely imbibed into the catalyst layer

and none of the accumulated liquid film protrudes from the catalyst surface. The transition from a completely imbibed liquid film and one that is partially supported above the catalyst interface was observed experimentally by comparing the results for average catalyst particle sizes of 100 µm and 10 µm. In both cases, a stream of 15 µm droplets was delivered at 1 MHz with 3.6 W applied to the interface heater. In Figure 4.9 (a) the film thickness above the catalyst interface is not measurable, although the wetted portion of the interface is clearly visible by the reflected light from the stroboscopic source. With the smaller catalyst particles, the film thickness is clearly non-zero as seen in Figure 4.9 (b).

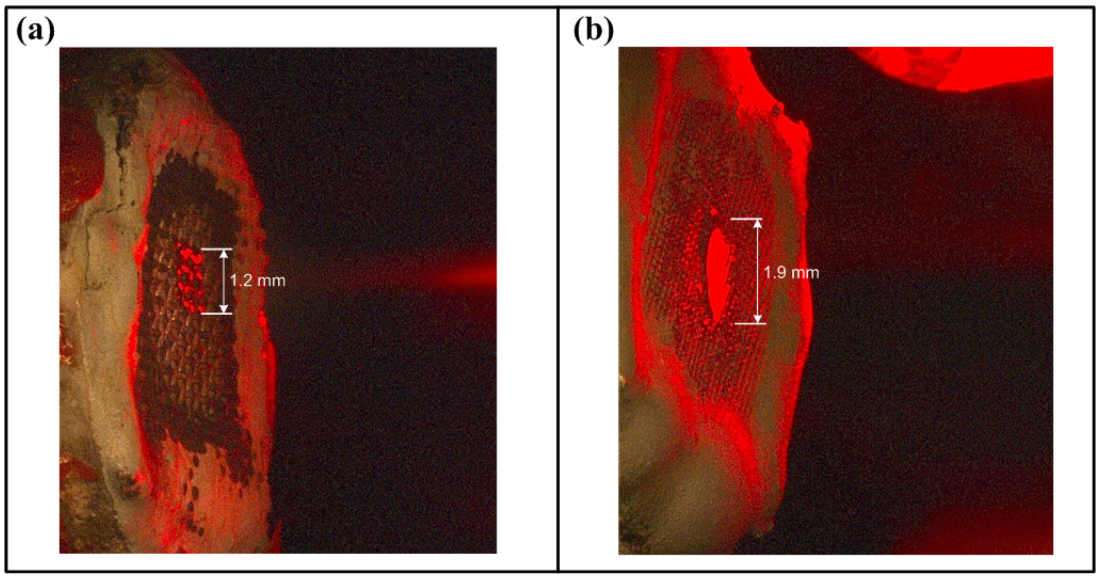

Figure 4.9. Visualization of accumulated liquid film at catalyst interface with 3.6 W interface heater power and impinging stream of 15 µm droplets at 1 MHz. a) Average catalyst particle diameter 100 µm, b) Average catalyst particle diameter 10 µm.

It is impossible to compute the capillary penetration rate from the visualization results because of its dependence on the penetration depth, which is not optically accessible. For this reason, simulations were carried out under identical conditions to ensure that the relative rates of droplet delivery and capillary penetration are

commensurate with the observed experimental results. For both simulations, 15 μm diameter droplets are delivered at a rate of 1 MHz with an initial velocity of 15 m/s. Also, for both cases R_{cell} = 1.5 mm with a total of 3.6 W applied uniformly along the catalyst interface. Note that in the experiments, the overall lateral extent of the reactor is larger because of the encasing material, but the inner diameter is the same as in the simulations. Figure 4.10 shows the accumulated liquid at the catalyst interface for both (a) the 100 μm particles and (b) the 10 μm particles. In this figure, the heavy vertical line denotes the catalyst interface with the catalyst bed lying to the left (corresponding to the experimental visualization results). The results show that the liquid penetrates deeper into the catalyst layer, but does not spread as much for the larger catalyst particles. Also, more liquid is supported above the catalyst interface for the smaller catalyst particles. These results qualitatively agree with the experimental results presented above, but there is some disagreement between the experimental and simulation results, each case displaying an approximately 40% difference between the observed and the simulated film sizes. However, it should also be noted that the ratios of the observed to the simulated film radius are approximately the same, with a value of 0.63 for the 100 μm particles and 0.65 for the 10 μm particles. One possible reason for the numerical discrepancy is overestimation of the heat losses used in the simulations, which would cause the size of the accumulated liquid film to be greater than expected.

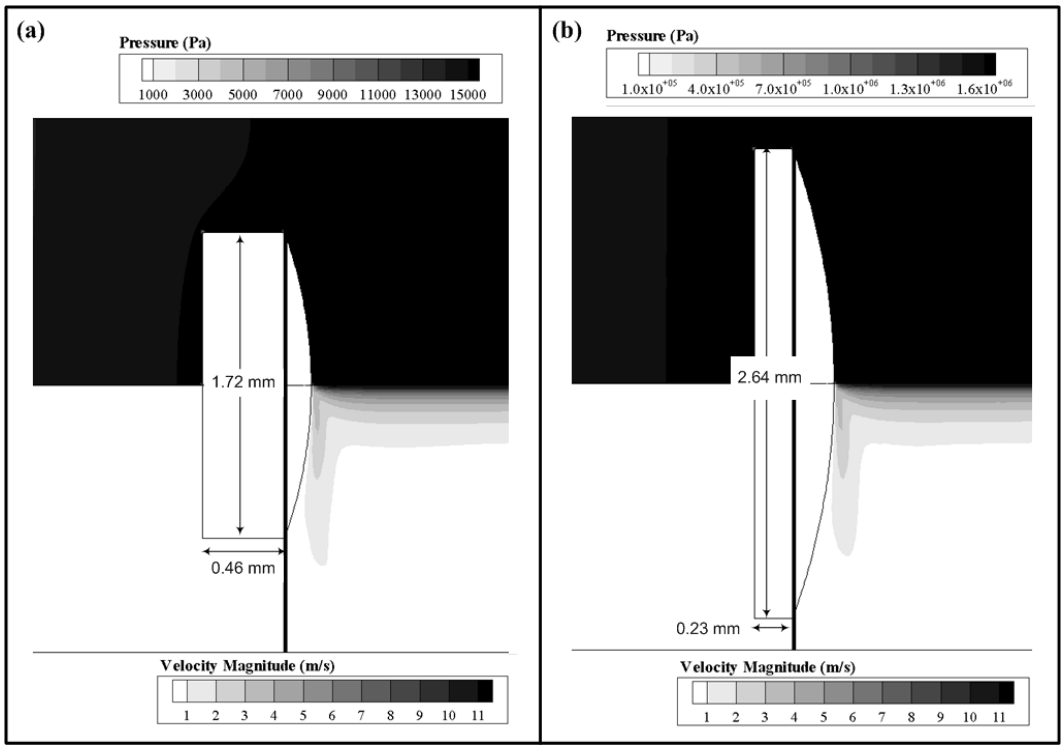

Figure 4.10. Simulation results accompanying visualization of liquid accumulation at catalyst interface. For both cases, $R_{d,0}$ = 7.5 µm, f = 1 MHz, R_{cell} = 1.5 mm, Q_{int} = 3.6 W a) d_p = 100 µm, b) d_p = 10 µm.

Another feature observed in the simulation results is a factor of 100 increase in gas phase pressure at the catalyst interface with the factor of 10 decrease in the catalyst particle size, due to the increased Darcy friction. In the experiments, this pressure increase was not realized because the space between the atomizer and catalyst was not enclosed.

4.2.6 Experimental Validation of Hydrogen Production from Unit Cell Reactor

In this set of experiments, the methanol steam reforming reaction was carried out using the DDIR unit cell experimental apparatus described above, varying the heater power input to observe the transition from flooding to stable film formation while monitoring the product composition with the mass spectrometer. Argon was introduced at the reactor inlet at a rate of 250 sccm as well as being swept across the reactor outlet at

the same rate. The average catalyst particle size used was 100 μm and was filled to a height of 15 mm in the inner tube of the reactor with the remainder of the tube filled with inert alumina particles of approximately the same average size. Droplets with a diameter 56 μm were introduced to the reactor at a rate of 24 kHz with approximately 10 mm of space separating the surface of the droplet generator and the catalyst interface.

After catalyst reduction, a 30 minute settling period was allowed before commencing droplet generation. The voltage of the periphery heater was kept constant throughout the entire test at 50 VRMS, while the interface heater voltage was varied between 3.5 – 10 VRMS. At each interface heater voltage setting, a dwell time of at least 10 minutes was used to allow the catalyst bed temperature and species composition to reach steady state. Also, the current flowing through the interface was monitored using a Fluke true RMS multimeter (M/N 179) to obtain more accurate readings of the power input. The transient response of the hydrogen partial pressure read at the mass spectrometer shown in Figure 4.11 justifies waiting 10 minutes before taking measurements. When droplet impingement commences, the catalyst surface is hot, so the conversion is high, and the interface cools quickly as the liquid film accumulates at the catalyst interface. The heater is adjusted manually from its low baseline value after impingement occurs, at which point the hydrogen flux partially recovers and approaches its steady state value. This manual adjustment is necessary because supplying the interface heat rate necessary to achieve a steady-state film would cause burnout under dry conditions. Once steady impingement is occurring, a change in heater input will take less time to reach steady state.

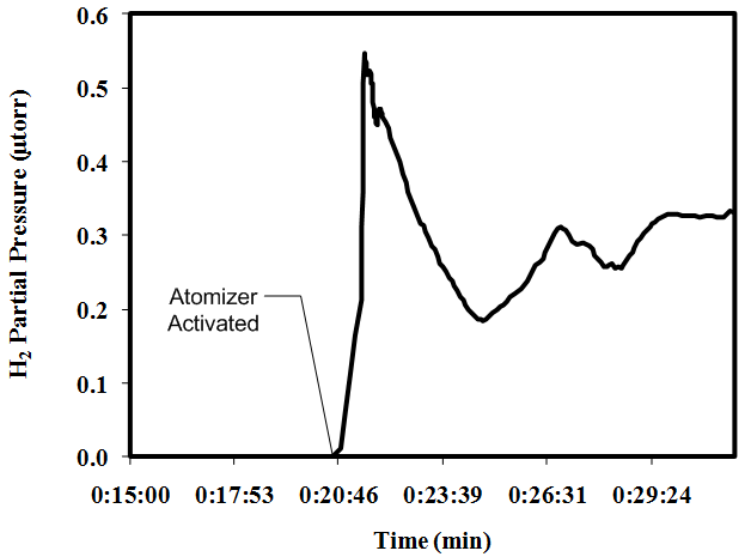

Figure 4.11. Transient response of hydrogen output from DDIR unit cell experimental apparatus after activating atomizer. Interface heater was supplying 2 W under dry conditions and increased to 4 W after activating atomizer.

The steady state results for these experiments are shown below in Figure 4.12 in the form of hydrogen flow rate and compared with model results. The simulation results roughly follow the observed experimental results for applied interface heat above 5 W. However, the simulations overpredict the hydrogen generation rate at higher applied interface heat, even when increasing the convective heat transfer coefficient to 25 W/m^2-K from the baseline value of 15 W/m^2-K calculated from the experimental conditions. There are a few plausible explanations for this: 1) the heat losses in the simulations are underpredicted, 2) hotspots in the catalyst bed in the vicinity of the interface heater cause local catalyst deactivation and reduced conversion, and 3) the specific surface area of the catalyst used in the experiments is lower than the manufacturer reported value used in the simulations. Given all these possible sources of error, the results are in satisfactory agreement. What is most interesting are the experimental results observed below an applied interface heat of 5 W. Below this point, the simulations predict flooding of the

catalyst interface and no hydrogen production. However, the simulations do not account for axial heat transfer from the periphery heater to the interface, so that the actual heat supplied to the interface is higher than reported. Since the power supplied to the periphery heater is constant throughout all experiments, the hydrogen production rate approaches a constant value at low values of applied interface heat. This is estimated by the isothermal catalyst condition at 505 K, also shown in Figure 4.12.

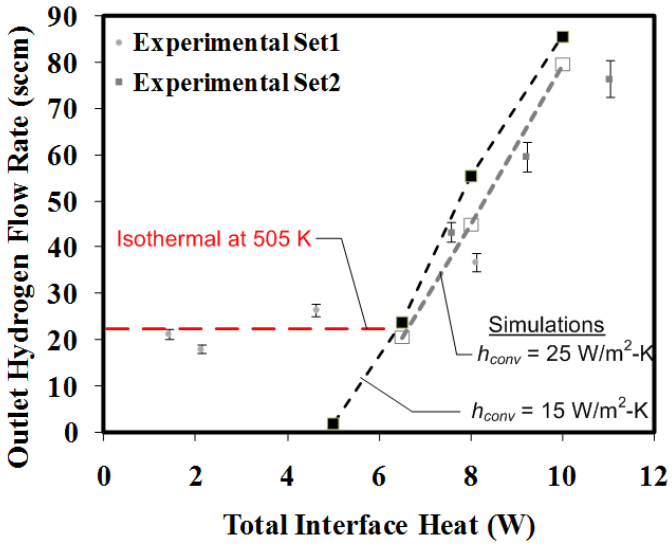

Figure 4.12. Comparison of experimental and model results for hydrogen generation rate from a stream of 27.5 µm droplets delivered at a frequency of 100 kHz impinging on a catalyst bed of 150 mg with applied interface heat varied between 1.5 – 11 W.

4.3 Design and Experimental Demonstration of DDIR for 100 W Fuel Cell

The experiments presented above were carried out primarily to validate the DDIR unit cell model, although a secondary purpose was to demonstrate the practical implementation of a DDIR type reactor. This practical demonstration was extended by designing, constructing, and operating a complete DDIR system with an *array* of droplet generators, which collectively supply hydrogen for use in a fuel cell. The reactor was designed to supply sufficient hydrogen for a 100 W fuel cell, although integration with a fuel cell was not considered in these experiments.

4.3.1 Reactor Sizing for Methanol Steam Reforming

The liquid feed rate, catalyst bed size, and heater capacity were calculated given the 100 W peak power demand. The required hydrogen feed rate, $\dot{n}_H$, to achieve this power demand is estimated by

$$P = \eta_{cell}\Phi_{th} I = \eta_{cell}\Phi_{th}\left(\eta_{an}\dot{n}_H NF\right) \tag{4.4}$$

where Φ_{th} = 1.23 V is the theoretical single cell voltage, N = 2 is the number of electrons generated per molecule of hydrogen, and F = 96500 C/gmol is Faraday's constant. Assuming typical values of utilization at the fuel cell anode, η_{an} = 0.8, and fuel cell efficiency, η_{cell} = 0.6 [81], $\dot{n}_H$ = 8.78x10^{-4} gmol/s. If only the steam reforming reaction occurs at 95% conversion, the required methanol flow rate is $\dot{n}_M$ = 3.08x10^{-4} gmol/s. If the liquid feed at the reactor inlet is 50% molar methanol/water, the total volumetric feed rate (assuming standard conditions) is 0.018 ml/s.

The ultrasonic atomizer described in section 2.1.4 was used in this reactor to supply the liquid feed. The baseline design of this device consisted of a 20x20 array of nozzles of various sizes spaced at 780 μm on a square grid with a nominal operating frequency of 1 MHz, giving a relationship between the desired nozzle size (assumed to be the same as the droplet size) and volumetric flow rate, $\dot{\forall} = 400\left(4/3\right)\pi R_{d,0}^3 f$. The design droplet diameter of 4.4 μm suggested using the closest available size, which was 5 μm.

The catalyst bed cross-sectional area is set by the area of the ultrasonic atomizer, and the required thickness of 20 mm for 95% conversion was calculated using an isothermal plug flow reactor model assuming a bed temperature of 250 ^{o}C. The required heater capacity was set to twice that required to vaporize and heat the liquid feed and

carry out the endothermic steam reforming reaction in order to account for heat losses, which requires a 100 W heater.

4.3.2 Experimental Apparatus

As described above, the reactor consisted of an array of droplet generators and an electrically heated catalyst layer in addition to a gas delivery system as shown schematically in Figure 4.13, and was outfitted with similar measurement and control instrumentation as that employed for the unit cell reactor.

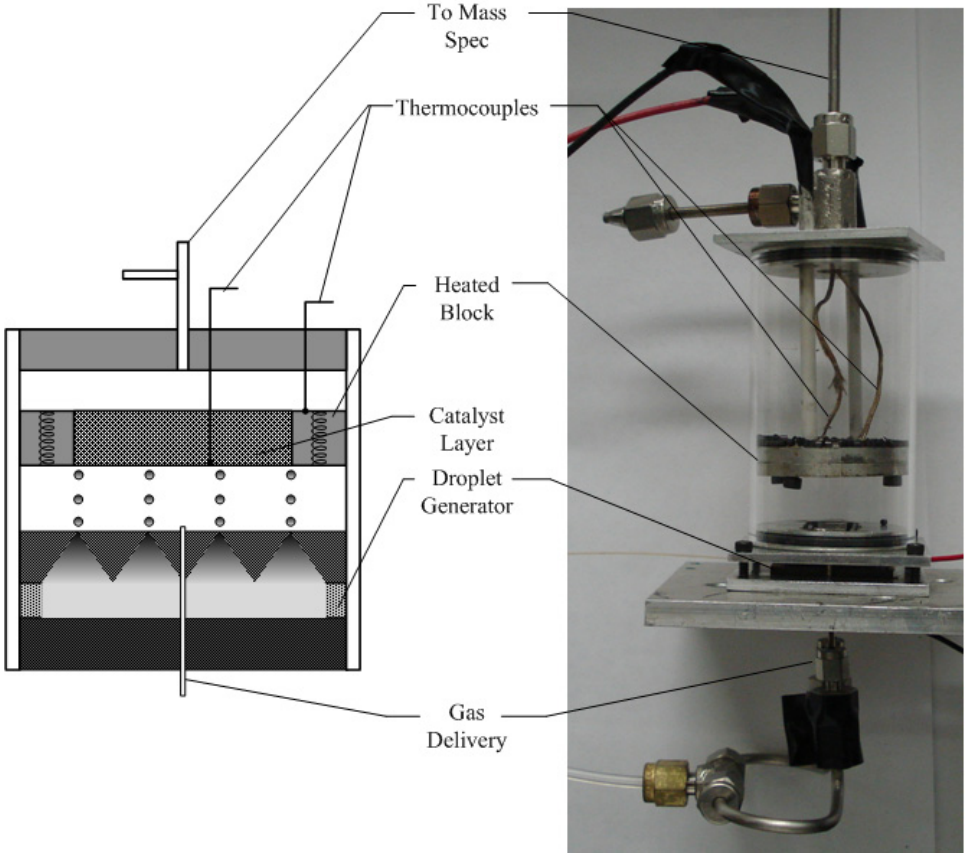

Figure 4.13. Reactor used for 100 W capacity DDIR experiments. Both a schematic and photo are shown.

The piezoelectric used to power the ultrasonic atomizer was P-880 from American Piezo, Inc. with dimensions 28 mm x 24 mm x 2 mm driven with a Agilent 33250A function generator amplified with a T&C Power Conversion Ultra 2020 RF Amplifier. Liquid flow rate control was achieved by operating the atomizer in a burst mode and varying the duty cycle. The liquid flow rate was also monitored by storing the liquid feed in a graduated buret and recording the liquid level at regular intervals throughout the experiment to get an average flow rate. This is necessary because on most occasions only a fraction of the nozzles on the ultrasonic atomizer were actively ejecting droplets.

The catalyst used in the reactor was BASF F3-01 Cu/Zn reforming catalyst in its original 1.5 mm x 1.5 mm pellet form. The catalyst rested in a cavity in an aluminum block and held in place by a copper mesh with a 100 μm opening size. Heaters were constructed by winding 30 AWG nickel-chromium alloy wire around a 1/16" O.D. x 1.5" L ceramic tube. Four of these heaters were connected in series around the periphery of the aluminum block. Two thermocouples were used to monitor the temperature at the copper mesh where the droplets impinge and also at the periphery of the heated block. A Harrick ATC low voltage temperature controller was used in conjunction with the two thermocouples to power the heaters and maintain the desired temperature at the mesh.

Gas was delivered to the impingement plane via two perforated 1/16" stainless steel tubes such that the gas comes out parallel to the ejected droplets. In all cases, 200 sccm argon was fed into the reactor with the same system described above in Section 4.2.1, providing a reference for product gas analysis. For autothermal reforming, air was pumped into the reactor using a Hargraves (M/N E129-13-120) miniature reciprocating

pump. A Cole Parmer 65mm rotameter monitored the flow rate of air entering the system.

Analysis of the product gases was carried out with a Hiden HPR20 quadrupole mass spectrometer. Separate experiments were run to establish the relative sensitivity of the detector to hydrogen, water, and methanol compared to argon by individually feeding each of these species with argon at known flow rates. The partial pressures of the product species were then converted to molar flow rates using the flow rate and partial pressure of the argon reference.

Upon reactor startup, the catalyst was heated to 200^{o}C and reduced by flowing a 5% H_2 in Ar mixture at 200 sccm for one hour. The gas flows were then set to the desired values for the experiment and the reactor and mass spectrometer are allowed to settle for at least 10 minutes. The droplet generator was turned on and the reactor is visually inspected to ensure that the droplets are impinging on the catalyst bed.

4.3.3 Methanol Steam Reforming Experiments

Several methanol steam reforming experiments were performed with catalyst bed temperatures between 200-240 ^{o}C and at a catalyst loading of 20 g. At each temperature, the flow rate from the ultrasonic atomizer was varied by adjusting the duty cycle in burst mode operation. The results of these experiments are summarized in Figure 4.14 below. For temperatures of 220 and 240 ^{o}C, the results show an increase of conversion with W/F as expected, but are still below the conversion for an ideal 200 ^{o}C PFR. At 200 ^{o}C, even more scatter in the data was observed. The primary reason for this was that significant deflection of the droplets from a straight line path occurred, resulting in condensation on the side walls. Thus, a significant fraction of the liquid feed did not contact the catalyst bed, resulting in much lower conversion than expected.

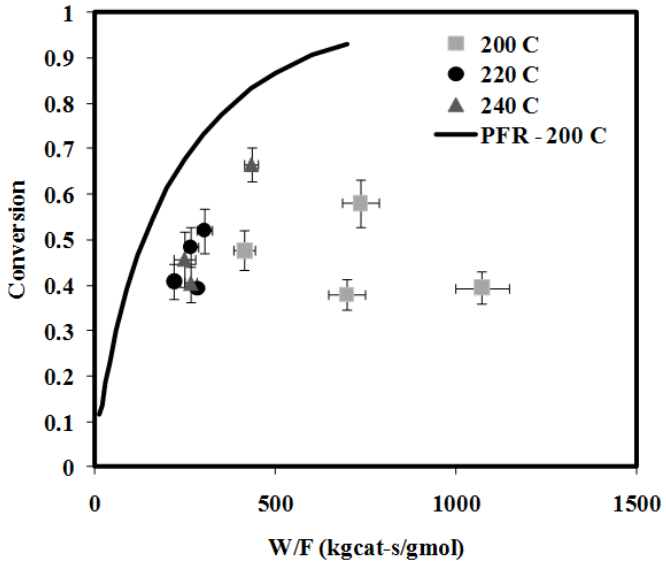

Figure 4.14. Conversion for initial methanol steam reforming reaction experiments on 100 W DDIR compared with isothermal plug flow reactor at 200 ^{o}C. Temperature range between 200-240 ^{o}C and catalyst loading 20 g for all cases.

Figure 4.15 shows that a significant amount of CO appears in the product stream. The primary reason for this is the high temperature observed at the edge of the catalyst bed, which increases the rate of the methanol decomposition reaction relative to steam reforming, and increasing the amount of CO in the products. Improved distribution of the heat throughout the catalyst bed would reduce the CO in the product stream. This is investigated further in Chapter 5.

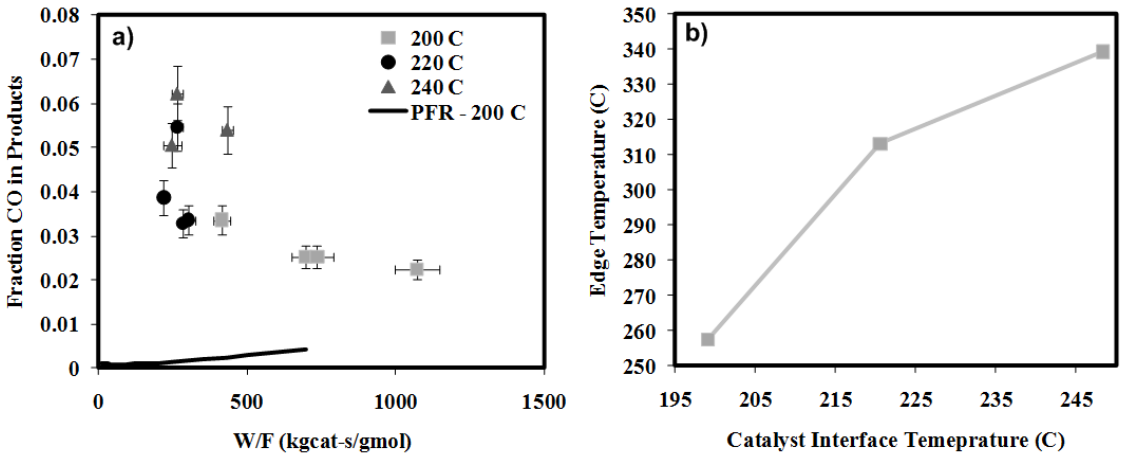

Figure 4.15. a) Fraction of CO in products for different reaction temperatures and W/F. b) Measured temperature at edge of catalyst bed compared to the temperature at the center of the catalyst bed, showing the spatial temperature variation.

To ameliorate some of the problems with droplet deflection, 1) the applied voltage to the piezoelectric transducer was increased to increase the ejected droplet velocity, and 2) the catalyst layer was brought closer to the atomizer surface. This modified configuration was then utilized to run methanol steam reforming experiments at 200 ^{o}C with catalyst loading varied between 1 – 10g, and the atomizer run at a constant 100% duty cycle. The results of these experiments were then compared with experimental studies of portable methanol steam reformers presented in the literature, which demonstrates the feasibility of the DDIR concept for this reaction. Figure 4.16 shows the conversion vs. catalyst mass to fuel flow rate ratio (W/F) for these experiments and the portable methanol steam reformers described in [17, 18, 82] at 200 ^{o}C. Even with the aforementioned improvements in the droplet delivery, significant variations in droplet delivery rate occurred within each experiment and from experiment to experiment. These variations highlight the need to address the reliability of the droplet generator to ensure repeatable operation.

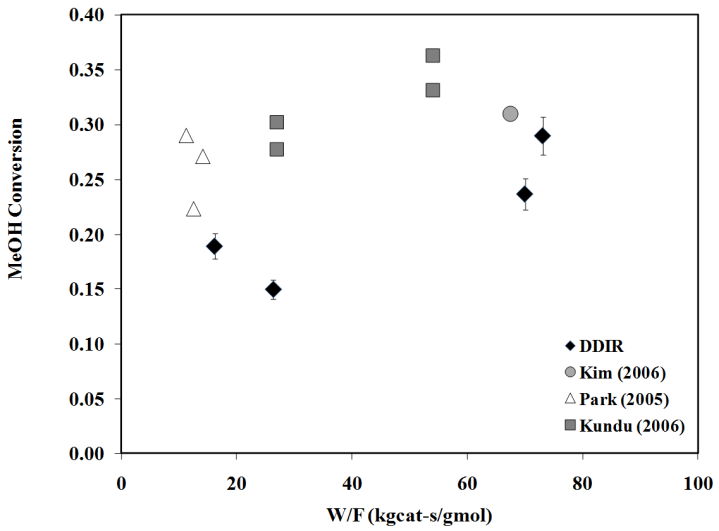

Figure 4.16. Comparison of methanol conversion in proof of concept DDIR for methanol steam reforming with selected literature results at 200 ^{o}C.

4.3.4 Demonstration of Autothermal Reforming

Autothermal reforming of methanol was also demonstrated using the DDIR. To achieve autothermal operation, the feed rates of air, methanol, and water must be in the correct ratio so that the heat liberated by partial oxidation is sufficient to vaporize the liquid feed and drive the endothermic steam reforming as given in eq. (2.5), which was used to calculate the ratio of methanol to water in the feed, assuming 20% of the total heat generated by the exothermic reaction was lost to the environment. The stoichiometry of the partial oxidation was then used to calculate the required air feed rate.

The reactor was preheated to 300 ^{o}C using the electrical heaters with a mixture of air flowing at 300 sccm and argon at 150 sccm flowing into the reactor via the gas delivery tubes. The acoustic atomizer was then activated to introduce a 5:1 by volume methanol/water mixture. Figure 4.17 shows the time variation of the power input to the heaters along with the interface temperature and product distribution.

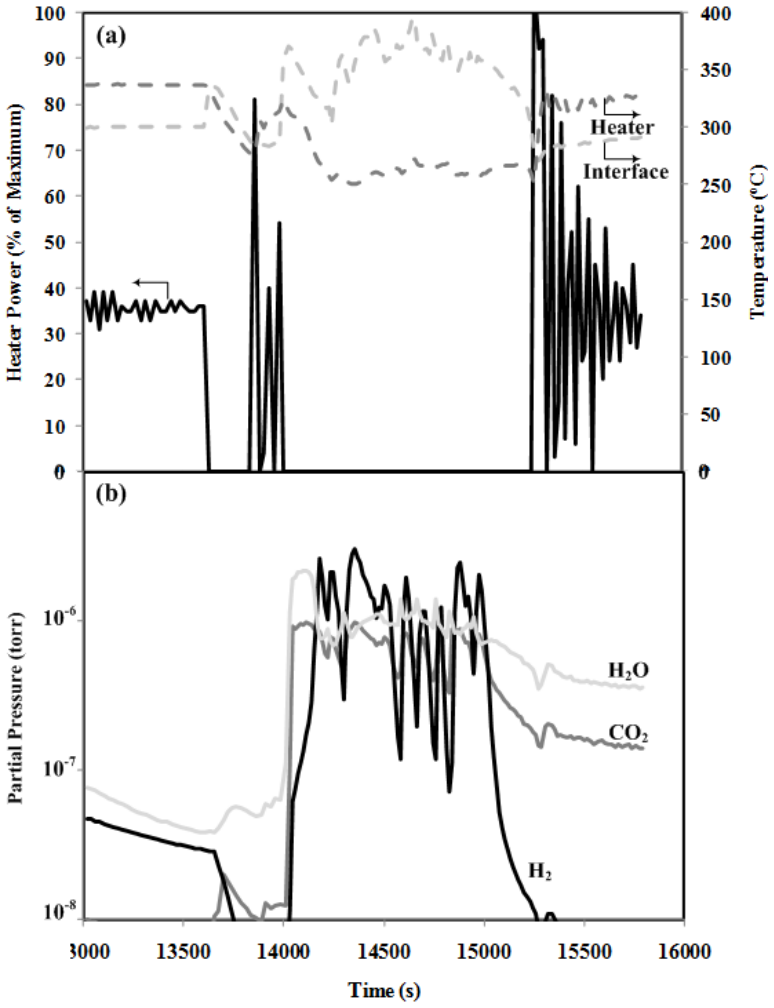

Figure 4.17. Results from methanol autothermal reforming experiment using proof-of-concept DDIR, a) power input to heater and measured temperatures, b) partial pressure of species measured at reactor outlet.

These results show that the upon ejection of the liquid mixture onto the catalyst layer at approximately 14000 s, the automatic temperature controller turned off power to the heaters, the interface temperature increased from 300 ^{o}C to between 350-400 ^{o}C, and hydrogen was observed at the reactor outlet. This behavior was sustained for over 10 min until ejection of the liquid fuel mixture was ceased. Since there was no power supplied to the heaters during this period, it is clear that autothermal operation of the DDIR was achieved. Additionally, the temperature at the catalyst interface was between 50-100 ^{o}C

higher than the temperature measured at the heater, suggesting that all heat was generated from the exothermic reaction at the catalyst interface. Although sustained autothermal reforming was achieved, these results also show large oscillations in both the interface temperature and product composition. Also, a significant amount of excess water was observed in the products, indicating that the fuel feed was not at the optimal ratio.

The results obtained from the macroscopic DDIR for methanol steam reforming and autothermal reforming clearly demonstrate the feasibility of the concept for both of these reactions. For the steam reforming reaction, the conversion for a given W/F ratio observed for the DDIR is comparable to selected literature results for portable MSR reactors. Autothermal reforming was demonstrated with the DDIR, but also displayed unexpected oscillations in temperature and product composition. These results suggest that a more careful study of the design parameters for the DDIR should be carried out to optimize the reactor design

CHAPTER 5

REACTOR SIMULATIONS AND IDENTIFICATION OF OPERATING REGIMES

5.1 Ideal Performance Limits for Methanol Steam Reforming

To establish a baseline for comparison and ideal limits for reactor performance, an isothermal plug flow reactor (PFR) model is used to calculate quantities of interest for temperatures between 473-573 K. This temperature range corresponds to the suggested operating range reported in the literature for Cu/Zn based methanol steam reforming catalysts [76]. The isothermal plug flow equations are simply a balance between advection of species and reaction along the length of the reactor and the molar flux of any species, n_i'', along the reactor length is found by the following equation.

$$\frac{dn_i''}{dz} = \sum_j \nu_{ij} r_j \tag{5.1}$$

In using this simplified model, diffusion of species is neglected, which at low Peclet number (Pe) can result in significant errors. In a real reactor with low Pe the reaction products diffuse back toward the reactor inlet, where they competitively adsorb on the catalyst surface, decreasing the reaction rate. Assuming an isothermal bed can also lead to significant deviation from actual results since the thermal conductivity of the catalyst bed is typically low (~1 W/m-K).

Despite these shortcomings, the simple nature of the isothermal plug flow model is quite valuable in establishing expected performance limitations. For example, the

upper limit on the power output for a fuel cell fed with the reactor product stream can be estimated by $P_{out} = \dot{n}_{H2} LHV_{H2}$, where $\dot{n}_{H2}$ is the molar flow rate of hydrogen at the reactor exit and LHV_{H2} is the molar lower heating value of hydrogen gas. A lower limit for the heat input required to run the reactor, Q_{in}, is calculated by considering only the power input required to vaporize and heat the feed and to drive the endothermic reaction, assuming that no heat is lost to the surroundings.

$$Q_{in} = \dot{n}_f \left(\sum_{i=M,W} x_i \left[\overline{h}_{fg,i} + \overline{c}_{p,g,i} \left(T_{rxn} - T_{sat} \right) \right] + x_M \Delta H_{rxn} \right) \tag{5.2}$$

Here, $\dot{n}_f$ is the molar flow rate of the reactant feed, the subscripts M and W refer to methanol and water, respectively, and $\overline{h}_{fg,i}$ and $\overline{c}_{p,g,i}$ are the molar heat of vaporization and molar specific heat, respectively. Thus, upper limits on the efficiency, $\eta = \left(P_{out} - Q_{in} \right) / \dot{n}_f \, x_M LHV_M$, and volumetric power density, $\omega = \left(P_{out} - Q_{in} \right) / \forall_r$ are established, where $\forall_r$ is the volume of the reactor. Additionally, the performance metrics of methanol conversion, X_M, and selectivity to methanol steam reforming, $S_{CO2/CO}$, are defined as usual.

$$X_M = 1 - \frac{\dot{n}_{M,out}}{\dot{n}_{M,in}} \tag{5.3}$$

$$S_{CO2/CO} = \frac{\dot{n}_{CO2,out}}{\dot{n}_{CO,out}} \tag{5.4}$$

The results for 95% methanol conversion are summarized in Figure 5.1 below and are not only used as a baseline for comparison, but also to estimate the required catalyst bed size for a given flow rate of droplets in the DDIR.

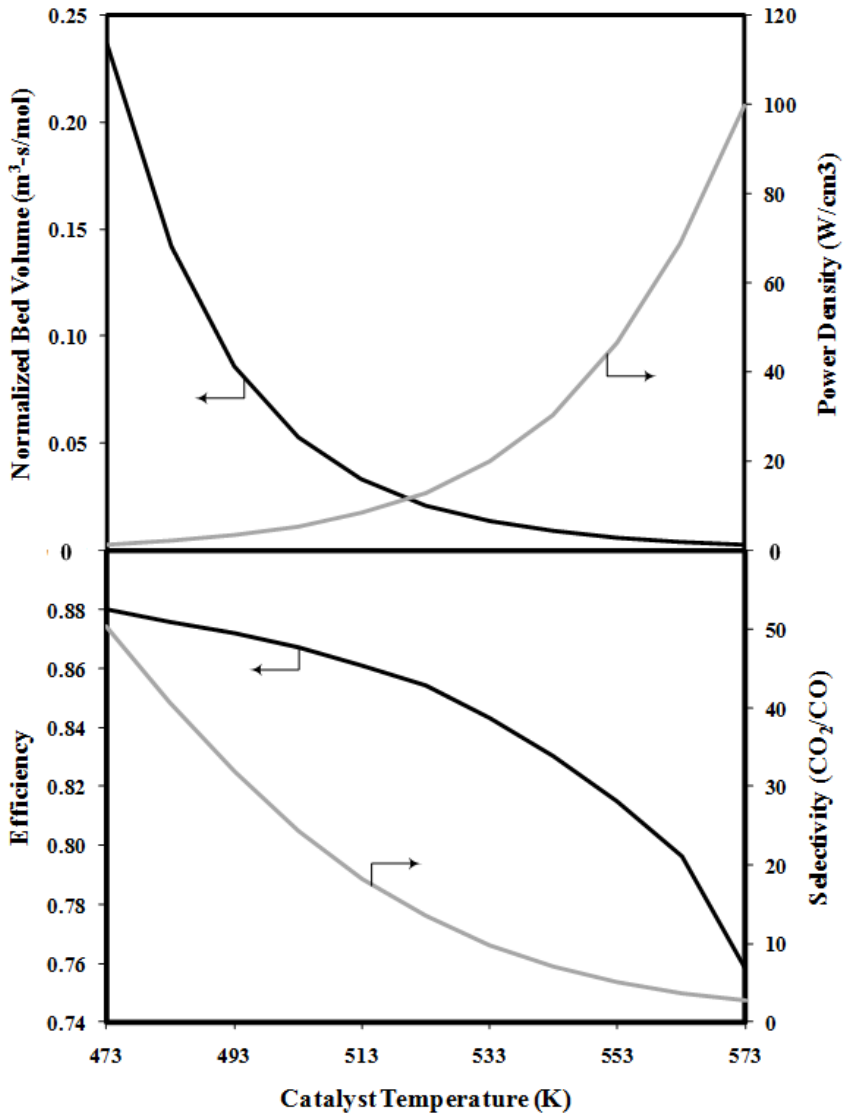

Figure 5.1. Size requirements and ideal operating limits for methanol steam reforming reaction carried out in isothermal plug flow reactor with 95% conversion in the temperature range 473-573 K.

At lower temperatures, selectivity to steam reforming is high so that more hydrogen is produced per unit of fuel consumed and less heat goes to raising the vaporized feed to reaction temperature. Thus, η is higher at lower reactor temperatures, but the power density drastically increases at higher temperatures due to the exponential dependence of the reaction rate on temperature, resulting in a corresponding increase in hydrogen production per unit volume of catalyst bed. This, however, is accompanied by

increased CO at the reactor outlet and a decrease in efficiency due to the increased heat required to bring the reactants to reaction temperature. From a practical perspective, the heat losses would also significantly increase as the operating temperature increased. Catalyst bed temperatures above 573 K are not considered due to rapid deactivation of the catalyst as a result of sintering [48].

Examining the reactor performance at a fixed temperature of 523 K with varying catalyst bed volume also reveals some design tradeoffs. At low W/F, insufficient hydrogen is produced to break even and supply the required heat input for the reactor, so the power density is zero. The power density then begins to increase, goes through a maximum and begins to decrease as the amount of hydrogen produced per unit volume of reactor continues to decrease further downstream as the reaction rate decreases. The selectivity similarly decreases with increasing W/F because the increasing presence of H_2 and CO_2 from the steam reforming reaction leads to an increase in the reverse water gas shift reaction, producing CO. From a size minimization perspective, it is desirable to run the reactor at the W/F value that maximizes the power density, which also corresponds to a high selectivity. However, operating the reactor at this point would result in very low fuel utilization since the conversion here is less than 50%. These basic trends apply to all temperatures in the catalyst operating range (473 – 573 K).

Without a mechanism to recycle the unutilized feed and bring it back to the reactor inlet, it is impractical to operate at maximum power density because much of the fuel is wasted. Most proposed portable fuel reforming devices have targeted high conversion (and thus high efficiency) operation, sacrificing power density for fuel utilization, a tradeoff which was discussed in detail by Harold and Nair [40]. In fact, a

review of the literature has not yielded any serious attempts to recycle the unused feed in portable reforming devices, although Mitsos [83] considers the possibility of fuel recycling in a conceptual design of portable fuel reformers. One possibility would be to run the outlet feed (products + unreacted gases) through a cold trap to condense the feed and bring it back to the fuel reservoir. Of course, consideration must also be given to the increase in system size and complexity involved in implementing a feed recycle system. For the purposes of this study, feed recycle is not considered, and the catalyst bed volume for a required fuel throughput would then be set by determining a minimum acceptable conversion level.

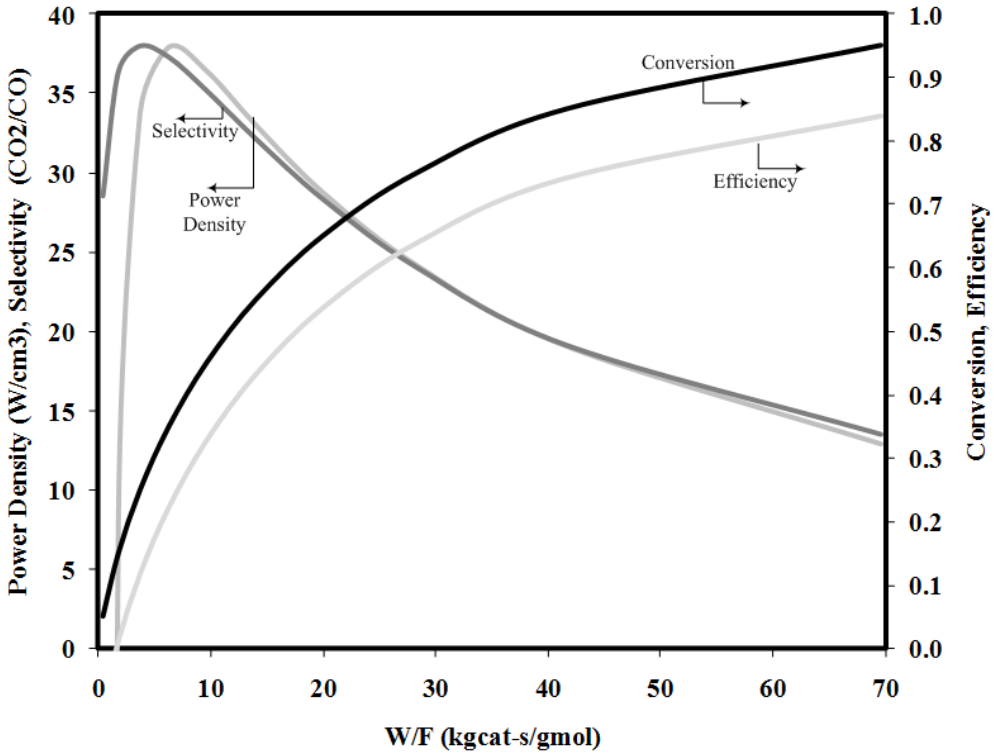

Figure 5.2. Power density, selectivity, and conversion as a function of catalyst mass to molar fuel flow ratio for methanol steam reforming carried out in an isothermal plug flow reactor at 523 K.

5.2 Baseline DDIR Simulation for Steam Reforming

As a baseline case, consider 20 μm droplets delivered at a frequency of 100 kHz with an initial velocity of 5 m/s. This ensures that the droplet stream impinges on the catalyst interface and does not experience any mass loss due to vaporization. These effects are further investigated below. The required catalyst bed volume for 95% conversion for a unit cell is estimated from the isothermal plug flow reactor results above assuming that the entire bed is at 523 K (optimum for steam reforming). Of course this is not possible for the real reactor due to the relatively low thermal conductivity of the packed bed (k_s ~ 1.0 W/m-K), which is seen in the results below. Another consideration that is inconsequential for the isothermal plug flow reactor is the aspect ratio ($AR = H_{cat}/R_{cell}$) of the unit cell. This becomes important for the DDIR since it will determine how much of the catalyst interface is covered by the liquid film, how effectively the heat supply is distributed throughout the catalyst bed, and the reactor Peclet number (Pe) for a given throughput, which plays in important role in reactor performance. Here, the Peclet number is defined with the velocity scale determined by the total mass flow rate of droplets, $\dot{m}_d = (4/3)\pi R_{d,0}^3 \rho_l f$, and the reactor cross-sectional area.

$$Pe = \frac{uH_{cat}}{D_e} = \left(\frac{\dot{m}_d}{\pi R_{cell}^2}\right)\left(\frac{H_{cat}}{D_e}\right) \tag{5.5}$$

For this baseline case, an aspect ratio of 1.5:1 is investigated with a W/F = 72 kgcat-s/gmol, matching that required for 95% conversion in the isothermal plug flow reactor at 523 K, which results in catalyst bed dimensions of R_{cell} = 4 mm and H_{cat} = 6 mm. The total heat supplied to the reactor is found from eq. (5.2) to be Q_{in} = 0.99 W and distributed uniformly along the catalyst interface so that the interface heat flux is 1.97

W/cm^2. The parameters used in the baseline case are summarized in Table 5.1 below.

Table 5.1 Operating Parameters for Baseline DDIR for methanol steam reforming

Parameter	Description	Value
$R_{d,0}$	Initial droplet radius (μm)	10.0
$V_{d,0}$	Initial droplet velocity (m/s)	5.0
$T_{d,0}$	Initial droplet temperature (K)	300
$X_{M,d,0}$	Initial droplet methanol mole fraction	0.5
q''_{int}	Heat flux at catalyst interface (W/cm^2)	1.97
q''_w	Heat flux at unit cell periphery (W/cm^2)	0
R_{cell}	Unit cell radius (m)	0.004
H_{cell}	Distance from droplet generator to catalyst (m)	0.001
H_{cat}	Length of catalyst bed (m)	0.006
ε	Catalyst porosity	0.3
d_p	Catalyst average particle size (mm)	0.1
k_s	Catalyst thermal conductivity (W/m-K)	1.0

The hydrodynamic behavior for the baseline case is depicted in Figure 5.3, which shows streamlines and contours of velocity magnitude and pressure in the region surrounding the catalyst interface. In this figure and all others, the droplets emanate from the left-center of the figure and travel to the right, and the catalyst interface is denoted by the vertical line dividing the accumulated liquid film. Figure 5.3 shows that a recirculation zone is created in the space between the droplet generator and catalyst interface due to the continuous supply of droplets moving along the unit cell axis. This recirculation zone exhibits a high velocity close to the axis where the stream of droplets creates a strong flow entrainment that slows rapidly with radial distance from the axis. Streamlines also emerge from the liquid film interface inside the catalyst layer due to vaporization and are driven normal to the isobars, which results in backflow of some of the vapor generated from the liquid film, causing a radial flow in the space between the atomizer and catalyst, before the flow reenters the bed near the unit cell edge.

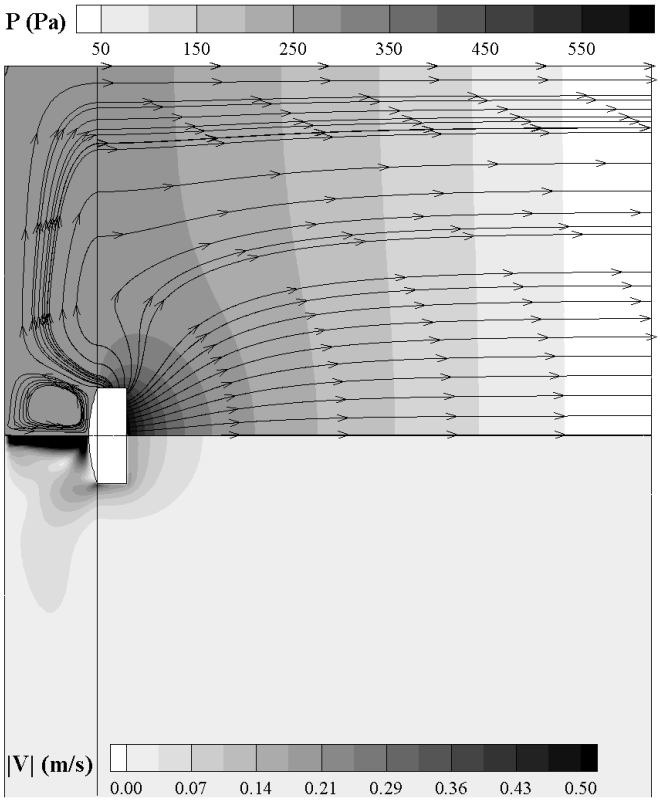

Figure 5.3. Streamlines and contours of pressure and velocity magnitude for baseline case in region directly surrounding the accumulated liquid film.

The temperature profile is shown in Figure 5.4 (a) along with the rate of methanol steam reforming. Along the unit cell axis, the temperature remains close to the initial droplet temperature since the continuous droplet stream acts to cool the surrounding gas. As a result, the droplet temperature also remains unchanged as it travels to the catalyst interface and impinges on the liquid film. A strong radial temperature gradient is observed near the catalyst interface due to the high heat load imposed by vaporization at the liquid film interface. Since the vapor leaving the liquid film interface is at its saturation temperature, measurable reaction rates are not observed close to the film interface because sensible heating of the vapor must occur before it reaches suitable reaction temperature. Thus, the portion of the catalyst bed covered by the liquid film and its immediate vicinity are unutilized. Examining the flow pattern in Figure 5.3 shows that

the vapor generated at the film interface that enters the droplet transit zone, re-enters the catalyst bed towards the unit cell edge. Additionally, the bed temperature exceeds 570 K at this point since the heat is supplied along the catalyst interface, resulting in all reaction rates being highest in this region. This hotspot results in increased carbon monoxide formation due to methanol decomposition, but this is partially ameliorated due to the water gas shift reaction at the same spatial location.

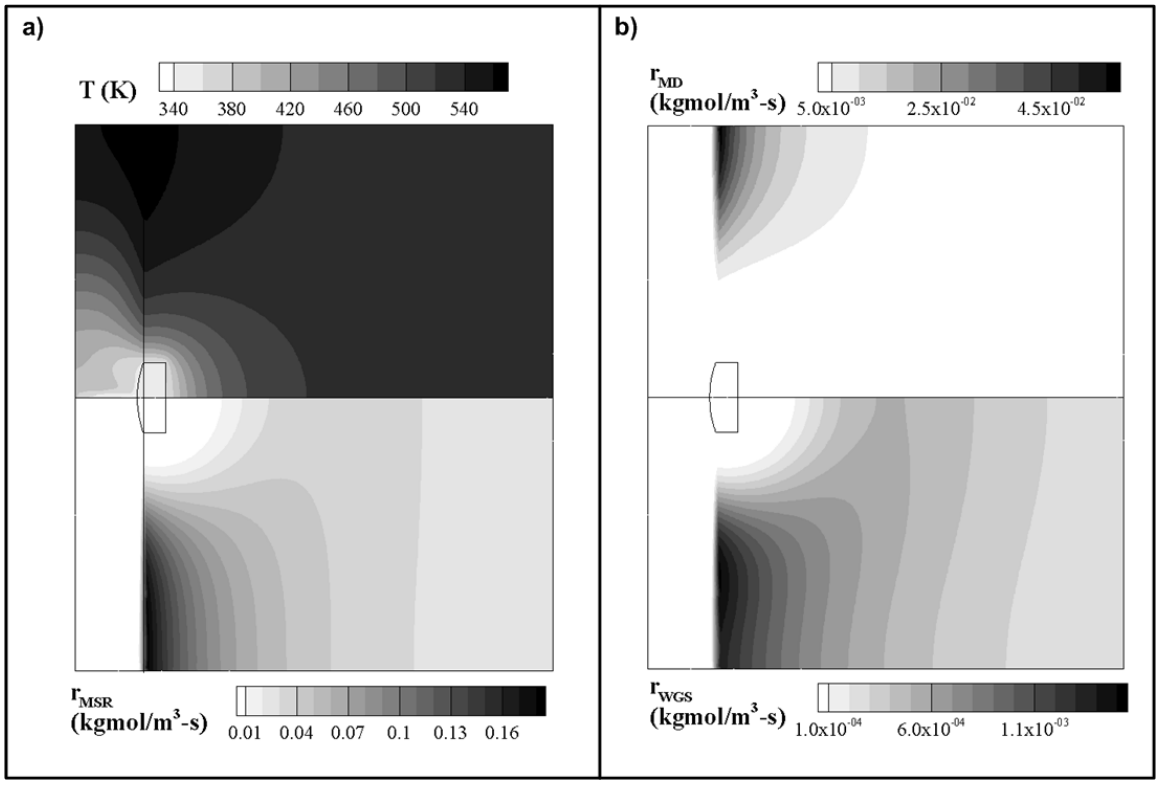

Figure 5.4. (a) Contours of temperature and rate of methanol steam reforming reaction, and (b) rates of methanol decomposition and water gas shift reactions for baseline DDIR-MSR case.

Away from the catalyst interface, the bed approaches isothermality close to the target design value of 523 K. In this region of the catalyst bed, the methanol steam reforming reaction rate is dominant over the decomposition and water gas shift reactions as expected. Furthermore, the steam reforming reaction rate decreases downstream in the catalyst bed as the concentrations of methanol and steam drop.

Comparing the baseline DDIR performance with that of the isothermal plug flow reactor reveals expected deficiencies, which are summarized in table 5.2 below. The obvious reason for the lower conversion in the DDIR is that a significant portion of the catalyst bed is covered by the liquid film and unutilized. Here, the volume of the liquid covering the catalyst is only 0.08% of the total bed volume, so this contributes a small amount to the decreased performance. However, consider that the volume of catalyst below 500 K surrounding the liquid film accounts for 20% of the overall bed volume, which explains the decreased conversion. As a result, less hydrogen is produced per unit of fuel input compared with the isothermal PFR, resulting in lower efficiency and power density. The lower selectivity and higher CO in the outlet of the DDIR is explained by the hotspot along the catalyst interface, which increases the rate of methanol decomposition reaction relative to the steam reforming reaction.

Table 5.2. Comparison of baseline DDIR for methanol steam reforming reaction with the equivalent isothermal plug flow reactor. For both cases, W/F = 72 kgcat-s/gmol, $Q_{in} / \dot{m}_{in}$ = 2.8 MJ/kg.

	MeOH Conversion	**$S_{CO2/CO}$**	**Outlet CO (%)**	**Efficiency (%)**	**Power Density (W/cm^3)**
Isothermal PFR	0.95	13.5	1.8	84	12.9
DDIR	0.69	9.3	3.1	55	8.19

5.2.1 Effect of Unit Cell Aspect Ratio

The effect of the catalyst bed aspect ratio on reactor performance is investigated by holding the catalyst bed volume, droplet delivery rate, and total heat input constant and equal to the baseline case presented above, and varying the aspect ratio ($0.75 < AR < 9$) . All other properties and operating parameters are unchanged from the baseline case. Figure 5.5 shows that as the aspect ratio is increased, the maximum temperature at the catalyst interface increases, which is expected since the same total heat rate is applied

within a smaller area. At the same time, the average temperature over the entire catalyst bed decreases because the thermal resistance in the axial direction increases. In other words, a larger portion of the catalyst bed is further from the heat source at the interface as *AR* increases. Despite the decrease in average bed temperature with *AR*, monotonic increases in both conversion and power density are observed. This occurs because of the exponential dependence of reaction rate on temperature coupled with higher interface temperatures with increasing *AR*, causing increased hydrogen production.

However, the practical consideration of catalyst deactivation must be accounted for when examining these results. Recalling the maximum catalyst operating temperature of 573 K suggests that increasing the aspect ratio beyond a value of 2 will result in deactivation of the catalyst in the vicinity of the heater and the power density and conversion will most certainly be lower than the values computed by the simulations. These effects could be accounted for via a modified kinetic model, which appropriately modifies the reaction rate in regions exceeding the suggested operating limits. Deactivation models for the $Cu/ZnO/Al_2O_3$ steam reforming catalyst exist in the literature [47, 84], which could be applied to this model to estimate the decrease in reaction rate at elevated temperatures. However, such a model is not incorporated here because of limited applicability of these semi-empirical models and lack of generality. As a result the findings should be interpreted carefully where the catalyst bed temperature exceeds 573 K.

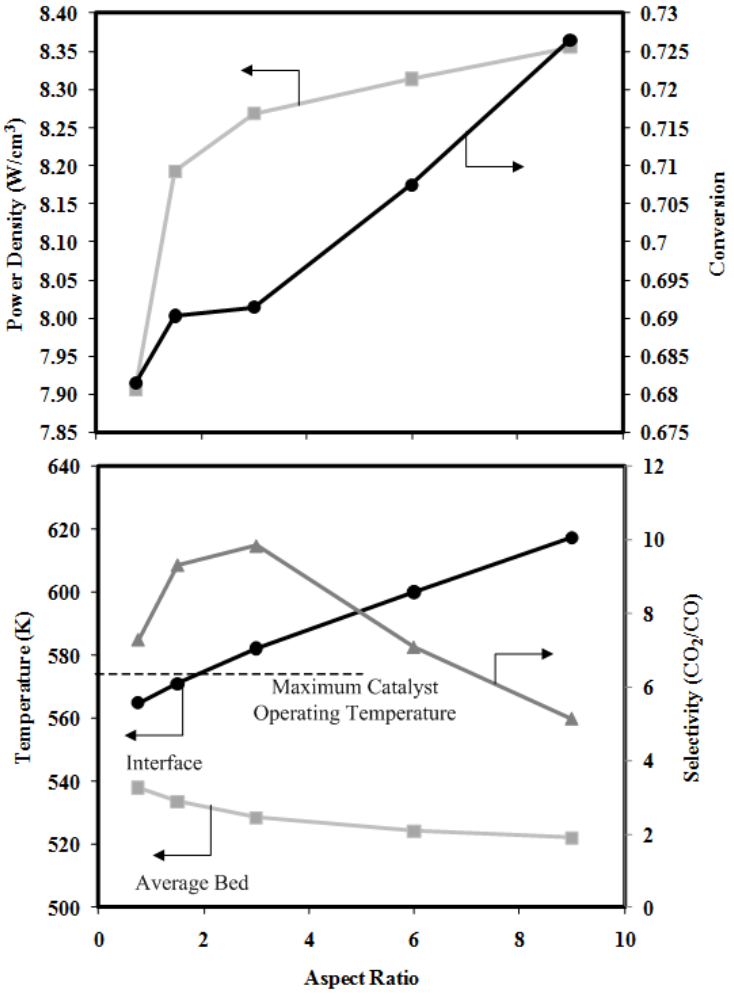

Figure 5.5. Effect of changing unit cell aspect ratio on catalyst interface temperature, selectivity to methanol steam reforming reaction, power density, and methanol conversion. W/F = 72 kgcat-s/mol and $Q_{in} / \dot{m}_{in}$ = 2.8 MJ/kg for each case.

The selectivity to steam reforming displays a more interesting trend with aspect ratio. One would expect that the increased interface temperature at larger *AR* would result in a monotonically decreasing selectivity with *AR*, but the selectivity achieves a maximum at $AR \cong 3$ before decreasing at higher *AR*. Examining contour plots of hydrogen mole fraction and fractional yield (defined as the local ratio of the rates of steam reforming to decomposition, r_{MSR}/r_{MD}) in Figure 5.6 shows that the mole fraction of hydrogen is higher near the catalyst interface for the lower *AR* case. The inhibiting

effect of hydrogen on the steam reforming reaction causes a decrease in the fractional yield such that its average is lower over the entire catalyst bed for lower *AR*, which results in a lower selectivity. Physically, this occurs because diffusional transport becomes dominant over advective transport and the resulting dispersion of the products causes the mole fraction of products near the catalyst interface to increase.

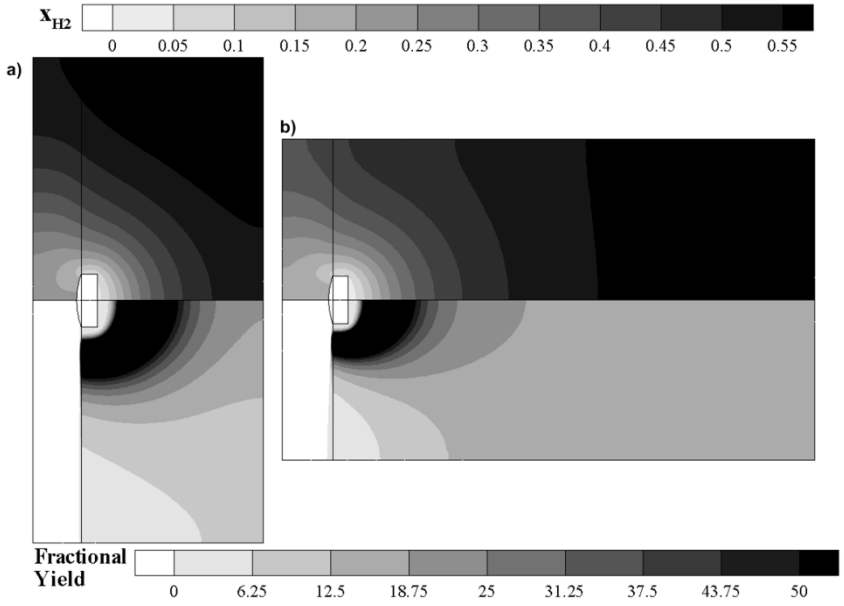

Figure 5.6. Contours of hydrogen mole fraction and fractional yield for a) $AR = 0.75$, b) $AR = 3$. $\dot{m}_d = 3.5\text{x}10^{-7}$ kg/s W/F = 72 kgcat-s/mol and $Q_{in} / \dot{m}_{in} = 2.8$ MJ/kg for each case.

This interpretation of the variation in selectivity with aspect ratio is supported by considering the results for the two limiting cases 1) Pe $\rightarrow$ 0 and 2) $k_e \rightarrow \infty$, which are shown in Figure 5.7. These results are obtained by rerunning the simulations for each aspect ratio value above with exactly the same values except 1) setting a constant mass diffusion coefficient equal to $1\text{x}10^{-10}$ m^2/s, and 2) changing the solid thermal conductivity from 1 W/m-K to 10 W/m-K. For case 1) where Pe $\rightarrow$ 0, the dispersion of products at lower aspect ratio is virtually eliminated and a monotonically decreasing selectivity is

observed as expected. For case 2) where $k_e \rightarrow \infty$, diffusion still dominates over advection at lower *AR*, but as *AR* increases, isothermal plug flow behavior is approached. The situation in the real reactor can be roughly thought of as a combination of these two ideal cases where the selectivity is controlled by back diffusion of products at low *AR*, and by thermal resistance of the catalyst bed at high *AR*.

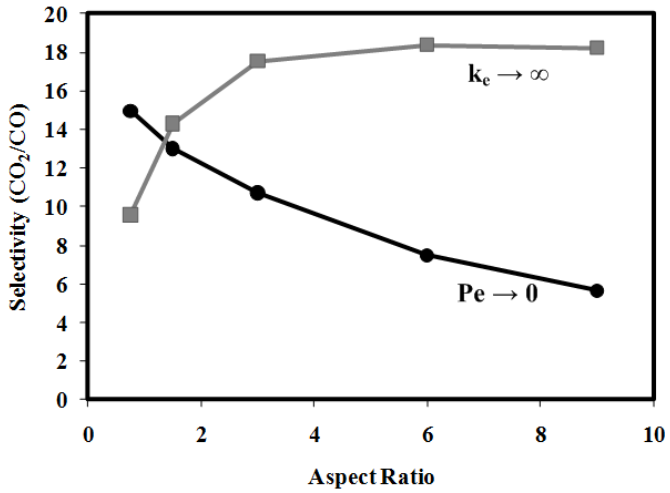

Figure 5.7. Variation of selectivity to methanol steam reforming with aspect ratio for the limiting cases Pe → 0 and $k_e \rightarrow \infty$.

5.2.2 Effect of Heater Distribution

As mentioned in the above discussion, as the DDIR unit cell aspect ratio increases, the interface temperature increases, leading to a low selectivity and large axial temperature gradient in the catalyst bed. The performance of the high aspect ratio unit cell could be improved by instead deploying the heater at the unit cell periphery, a configuration that was mentioned in section 2.2. Thus, heat would be spread along the entire length of the unit cell so that it is delivered close to the point of consumption by endothermic chemical reaction. Attention is confined to the case where the heat flux is constant along the unit cell periphery, which is the situation for an electrical resistance heater uniformly distributed so that each unit cell becomes its own miniature reactor.

Consideration must still be given to the fact that the heat load is higher at the interface due to liquid vaporization and higher rate of reaction. For this reason, simultaneously deploying separate heaters at both the interface and along the unit cell periphery is also studied. In this configuration, the heat applied at the interface is equal to that required to vaporize the liquid feed and heat it to reaction temperature while the heat applied along the periphery is equal to the heat required to drive the endothermic steam reforming reaction. Thus the heat fluxes at the interface, q_i'', and periphery, q_w'', are

$$q_i'' = \frac{(4/3)\pi\rho_l R_{d,0}^3 f\left[h_{fg} + c_{p,g}\left(T_{rxn} - T_{sat}\right)\right]}{\pi R_{cell}^2} \tag{5.6}$$

$$q_w'' = \frac{(4/3)\pi\rho_l R_{d,0}^3 f y_{MeOH}\Delta H_{MSR}}{2\pi R_{cell} H_{cat}} \tag{5.7}$$

All three heater configurations are examined for *AR* ranging from 1.5 – 9 with the same total heat supplied in each case with all other conditions equal to those studied in section 5.2.1, where the heat was all supplied at the catalyst interface. These results are summarized in Figure 5.8. At low aspect ratio where the thermal resistance is low, the effect of heater arrangement on performance is less pronounced.

When heat is supplied only at the edge of the catalyst bed, the peak bed temperature decreases as *AR* increases, resulting in decreased power density. Furthermore, flooding occurs for $AR > 5$ because the total heat (which is constant for all cases) is spread over a larger area, so the heat flux near the interface is insufficient to vaporize the impinging droplets. It is also likely that flooding will also occur if *AR* drops below a certain threshold level because the increased radial thermal resistance will cause the accumulated liquid to spread out more, although this is not confirmed via simulations.

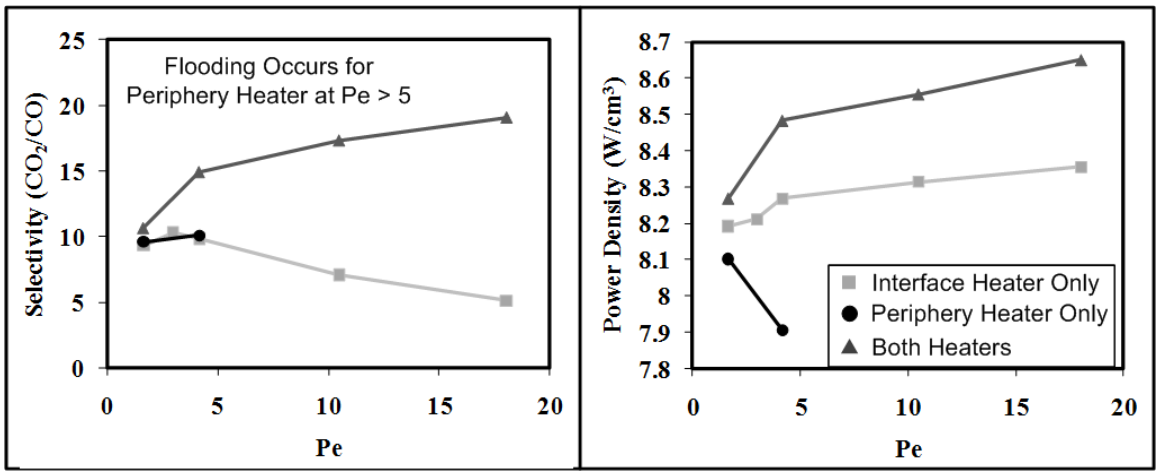

Figure 5.8. Effect of heater placement in DDIR unit cell on (a) selectivity and (b) power density. Equal total heat rates were applied uniformly at the catalyst interface, unit cell boundary, or split between the two as described above. For all cases, W/F = 72 kgcat-s/gmol, and $Q_{in} / \dot{m}_{in}$ = 2.8 MJ/kg.

Reactor performance is optimized for a given aspect ratio when splitting the heat between the catalyst interface and unit cell periphery as described above. Furthermore, in this configuration, performance improves with increasing *AR*. The primary reasons for this are: 1) the interface heater supplies sufficient heat to vaporize the liquid feed, 2) the heat transfer along the periphery is delivered directly at the point of consumption by the steam reforming reaction, 3) as the aspect ratio increases, the radial heat transfer resistance decreases, so radial temperature gradients are minimized and 4) the Peclet number increases with increase in aspect ratio, approaching plug flow and reducing the effect of back diffusion of reactants. A plot of average temperature and difference between maximum catalyst interface and outlet temperatures supports the conclusion that splitting the heat load between the catalyst interface and unit cell boundary provides optimal performance for higher aspect ratios. When considering these results it is important to realize the increased system complexity in employing heaters within the catalyst bed that uniformly heat each unit cell periphery, in addition to controlling two

independent heaters. In this case, each unit cell is actually a miniature reactor, and the overall reactor is just a collection of these miniature reactors. However, if the catalyst were only heated at the interface, the unit cell view point is merely conceptual and the design is greatly simplified. For this reason, the remainder of this work focuses on the simplest case where heat is only supplied at the catalyst interface.

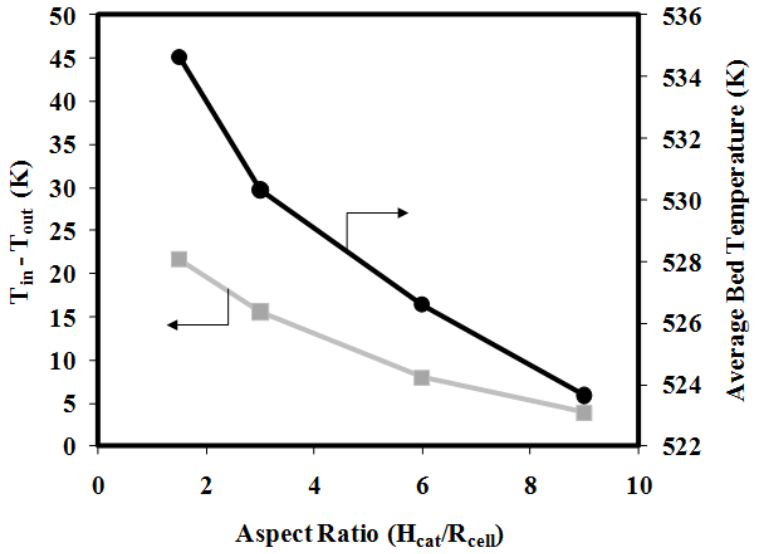

Figure 5.9. Difference between maximum interface and outlet temperature and average bed temperature for different bed aspect ratios with applied heat split between interface and unit cell periphery.

In all cases presented above, the applied heat fluxes are spatially uniform. It is also possible to generate a non-uniform heat flux distribution to improve performance for the high aspect ratio case. One possibility is mentioned in section 2.2, where alternating unit cells carry out a strong exothermic reaction, such as catalytic combustion, supplying heat to adjacent unit cells carrying out steam reforming. For both reactions, the reaction rate is highest near the impingement point so that spatially, the location of highest heat generation for the combustion reaction corresponds to the location of highest heat consumption for the steam reforming reaction. To achieve this, proper catalyst loadings

and feed rates must be selected to match the heat loads in adjacent channels. A thorough analysis of this has already been performed by Stefanidis and Vlachos [50] and is not pursued any further here.

5.2.3 Effect of Droplet Delivery Rate

To achieve a target fuel throughput, the number of unit cells is selected such that the sum of the individual unit cell throughputs adds up to the desired overall throughput. A critical design question is whether it is better to have a large number of droplet generators, each with a low throughput or a small number of droplet generators, each with a high throughput. As a first step in addressing this question, unit cells with 5, 10, and 20 μm diameter droplets delivered at a frequency of 100 kHz are investigated. The initial droplet velocity is set so that the droplet Reynolds number, $\mathrm{Re}_d = R_{d,0} V_{d,0} / \nu_g = 3.3$ (as in the baseline simulations) to ensure that the droplet stream impinges on the catalyst interface without significant evaporation. In each case, the catalyst bed is heated at the interface with $Q_{in} / \dot{m}_{in}$ = 2.8 MJ/kg and W/F = 72 kgcat-s/gmol, just as with the baseline case. In investigating the effect of *AR* above, it is observed that the interplay between diffusive and advective transport and bed thermal resistance are the critical factors in determining reactor performance. For this reason, the results here are presented as a function of Pe rather than *AR*. For each throughput a range of *AR* are investigated to roughly cover the range 1 < Pe < 10, and the relevant results are presented in Figure 5.10. As expected, the maximum interface temperature increases while the average outlet temperature decreases with increasing Pe because of the increasing axial thermal resistance, as observed in Figure 5.10 (c). However, for a given Pe, the maximum interface temperature is significantly less for lower throughput since the radial extent of

the unit cell is smaller, and the radial thermal resistance is smaller. On the other hand, the variation in outlet temperature with throughput at a given Pe is not nearly as large, and thus the spatial temperature variation throughout the catalyst bed at a given Pe is reduced as the unit cell throughput is reduced.

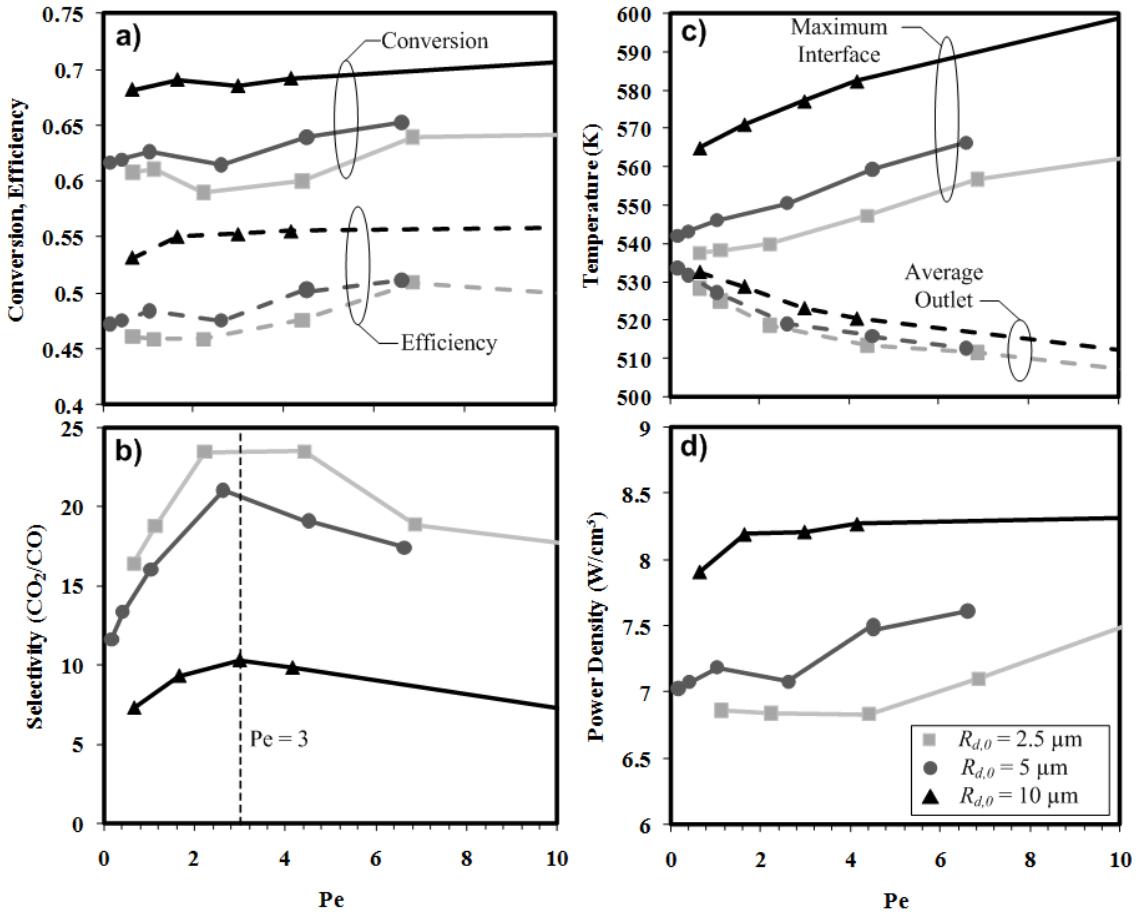

Figure 5.10. DDIR performance as a function of Pe for unit cell throughputs defined by droplets with $R_{d,0}$ = 2.5, 5, and 10 µm delivered at a frequency of 100 kHz. For all cases, W/F = 72 kgcat-s/gmol and $Q_{in} / \dot{m}_{in}$ = 2.8 MJ/kg. a) methanol conversion and efficiency, b) selectivity to methanol steam reforming, c) maximum interface temperature and average outlet temperature, and d) power density.

Although the catalyst bed approaches isothermality for lower unit cell throughput and lower Pe, Figure 5.10 (a) and (d) show that the methanol conversion, efficiency, and power density are in fact higher for higher unit cell throughput because of the hotspot at

the catalyst interface combined with the exponential dependence of reaction rate on temperature (this was discussed in the previous section)

Again, the most interesting result is the variation of selectivity with Pe for varying throughput shown in Figure 5.10 (b). All the curves display a maximum in selectivity with Pe, the reasons for which are explained in the previous section. What is remarkable is that the maximum in selectivity occurs at Pe ~ 3 regardless of unit cell throughput. This validates selecting Pe as the dimensionless parameter controlling reactor performance, capturing the influence of both back diffusion of products and catalyst bed thermal resistance.

All previous results are for W/F = 72 kgcat-s/gmol and $Q_{in} / \dot{m}_{in}$ = 2.8 MJ/kg, which is based on the isothermal plug flow reactor results at 523 K. However, the non ideal conditions in the DDIR result in low methanol conversion (~ 60-70%), which would be considered unacceptable for an actual fuel reformer, since a large part of the fuel would be unutilized. Achieving an acceptable minimum conversion of 95% requires increasing W/F or $Q_{in} / \dot{m}_{in}$, or some combination thereof.

First, consider keeping $Q_{in} / \dot{m}_{in}$ constant at 2.8 MJ/kg and increasing W/F to try to achieve the target conversion for each of the unit cell throughputs presented above with Pe = 3. The results of these simulations are shown in Figure 5.11. As catalyst is added (W/F increased), the conversion increases as expected, but begins to level off before it reaches 80% for the highest throughput case. This occurs because the bed thermal resistance increases with size, which causes both peak and average catalyst temperatures to decrease to the point where conversion actually begins to decrease as more catalyst is added. For the lower unit cell throughput cases, the conversion does not

level off, but only marginal increase in conversion is observed for over a factor of 4 increase in W/F. Thus, the approach of simply increasing the catalyst bed size with a fixed heat input at the catalyst interface is not a practical solution for achieving the target 95% conversion. However, this may be a viable solution for the split heater deployment described above since the applied heat is better spatially matched to the point of consumption.

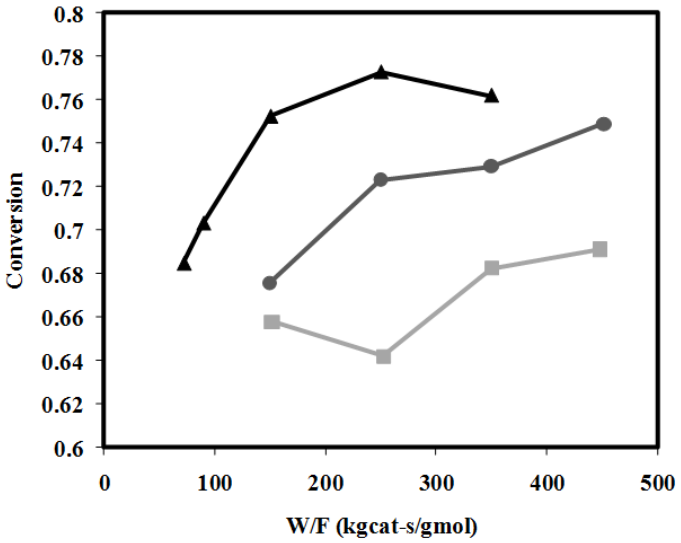

Figure 5.11. Effect of increasing W/F on methanol conversion for the cases, $R_{d,0}$ = 10 µm, 5 µm, 2.5 µm, each with Pe = 3, f = 100 KHz, $Q_{in} / \dot{m}_{in}$ = 2.8 MJ/kg.

Instead, consider retaining W/F = 72 kgcat-s/gmol as in the above cases and increasing $Q_{in} / \dot{m}_{in}$ to 3.4 MJ/kg to achieve the desired 95 % conversion level. This is shown in Figure 5.12 as a function of Pe for unit cell throughputs defined by 5, 10, and 20 µm diameter droplets delivered at a frequency of 100 kHz. Clearly, the target conversion is achievable simply by increasing the interface heat flux, and accompanying increases in power density and efficiency are also observed. Furthermore, the difference in performance for different unit cell throughputs is less pronounced. However, the tradeoff is a decrease in selectivity. In fact, Figure 5.12 (b) not only shows that selectivity

drops dramatically compared to the results for $Q_{in} / \dot{m}_{in}$ = 2.8 MJ/kg shown in Figure 5.10, but there is no clear maximum in selectivity with Pe. Figure 5.12 (c) reveals an expected increase in both interface and outlet temperature compared to the case with lower heat input. Because the decomposition rate increases faster with temperature than the steam reforming rate, the behavior of the selectivity at elevated temperatures is dominated by this, reducing the influence of back diffusion and bed thermal resistance that results in a clear maximum in selectivity with Pe at lower $Q_{in} / \dot{m}_{in}$. In fact, observing Figure 5.10 (b) for the highest throughput case ($R_{d,0}$ = 10 μm, f = 100 KHz) hints at this transition in behavior as the selectivity curve begins to flatten with an increase in temperature.

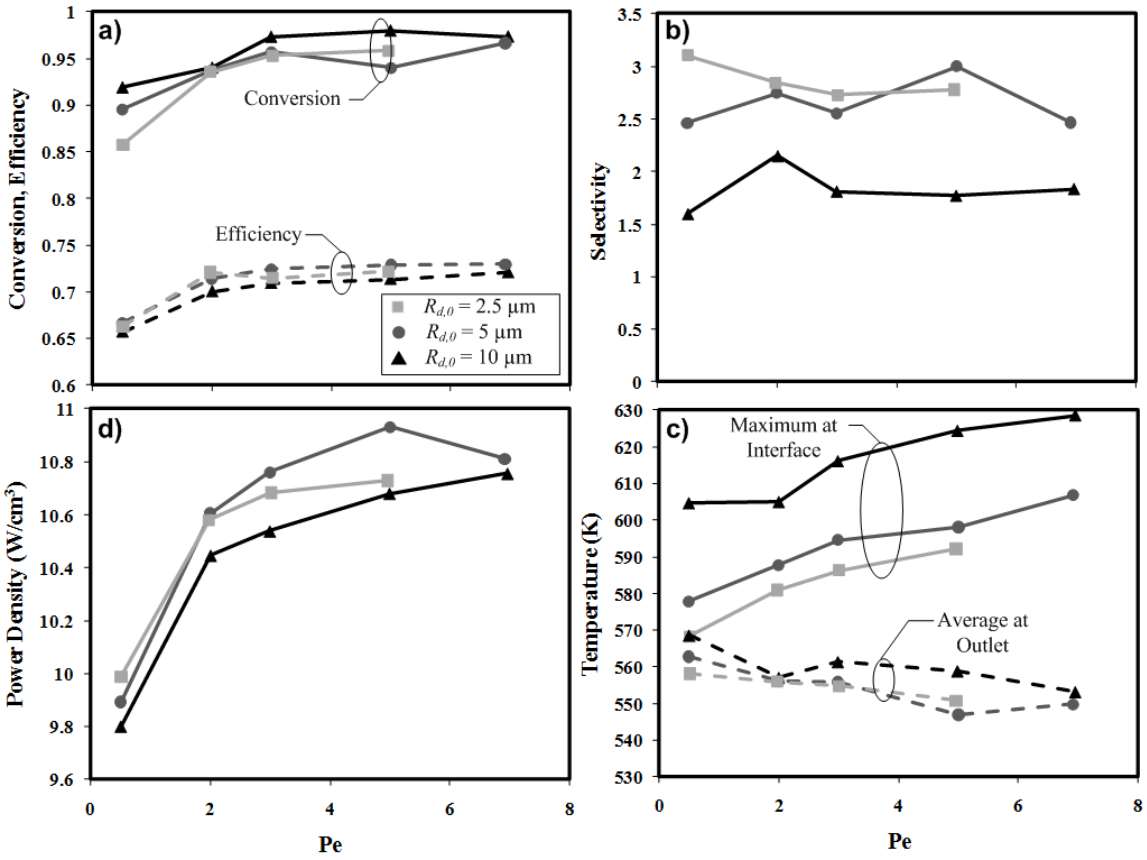

Figure 5.12. DDIR performance as a function of Pe for unit cell throughputs defined by droplets with $R_{d,0}$ = 2.5, 5, and 10 µm delivered at a frequency of 100 kHz. For all cases, W/F = 72 kgcat-s/gmol and $Q_{in} / \dot{m}_{in}$ = 3.4 MJ/kg. a) methanol conversion and efficiency, b) selectivity to methanol steam reforming, c) maximum interface temperature and average outlet temperature, and d) power density.

As mentioned previously, changing both W/F and $Q_{in} / \dot{m}_{in}$ instead of just one or the other, is a viable option for achieving a conversion goal. Having control over both of these opens up the parameter space considerably and allows the reactor performance metrics to be tuned over a much broader range. To fully explore this possibility, several simulations must be run over reasonable ranges of W/F and $Q_{in} / \dot{m}_{in}$ for different throughputs and unit cell aspect ratios (Pe). This requires a considerable investment in computational time and is not investigated further here. However, the general trends in behavior observed for the cases presented above provide valuable insight into the design

of the DDIR reactor for methanol steam reforming without the need for an exhaustive parametric study.

Again, one must factor in the practical consideration of maximum catalyst operating temperature. In each case presented above, the maximum temperature at the catalyst interface is always lowest for the lowest unit cell throughput. This suggests that to eliminate hotspots and promote bed isothermality, achieving a given total throughput should be accomplished by adding together unit cells with the lowest throughput that is practically achievable. In the next section, it is observed that certain conditions must be met in order for the droplet stream to impinge on the catalyst and have the reactor operate as anticipated. This leads to more stringent conditions as the unit cell throughput is decreased.

5.2.4 Effect of Droplet Parameters at a Given Throughput

Achieving a given unit cell throughput could be accomplished by delivering small droplets at a high frequency or larger droplets at a lower frequency. It is desired to determine whether this has an effect on the reactor behavior. Specifically, the droplet stream can impinge on the catalyst interface, be overcome by viscous drag and not reach the catalyst layer, or completely evaporate before reaching the catalyst interface. This is investigated by considering a fixed unit cell throughput of 4.4×10^{-8} kg/s achieved with droplet sizes of 5, 10, and 20 μm and frequencies of 800, 100, and 12.5 kHz, respectively with $V_{d,0}$ = 5 m/s and $T_{d,0}$ = 300 K for all cases. For each droplet diameter the distance between the atomizer and catalyst, H_{cell}, is increased until the droplet does not impinge on the catalyst interface or completely evaporates. For the purposes of this analysis, the droplet stream is defined as "stopped" when the droplet velocity decreases to $0.001 V_{d,0}$,

meaning the droplet stream is overcome by drag forces before reaching the catalyst interface. The other simulation parameters are fixed at $Q_{in} / \dot{m}_{in}$ = 2.8 MJ/kg, W/F = 72 kgcat-s/gmol, and AR = 1.5.

For a single droplet traveling through a quiescent medium it is a simple matter to calculate whether the droplet impinges on the surface, completely evaporates, or is overcome by drag forces and never reaches the catalyst surface. This is done by solving the trajectory of the droplet using eqs. (3.1)-5). First, consider the case of negligible droplet heating and evaporation. Here, an analytical expression for $V_d(t)$ is found by integrating eq. (3.2) to find the time required for $V_d = 0.001 V_{d,0}$. The maximum distance traveled by the droplet, d_{max}, is then found by integrating eq. (3.1) over this time using the analytical expression for $V_d(t)$, yielding

$$d_{\max} = \frac{2}{9} \frac{R_{d,0}^2 V_{d,0} \rho_l}{\mu_g} \tag{5.8}$$

To cast this in dimensionless form, the following time scales are defined:

- Droplet transit, $\tau_{d,trans} = H_{cell} / V_{d,0}$, defined as the time required for the droplet to travel to the catalyst interface.
- Droplet drag, $\tau_{d,drag} = \left(\rho_l / \rho_g\right)\left(R_{d,0}^2 / \nu_g\right)$, defined as the ratio of the initial droplet momentum to the drag force on the droplet (assuming Stokes flow).

Using these timescales, the following criterion defines the transition between impingement and no impingement of a single droplet traveling through a quiescent medium.

$$\frac{\tau_{d,drag}}{\tau_{d,trans}} \sim \frac{9}{2} \tag{5.9}$$

In the case of the DDIR, however, the continuous stream of droplets creates an entrained flow with a recirculation zone as shown above for the baseline case. This coupling between the droplet transport and the surrounding gas phase has a significant impact on what the ultimate fate of the droplet stream is. Examining eq. (3.2) shows that the drag force is proportional to ($V_d - u$), where u is the gas phase velocity. Clearly, the higher the surrounding gas velocity induced by the entrained flow, the lower the drag force will be, and in general terms the easier it is for the droplet stream to impinge on the catalyst interface. To determine this effect, a modified timescale for droplet drag, $\tau^*_{d,drag}$, is introduced that accounts for the gas phase velocity. This timescale is found by scaling eq. (3.2) as follows

$$\frac{V_{d,0}}{\tau^*_{d,drag}} = \frac{\rho_g}{\rho_l}\frac{\nu_g\left(V_{d,0}-u_s\right)}{R^2_{d,0}} \Rightarrow \tau^*_{d,drag} = \frac{\rho_l}{\rho_g}\frac{R^2_{d,0}}{\nu_g}\frac{V_{d,0}}{\left(V_{d,0}-u_s\right)} \tag{5.10}$$

An appropriate scale for the gas phase velocity follows from the gas phase momentum equation, eq. (3.50), by assuming that the viscous term in the radial direction scales with the source term from the droplet and the radial length scales with droplet radius.

$$\frac{\nu_g u_s}{R^2_{d,0}} \sim \frac{6\pi\nu_g R_{d,0}\left(V_{d,0}-u_s\right) f}{V_{d,0}}\frac{\delta(r)}{2\pi r} \tag{5.11}$$

The only difficulty is in dealing with the delta function in the source term. Realizing that this concentrates the source at the axis, and instead spreading the source out so that it occupies the droplet radius leads to

$$\frac{\nu_g u_s}{R_{d,0}^2} \sim \frac{6\pi\nu_g R_{d,0}\left(V_{d,0}-u_s\right)f}{V_{d,0}\pi R_{d,0}^2} \tag{5.12}$$

Solving for the velocity scale, u_s, yields.

$$u_s \sim \frac{6R_{d,0}f}{1+\frac{6R_{d,0}f}{V_{d,0}}} \tag{5.13}$$

Assuming that the criterion for transition between impingement and no impingement, $\tau_{d,drag}^{*}/\tau_{trans} > 9/2$, still holds with the modified timescale for drag, and inserting the expression for the velocity scale from eq. (5.13) yields a new expression for the transition criterion as a function of droplet delivery frequency.

$$\frac{\tau_{d,drag}^{*}}{\tau_{d,trans}} \sim \frac{\rho_l}{\rho_g}\frac{R_{d,0}^2}{\nu_g}\frac{V_{d,0}}{H_{cell}}\left[1+\frac{6R_{d,0}f}{V_{d,0}}\right] \sim \frac{9}{2} \tag{5.14}$$

Defining the ratio of timescales $Re_{mod} = \tau_{d,drag}/\tau_{trans}$, which is like a modified Reynolds number and recognizing the Strouhal number, $St = R_{d,0}f/V_{d,0}$, the transition between impingement and no impingement is recast in terms of these dimensionless numbers.

$$Re_{mod} \sim \frac{9}{2}\frac{1}{1+6St} \tag{5.15}$$

Plotting this transition line as shown does not divide the simulation results between the impingement and no impingement well. Reconsidering the droplet velocity scale used in the above scale analysis leads to the proper form of the transition line. Since at transition, the velocity varies between $V_{d,0}$ and $0.001V_{d,0}$, the proper scaling to use is a time (or position) averaged velocity, which turns out to be $0.22V_{d,0}$. Plotting the transition line with this revised velocity scale is a much better fit to the simulation data, and is shown in

Figure 5.13. Physically, the scaling makes sense since as $St \to 0$, $Re_{mod} \to 9/2$, and as $St \to \infty$, $Re_{mod} \to 0$. However, it should be realized that there is a maximum St for which the transition scaling is valid, which corresponds to the transition between a stream of droplets and a jet (when the droplets touch each other the distance between them is $2R_{d,0}$). This corresponds to $St > 0.5$, which is shown on Figure 5.13, demonstrating that the derived scaling law applies to all of the simulated cases.

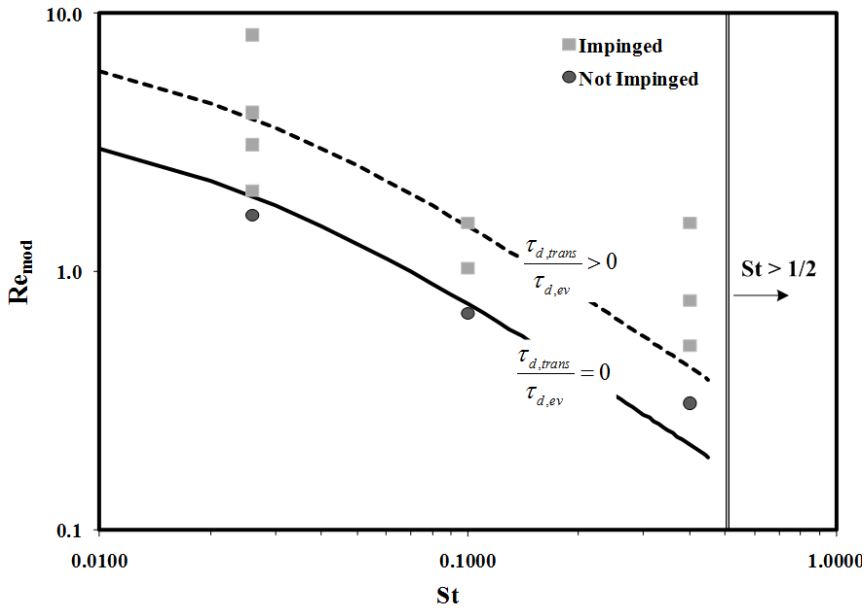

Figure 5.13. Regime map showing transition between droplet impingement and no impingement. The minimum Re_{mod} for impingement decreases as St increases. The transition line shifts up if significant droplet evaporation is occurring.

At the highest value of St, however, the no impingement result lies above the transition line. This occurs because the droplet stream experiences significant evaporation as shown in Figure 5.14. Thus, the transition line will shift upwards for increasing values of $\tau_{d,trans}/\tau_{d,ev}$ because as the droplet radius continuously decreases as evaporation occurs, the surface area to volume ratio increases and the drag forces become dominant. Here, the timescale for droplet evaporation is defined as $\tau_{d,ev} = R_{d,0}^2/K$.

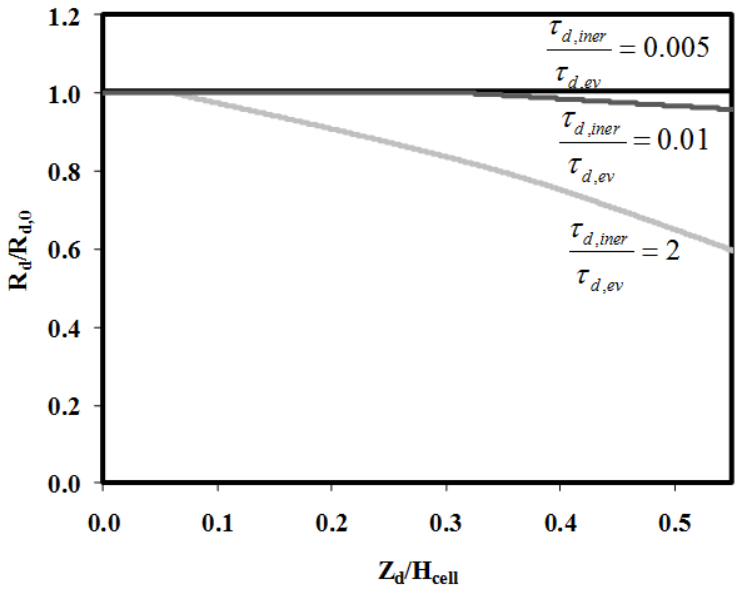

Figure 5.14. Normalized droplet area vs. normalized position for different values of the droplet evaporation timescale.

In general, complete evaporation of the droplet stream is possible before it is arrested if the value of $\tau_{d,trans}/\tau_{d,ev}$ is sufficiently high, but this does not occur for any of the cases in the methanol steam reforming reaction considered here. In the case of steam reforming the composition of the surrounding gas tends to that of the incoming droplet stream so that the potential for mass transfer is low and the reaction temperature is relatively moderate so that heat transfer to the droplets is low. In the case of autothermal reforming, full evaporation may be possible because the surrounding air flow will increase the potential for mass transfer from the droplet. If complete evaporation of the droplet stream occurs, then the complexity of the regime map increases and another family of transition lines must be added to account for this.

Consider the implications of these results on the conclusion reached in the previous section that the unit cell throughput should be made as small as possible to more effectively utilize the heat supplied at the interface. For smaller throughput (at a constant

$V_{d,0}$), St decreases, so Re_{mod} must be higher to achieve impingement. Furthermore, smaller unit cell throughput requires smaller droplets at a higher frequency in order to retain the validity of the steady state assumption. Thus, the evaporation timescale will decrease and the transition curve shifts to even higher Re_{mod}. Achieving impingement then largely depends on the maximum droplet velocity attainable by the droplet generator and the minimum allowable proximity between the droplet generator and the catalyst interface (which is addressed further below in the practical considerations section).

5.2.5 Effect of Heat Losses

Heat losses to the surroundings will have a significant impact on reactor performance. Consider the effect of heat losses from a single isolated unit cell with Pe = 3, W/F = 72 kgcat-s/gmol, $Q_{in} / \dot{m}_{in}$ = 2.8 MJ/kg, and a throughput of 3.5 x10^{-7} kg/s. Figure 5.15 shows that even at values of heat transfer coefficient below typical natural convection conditions (~ 10 W/m^2-K) the unit cell reactor performance suffers greatly.

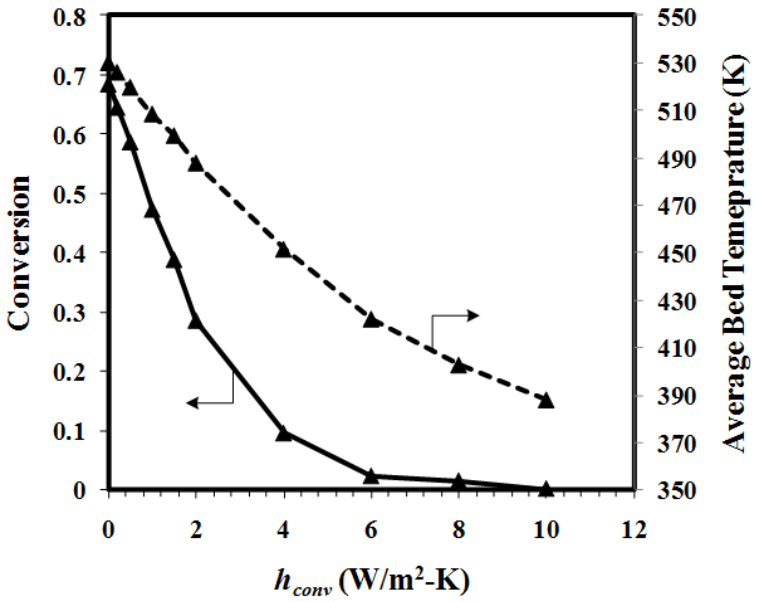

Figure 5.15. Effect of heat transfer coefficient on conversion and average catalyst bed temperature for a single unit cell with Pe = 3, W/F = 72 kgcat-s/gmol, $Q_{in} / \dot{m}_{in}$ = 2.8 MJ/kg, and a throughput of 3.5 x10^{-7} kg/s.

However, in a real DDIR, there are a collection of unit cells and in this situation, only the unit cells on the edge lose heat to the environment, which will result in decreased performance. The heat loss at the edges will also produce a temperature gradient over the entire DDIR so that each interior unit cell experiences different conditions, which is depicted schematically in Figure 5.16 (a). It is desired to account for these heat losses to the surroundings in such a manner that each unit cell experiences identical conditions, so that the basic design principle of adding unit cells together to achieve a given total throughput is unchanged. To accomplish this goal, the total heat loss from the periphery of the entire reactor must be uniformly distributed over all of the unit cells as shown in Figure 5.16 (b). Here, the unit cells have a square cross section instead of the circular cross-section assumed in the theoretical model. In other words, each circular unit cell is approximated by a square unit cell with an equivalent cross-sectional area.

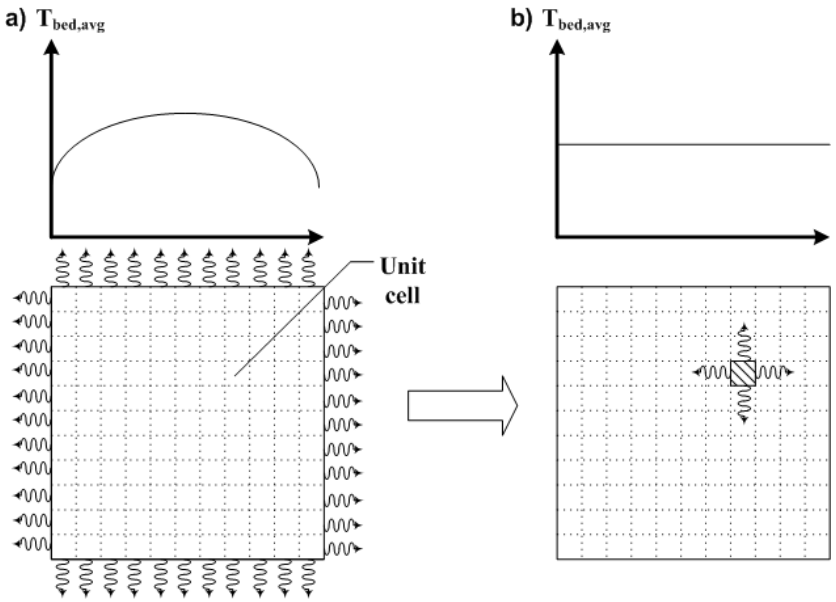

Figure 5.16. a) Schematic of heat losses from unit cells along edge of DDIR and profile of average unit cell temperature. b) Equally distributing the total heat loss from the overall DDIR among all the unit cells results in identical conditions in each unit cell.

Both the total number of unit cells (which depends on total desired throughput) and the configuration of the unit cells play an important role in reactor performance. For example, arranging all unit cells in a straight line will obviously result in the highest heat loss while arranging the unit cells in a square pattern will minimize the surface area to volume ratio and thus minimize the heat loss. The total heat loss from the DDIR, Q_{tot}, can be calculated from the heat loss from an isolated unit cell, Q_{cell}, with a uniform heat transfer coefficient at its edge (depicted in Figure 5.15) as follows.

$$Q_{tot} = Q_{cell} \frac{A_{cell,edge}}{A_{cell,tot}} N_{edge} \tag{5.16}$$

Where $A_{cell,edge}/A_{cell,tot}$ is the ratio of the exposed surface area of all of the edge unit cells to the total surface area of the edge unit cells (factoring out the unit cell boundaries on the interior of the reactor), and N_{edge} is the number of unit cells on the periphery of the overall DDIR. For a given configuration and size, this total heat loss is distributed evenly

among all unit cells, .

$$Q_{cell,eq} = \frac{Q_{tot}}{N_{tot}} = Q_{cell} \frac{A_{cell,edge}}{A_{cell,tot}} \frac{N_{edge}}{N_{tot}} \tag{5.17}$$

Thus, the overall reactor performance is estimated by applying the equivalent unit cell heat loss, $Q_{cell,eq}$. Plotting any desired integral reactor performance metric against the fraction $Q_{cell,eq}/Q_{cell}$, allows the reactor performance to be estimated for a given overall configuration since the quantity $(A_{cell,edge}/A_{cell,tot})(N_{edge}/N_{tot})$ is easily calculated. For the optimal configuration of arranging the unit cells in a square (or as close to a square as possible), the following simplification is made.

$$\frac{A_{cell,edge}}{A_{cell,tot}} \frac{N_{edge}}{N_{tot}} = \frac{1}{\sqrt{N_{tot}}} \tag{5.18}$$

These plots are shown below in Figure 5.17 for a unit cell throughput of 3.5×10^{-7} with W/F = 72 kgcat-s/gmol, $Q_{in} / \dot{m}_{in}$ = 2.8 MJ/kg, Pe = 3, and a value of the overall heat transfer coefficient of h = 10 W/m^2-K, which is typical for natural convection. Figure 5.17 confirms that reactor layout plays a critical role in performance and it is desired to minimize the number of cells on the edge. Even in the optimal configuration, if only a small total number of unit cells are required to achieve a target overall throughput, the reactor performance may be far from optimal. One strategy for countering heat losses is to simply add insulation at the boundaries to decrease the effective heat transfer coefficient. The configuration of heating the unit cell at the periphery can be modified so that only the periphery of the overall reactor is heated, which is less complicated. In fact this is exactly the configuration employed for the 100 W demonstration DDIR discussed in section 4.3 and it proved to be an adequate configuration.

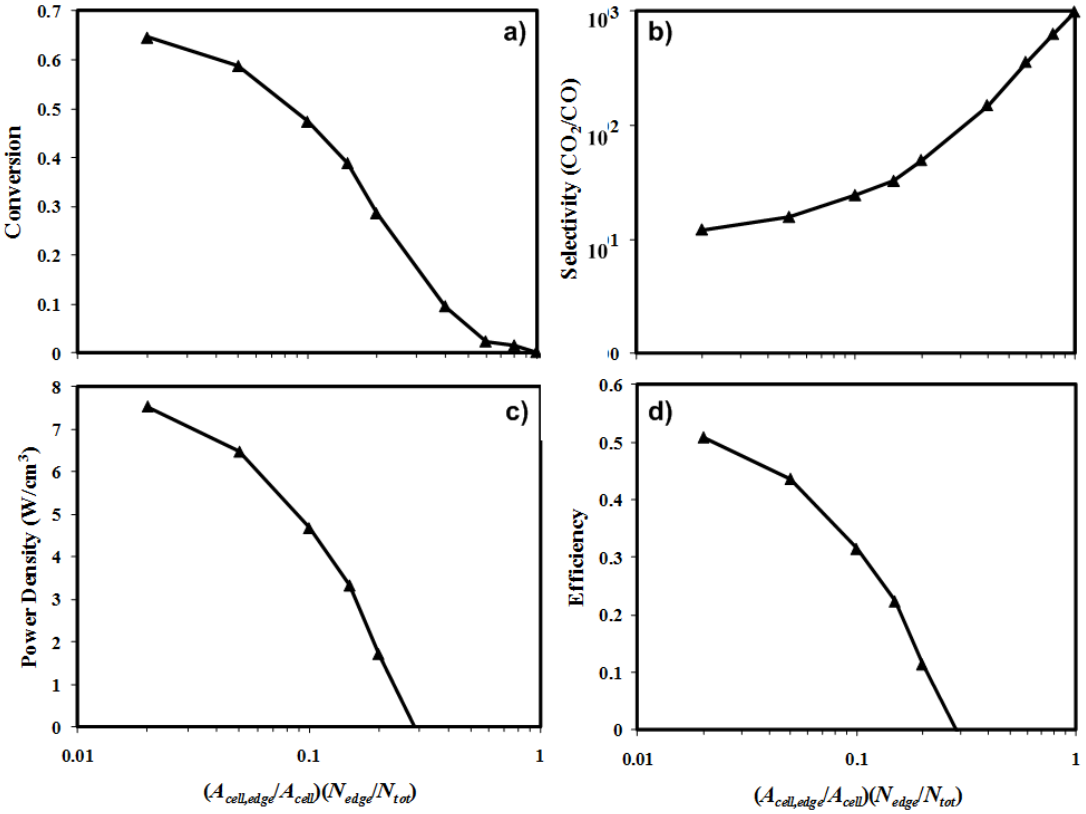

Figure 5.17. Influence of heat losses on reactor integral performance metrics with a heat transfer coefficient, h = 10 W/m^2-K. The results are plotted against the parameter $(A_{cell,edge}/A_{cell})(N_{edge}/N_{tot})$ which accounts for the layout of the unit cells. a) conversion, b) selectivity, c) power density, and d) efficiency.

5.2.6 Practical Considerations

One problem that is consistently observed in the experiments is condensation of liquid feed as some of the vapor generated at the catalyst interface comes into contact with the cold side walls or atomizer surface. The flow of the vaporized liquid feed back toward the atomizer and the high concentration of gaseous methanol and water coupled with surfaces exposed to cold external conditions explains these observations. Thus, unit cells at or near the boundary are particularly subject to condensation. To counter this, the reactor should be properly insulated such that all surfaces remain above the saturation temperature of the liquid mixture.

Another problem can arise when the temperature at the atomizer surface is maintained above the saturation temperature of the liquid. If the atomizer surface is in intimate thermal contact with the reservoir from which it is supplied, the liquid can boil and interfere with proper atomization of the liquid. This is true for the specific case of the ultrasonic atomizer studied in this work, and care must be taken to sufficiently insulate the liquid reservoir to avoid boiling at elevated temperatures. As a result, there is a practical minimum distance between the atomizer surface and hot catalyst interface, which factors into whether the droplet stream impinges or is deflected from the catalyst interface.

CHAPTER 6

CONCLUSIONS AND RECOMMENDATIONS FOR FUTURE WORK

This thesis work has led to a number of fundamental insights and important recommendations about the design and operation of DDIRs for methanol steam reforming. The original contributions to the field of portable fuel reforming and catalytic microreactor design are summarized below along with a summary of the important conclusions from the theoretical and experimental studies and suggestions for future studies on direct droplet impingement type reactors.

6.1 Original Contributions

- Development of the DDIR concept using a layered design of a regularly spaced array of droplet generators and a heated catalyst layer offers a scalable reactor platform utilizing the concept of multifunctional reactors in which 1) the droplet generator acts as both a liquid feed pump and fuel atomizer, and 2) the heated catalyst layer acts as both the liquid vaporizer and reaction chamber. Further, conceptualizing the DDIR as a collection of unit cells allows a careful theoretical and experimental investigation of the DDIR operation and development of first-principles guidelines for the reactor scale-up to various throughputs.
- A physics-based comprehensive model of the DDIR unit cell is developed with minimal empiricism, which considers the coupled processes of 1) droplet transport, evaporation, and impingement on the catalyst interface 2) liquid film accumulation at

the catalyst interface with capillary penetration and vaporization, and 3) heat and mass transport in the gas phase with catalytic reaction. This provides a comprehensive framework to investigate the influence of operating parameters on reactor performance. The model was applied to an in-depth investigation of methanol steam reforming, but the simulation tools developed are general enough to extend to other reactant/catalyst systems where a liquid feed must be vaporized before conversion via heterogeneous catalysis.

- Both methanol steam reforming and sustained methanol autothermal reforming are successfully experimentally demonstrated using the DDIR over a range of operating conditions.
- An experimental apparatus emulating a unit cell of the DDIR reactor is constructed to allow careful visual examination of the droplet impingement and film growth processes at the porous catalyst interface while simultaneously monitoring reaction products. Different droplet impact conditions and film accumulation regimes are observed, and are found to be in good agreement with model predictions. These coupled transport-reaction measurements are important in their own right, as well as for validating the comprehensive DDIR model.
- Analytical criteria are developed for droplet impingement on the heated catalyst layer in terms of relevant dimensionless numbers, using the reduced order droplet transit model and time scale analysis. The criteria are validated through simulations showing transition to impingement of the droplet stream. Furthermore, the developed criteria agree with experimental data showing deflection of the droplet stream from the catalyst interface.

6.2 Conclusions

Several conclusions can be drawn relative to the design of a DDIR reactor for methanol steam reforming based on the combined experimental observations and simulation results. The overall reactor performance depends on the complex interplay of all transport processes occurring in the reactor.

- Selectivity to steam reforming displays a clear maximum at Pe ~ 3, independent of the droplet delivery rate, resulting from a transition between back diffusion dominated behavior at low Pe to bed thermal resistance dominated behavior at high Pe. However, as reactor temperature increases, the selectivity decreases as expected and the variation with Pe diminishes.
- For a given droplet delivery rate, a minimum Reynolds number is required to ensure impingement on the catalyst interface, which is a decreasing function of droplet Strouhal number. This minimum Reynolds number increases with increasing droplet evaporation rate. However, the Reynolds number should also be such that Weber number is less than 80 at impingement to prevent splashing at the interface and subsequent unpredictable behavior. Beyond a Strouhal number of ½, the droplet stream collapses into a continuous jet which impinges at the catalyst surface.
- Complete evaporation of the droplet stream before impingement is not observed either experimentally or in simulations due to the mild conditions of the steam reforming reaction. Depending on operating conditions, film operation could be preferred from the conversion/selectivity prospective, so flash evaporation is not necessarily an optimal mode for DDIR operation, especially for reactions requiring moderate temperature.

- The spatial deployment of heaters in the reactor and unit cell aspect ratio (defined as the ratio of lateral extent to length) both have a significant impact on reactor performance.
    - Employing heaters only at the interface favors lower aspect ratios because the axial thermal resistance is less and leads to less spatial variation in bed temperature.
    - Employing heaters only along the side walls of the unit cell also favors lower aspect ratios because more heat is concentrated near the interface where it is required to drive vaporization and endothermic reaction. For this reason, flooding occurs above a certain aspect ratio, which depends on the total heat input to the reactor.
    - Splitting the heat load between an interface heater and side wall heater such that the interface heater matches the thermal load required to vaporize and heat the feed while the side wall heater matches the thermal load of the endothermic reaction always leads to the most favorable operation. Furthermore, the performance improvement is more pronounced for higher aspect ratio.
- Experimental results for methanol steam reforming with the demonstrated DDIR show comparable results with those presented in the literature for portable reformers. Furthermore, sustained autothermal operation was demonstrated, opening the door for future research for this reaction, which is discussed further below.

6.2.1 Summary in the Context of Existing Portable Reformer Technology

The key differences in the liquid fuel delivery method and reagent/catalyst

interaction in the DDIR lead to some distinct advantages over portable microchannel reformers presented in the literature. First, the droplet generator is an intimately integrated multifunctional component, achieving precise control over the droplet characteristics while simultaneously serving as the liquid feed pump. On the other hand, integrated fuel delivery methods have largely gone unaddressed for most microchannel fuel reformers. Furthermore, since the droplet generator is able to maintain precise control at low flow rates, this device is suitable for low-power applications (< 100 W). Also, variations in hydrogen demand from the fuel cell can be met by changing the rate of droplet delivery. For the specific case of the ultrasonic atomizer presented in this work, this is easily achieved by operating the device in a pulsed mode with variable duty cycle. Maintaining flow rate control at low flow rates is more difficult in microchannel reactor designs due to formation of stabilized vapor slugs and flow rate variations as described in Chapter 2. The multifunctional vaporization/catalysis method employed in the DDIR avoids these problems and has proven viable to achieve phase change and reaction with the heated catalyst bed, as confirmed by both experiments and modeling. Additionally, the DDIR provides a simpler design since the standalone vaporizer component is eliminated.

Another significant difference between microchannel based fuel reformers and the DDIR design is the resulting form factor. For microchannel designs, typically, the reactor is operated at high Pe to approach plug flow, using long channels with low hydraulic diameter etched into a planar substrate. Increase in throughput is achieved by increasing channel length or adding more channels in parallel. Stacked arrangements are utilized instead of arranging the channel(s) on a single layer to achieve a given form factor [21].

For the simplest embodiment of the DDIR with only the interface heater deployed, the form factor is set by the overall throughput and the unit cell aspect ratio for which the selectivity is maximum (Pe ~ 3). It was shown that much more flexibility in reactor form factor is achieved by employing more complex heater configurations (i.e. deploying heaters at the unit cell periphery within the catalyst bed).

The experimental results for the microchannel fuel reformers from the literature initially presented in Chapter 4 are revisited and compared against DDIR simulations under similar ranges of catalyst loading and thermal conditions. This provides some insight into how well the DDIR design would compare to the microchannel reformers if the problems encountered during the experiments were eliminated. These results are shown below for DDIR simulations run with Pe = 3, a unit cell throughput of 3.5 x10^{-7} kg/s, and $Q_{in} / \dot{m}_{in}$ varied (and applied all at the catalyst interface) to yield an average catalyst bed temperature close to 200 ^{o}C although there is some variation in temperature between the results. Figure 6.1 clearly shows the potential of the DDIR to outperform the microchannel reactors, especially at higher conversions, where up to a 40% increase in conversion is observed. Further, these microchannel reactor results do not account for penalization due to liquid feed vaporization and heating. These penalties are automatically built into the DDIR reactor. Isothermal plug flow reactor (PFR) results are also shown, providing an upper limit on reactor performance, showing that the DDIR deviates most at higher conversion due to the larger bed size and higher thermal resistance in the bed. However, the performance of the DDIR can be improved further relative to the isothermal PFR by better heat distribution as demonstrated in Chapter 5.

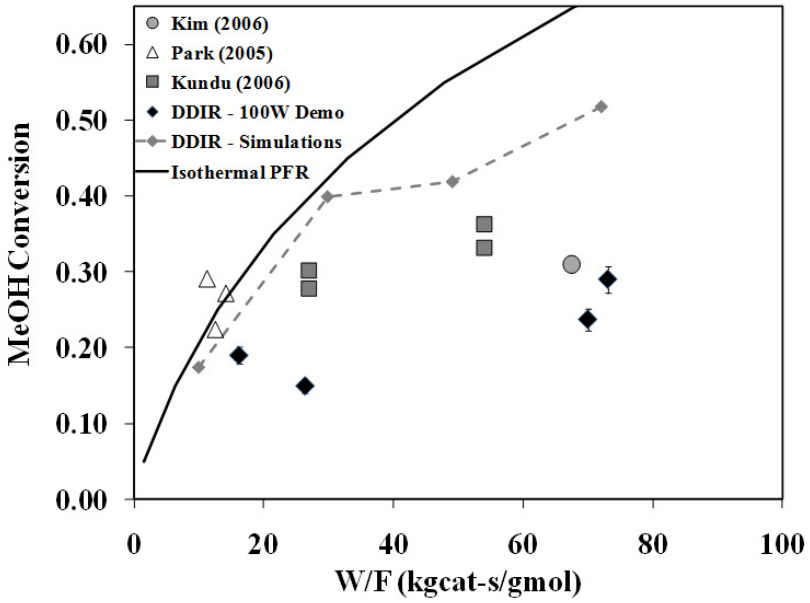

Figure 6.1. Comparison of methanol conversion in experimental microchannel reactors with DDIR simulations. The experimental results for the 100 W demonstration DDIR are also shown.

The results from the preliminary experiments and detailed modeling for methanol steam reforming presented in this work shows that the DDIR can achieve performance at least comparable to typical portable microchannel fuel reformers. Further performance improvements are possible with optimal design parameters as presented in Chapter 5. This makes the DDIR an attractive alternative design for portable fuel reforming, motivating further research into this class of reactors with several specific suggestions made below.

6.3 Suggestions for Improvements and Future Research

1) Extended Experimental Investigation of MSR. Several interesting results from the model results for methanol steam reforming should be verified experimentally. This involves development of several droplet generators with different unit cell throughputs (by varying droplet diameter and operating frequency). Further,

improving the spatial distribution of heat supply at the catalyst interface is necessary with the array of droplet generators. However, the basic infrastructure already exists for measurement and instrumentation of the experimental apparatus.

2) Reliability of Droplet Generator. Lack of stable and steady operation of the ultrasonic atomizer array used in the 100 W reactor demonstration unit was one factor in preventing optimal performance. Investigation into improving the operation of the droplet generator such that each nozzle in the array always produces a single droplet at every cycle is required. Alternative droplet generation techniques can also be explored.

3) Investigation of Transient Operation. The DDIR reactor is inherently transient since there is a finite time between successive droplet injections, but this work focused on the case where this time was sufficiently small to avoid significant transients. A first step would be to properly model the product of fluctuating terms appearing in the periodic steady-state equations to extend the range of applicability of the model.

Beyond this, examination of forced unsteady-state operation is already underway in our research group. Specifically, the modulation of feed rate, composition, and reactor temperature is being investigated to improve the time averaged performance of the reactor compared to steady-state operation. Systematic investigation of potential modulating frequencies is being performed by identifying the timescales of the transport processes occurring in the reactor. This basic approach has proved fruitful in utilizing periodic flow reversal for methane partial oxidation by matching the switching time with the time scale for thermal capacitance of the bed, resulting in measurable performance improvement [85].

4) Modeling of Autothermal Operation. Although this mode of operation was demonstrated with the bench scale DDIR reactor, it was not investigated in detail using the model developed in this work. Extension of this model to this reaction should be straightforward given appropriate kinetic data [86], which is far more sparse than that for steam reforming. What is particularly appealing about this reaction is that the heat for vaporizing and heating the liquid is produced directly at the point of contact with the catalyst without the need for external heat input, except at startup. Reactor sizing and aspect ratio take on a more important role as mixing of the vaporized feed at the interface with input air must occur while the heat produced from the exothermic reaction must be effectively spread over the catalyst bed. Autothermal reforming reactors would be particularly suited for applications requiring high power densities since none of the useful energy produced in the form of hydrogen would be wasted for heating. However, integration of a hydrogen separation membrane is crucial to obtain concentrations suitable for a fuel cell feed.
5) Integration with Variable Volume Batch Reactor. Previous work in this lab group investigated and demonstrated a fuel reforming device for hydrogen generation in which a fixed amount of fuel is converted in a batch reactor integrated with a hydrogen selective membrane, called a CHAMP reactor [87]. Integration of the DDIR type droplet delivery method in the interior of the CHAMP would eliminate the need for an external vaporizer. Also, additional modes of operation could open up with the ability to introduce more fuel mid-cycle.

Another possible configuration is a hybrid DDIR-CHAMP combination where the DDIR is operated at low W/F to achieve a high power density (but low fuel

utilization) and the CHAMP is used as a regenerative fuel processor to achieve optimal conversion and selectivity.

APPENDIX A

DETAILS OF FLUENT SIMULATIONS

A.1. Zone Definition and Boundary Conditions

The DDIR unit cell geometry is meshed in Gambit v2.2.30 as shown in Figure 3.4, in which four separate fluid zones and eight boundary zones are defined. The Fluent settings for each of these zones is described next.

Atomizer Boundary Zone

This is set as a "wall" boundary, which is impermeable to flow. The default thermal boundary condition for this zone is adiabatic.

In some of the simulations accompanying experimental results, a gas flow is introduced at this boundary, so the boundary condition is changed to a "velocity-inlet" with the appropriate velocity normal to the boundary and gas temperature supplied as inputs.

Outlet Boundary Zone

The outlet boundary zone is defined as a "pressure outlet" with the pressure and backflow temperature specified as inputs to the simulation. The default values are a gauge pressure of zero and backflow of nitrogen at a temperature of 300 K. Additionally, the option for target mass flow rate is set to the current combined value of the vaporization rate from the liquid film and droplet stream.

Film Interface Zones

All film interface zones are defined as wall boundary conditions. Because there is a fluid zone on each side of the wall, there is an additional shadow zone automatically

generated for each boundary zone once the mesh is imported into Fluent. A constant temperature equal to the saturation temperature of the liquid fuel mixture is applied to each of the film interface zones.

Gas Fluid Zone

This is the space where the droplets travel between the droplet generator and catalyst surface. In this zone, source terms are applied for mass, species, momentum, and heat arising from evaporation of droplets and from the gas side film interface. The source terms arising from droplet evaporation are applied to the computational cells adjacent to the axis boundary zone and are calculated by integrating the steady-state source terms across the length of the computational cell. For example, the source term for species *i* in computational cell *j*, $S_{i,j}$, is given by

$$S_{i,j} = \frac{1}{\forall_j} \int_{z_j - 0.5\Delta z_j}^{z_j + 0.5\Delta z_j} \frac{\dot{m}_{d,i}}{V_d} f dz \approx \frac{f}{\forall_j} \sum_{k=0}^{M} \frac{1}{2} \left[\left(\frac{\dot{m}_{d,i}}{V_d} \right)^{(k+1)} + \left(\frac{\dot{m}_{d,i}}{V_d} \right)^{(k)} \right] \left(Z_d^{(k+1)} - Z_d^{(k)} \right) \qquad \text{(A.1)}$$

where the integral has been approximated by the trapezoidal rule, Δz_j is the axial length of cell *j*, $\forall_j$ is the volume of computational cell *j*, and *k* is the index of the droplet trajectory points calculated in computational cell *j*. These source terms are implemented using separate DEFINE_SOURCE User Defined Function (UDF) coded in C++ for each source term.

Source terms from evaporation of the gas side film interface are applied to the adjacent computational cells on the gas side and are determined based on the normal component of the heat flux at the interface.

Catalyst Fluid Zone

In this zone, options are enabled for porous zone and reaction as well as source

terms for evaporation from the catalyst side film interface and interface heating. In the porous zone options, the pore level viscous and inertial resistances are calculated according to the Carman-Kozeny model [88] via DEFINE_PROFILE UDFs in which the catalyst porosity and particle diameter are inputs to the simulation. The reaction mechanism and corresponding kinetics for methanol steam reforming are taken from Peppley [39, 76]. This kinetic model is implemented in a DEFINE_VR_RATE UDF. Source terms from evaporation at the film interface are calculated and employed identically compared to those on the gas side film.

Gas and Catalyst Side Film Zones

The "Fixed Values" option is enabled in these fluid zones to set all gas phase species and velocities to zero. The liquid phase methanol and water mass fractions are set equal to those from the impinging droplets which are calculated from the droplet trajectory analysis (Ch. 3). The porous zone options are setup in the catalyst side film zone identically to those in the catalyst fluid zone.

A.2. Material Properties

Species transport is enabled and a mixture material consisting of species to be tracked is created. This mixture material consists of the species in the reaction network (gas phase methanol, water, hydrogen, carbon dioxide, carbon monoxide), and the inert species (nitrogen), along with liquid phase methanol and water, all of which are imported from the Fluent materials database. The mixture density is calculated using the "volume-weighted-mixing-law" option in Fluent. The mixture thermal conductivity and viscosity are calculated using the "mass-weighted-mixing-law" option in Fluent. The mass diffusivity is calculated using a "DEFINE_DIFFUSIVITY" UDF in which the binary

diffusion coefficient for each species in all other species is calculated using the Chapman-Enskog equation [72], averaged over the temperature range 300-600K, with extension to the multicomponent mixture:

$$D_i = \frac{1 - x_i}{\sum_{j \neq i} x_j / D_{ij}} \tag{A.2}$$

The diffusion coefficient in the liquid zones is calculated according to eq. (3.15).

The reaction network of Peppley consisting of methanol steam reforming, methanol decomposition, and water-gas shift reaction, are all defined as a reaction mechanism in the mixture material.

A.3. Droplet Transit

The droplet trajectory equations (3.1)-(3.5) are solved using a fourth order Runge-Kutta method with the time step adjustable as an input to the simulation. The surrounding gas phase fluid properties, velocity and temperature, which are required for the trajectory calculation, are taken from the Fluent cell where the droplet is located at that particular point in the trajectory. The evaporation rate at each point in the trajectory is calculated and stored along with the other droplet variables for calculation of the source terms arising from droplet evaporation. These equations are solved within a DEFINE_ADJUST UDF so that the droplet trajectory is updated after each Fluent iteration of the gas phase equations.

A.4. Solution Procedure

A Fluent Scheme program is used to control execution of the simulation, which is summarized in the flowchart of Figure 3.5. All adjustable simulation parameters, such as droplet characteristics, reactor size, boundary conditions, and solution controls can be

changed in the Scheme program. Additionally, all setup steps that would normally have to be input manually via the Fluent GUI or TUI (such as setting up material properties, defining boundary conditions, and loading/calling udfs) are accomplished automatically with the Scheme program.

Mesh Generation

An execute-on-demand UDF is developed to write a Gambit journal file containing all the commands used to generate the mesh for the current film dimensions, including export of the mesh to a Fluent case file. A separate execute-on-demand UDF calls Gambit as a background process and runs the journal file with Fluent execution paused until the mesh has been created and exported. Because Gambit has a minimum feature size, the mesh is created 1000 times larger and is scaled back down once it has been imported into Fluent.

Initialization

For the first iteration when the film size is guessed, the gas phase variables are usually initialized to spatially uniform values: $u = w = 0$, $T = 300$ K, $y_M = 0.64$, $y_W = 0.36$, and $y_i = 0$ for all other species. In some cases, when a suitable solution for a different case is available, it is mapped onto the current solution domain using a DEFINE_INIT UDF. For subsequent iterations of the film dimensions, a new mesh is created and the solution for the gas phase variables from the previous mesh is mapped onto the updated mesh to increase the rate of convergence. First, the cell positions and corresponding values for each gas phase dependent variable are obtained before the film dimensions are adjusted. The cell position values are then shifted according to how much the film interface will move upon remeshing, and these new positions and gas phase

solution are written to a file. After the new mesh has been generated, the same DEFINE_INIT UDF mentioned above is employed, which reads in the file containing the solution from the previous mesh and initializes the solution for each cell to that of the closest cell in the old mesh.

Convergence Criteria and Solution Controls

Convergence criteria for each transport equation was determined empirically by continually decreasing the convergence threshold for each variable for a test case (the baseline case presented in Chapter 5) until further reductions produced a negligible change in results. This results in the general criteria used for convergence as listed below (the numbers given are the scaled residuals in Fluent):

- Energy – $5x10^{-9}$
- Species – $1x10^{-6}$
- Velocity – $1x10^{-4}$
- Continuity – $1x10^{-3}$

In some situations, these criteria must be modified, particularly when leveling of the residual occurs before reaching the prescribed criterion. This is the case for the simulations accompanying the experimental validation.

Fluent has many options for modifying the solution method that are changed from their default values for the purposes of this simulation.

- The discretization for each equation except for pressure is set to the power law method .
- Under-relaxation factors are usually set to 1 for all variables except pressure and velocity, which are left at their default values of 0.3 and 0.7. In certain situations,

such as modeling the experimental unit cell reactor, it is required to set the under-relaxation factors to 0.99 to avoid oscillations in the residuals and promote convergence.

Grid Sensitivity

To establish a suitable grid for use in the simulations, several steps were taken. First, a test case was examined in which no film was accumulated on the liquid interface and the atomizer boundary was replaced with a velocity inlet condition to introduce the reactants consisting of a 50/50 molar mixture of methanol and steam at 523 K. All other conditions are equal to those in section 5.2.3 for the feed of 10 μm diameter droplets at 100 kHz (all heat was supplied at interface). Three different uniform grid sizes, Δz_{bulk} = 80, 40, and 20 μm were used. As shown in table A.1 below, the discretization error (calculating the methods presented in Ferziger and Peric [89]) using methanol conversion is less than 1% and the coarsest grid size is sufficient to predict the reactor behavior in the absence of the liquid film. In the second step a constant film size of $R_{film} = 6\text{x}10^{-5}$ and $h_{f,c} = 4\text{x}10^{-5}$ was used and the reactants were introduced in a spatially uniform manner over the film surface. The grid size in the bulk of the reactor was set to 80 μm and the grid size on the film was set to three different values of Δz_{film} = 12 μm, 6 μm, and 3 μm. The grid size is changed smoothly from the size at the film to the size in the bulk using the first and last ratio mesh grading scheme in Gambit. This shows that using 10 cells to resolve the effects at the film interface is sufficient, which is used as a general rule of thumb for all simulations. Finally, the full simulation is run in which the film size is iterated to find the stationary condition using the grid sizes 1) Δz_{bulk} = 20 μm, Δz_{film} = 3 μm, 2) Δz_{bulk} = 40 μm, Δz_{film} = 6 μm, and 3) Δz_{bulk} = 80 μm, Δz_{film} = 12 μm and the results

are summarized in Table A.1 below.

Table A.1. Grid sensitivity results showing change in methanol conversion (X_M) with grid refinement for two specialized cases (Cases 1 and 2) to establish appropriate grid parameters, and testing of these grid parameters for the full simulation (Case 3).

	Case 1	**Case 2**	**Case 3**
$\mathbf{r_{21}}$	2	2	2
$\mathbf{r_{32}}$	2	2	2
$\mathbf{X_{M,1}}$	0.848209	0.985033	0.994653
$\mathbf{X_{M,2}}$	0.845527	0.987758	0.995519
$\mathbf{X_{M,3}}$	0.841009	0.987953	0.99572
$\boldsymbol{\varepsilon_{32}}$	-0.00452	0.000195	0.000201
$\boldsymbol{\varepsilon_{21}}$	-0.00268	0.002725	0.000866
p - guess	2	2	2
q(p)	0	0	0
p	0.752375	3.80471	2.107172
$\mathbf{X_{M,1,ext,21}}$	0.852127	0.984823	0.994391
$\mathbf{X_{M,1,ext,32}}$	0.852127	0.987743	0.995458
$\mathbf{e_{a,21}}$	0.003162	0.002766	0.000871
$\mathbf{e_{a,32}}$	0.005343	0.000197	0.000202
$\mathbf{e_{ext\ 12}}$	0.004598	0.000213	0.000263
$\mathbf{GCI_{fine}}$	0.005774	0.000267	0.000329

Most of the simulations presented in Chapter 5 are in this general operating range, but it should be noted that these grid parameters will not produce grid independent results for all cases, but are only a guideline. A few cases were "spot checked" by decreasing the grid size and checking that the solution did not change an appreciable amount. In particular, care must be taken when applying much higher heat fluxes since the gradients in temperature and species become much greater near the interface. This is the case for many of the experimental validation simulations and the mesh had to be refined in the catalyst interface region.

REFERENCES

[1] S. F. J. Flipsen, "Power sources compared: The ultimate truth?," *Journal of Power Sources,* vol. 162, pp. 927-934, Nov 22 2006.

[2] A. Patil, V. Patil, D. W. Shin, J. W. Choi, D. S. Paik, and S. J. Yoon, "Issue and challenges facing rechargeable thin film lithium batteries," *Materials Research Bulletin,* vol. 43, pp. 1913-1942, Aug-Sep 2008.

[3] E. Stura and C. Nicolini, "New nanomaterials for light weight lithium batteries," *Analytica Chimica Acta,* vol. 568, pp. 57-64, May 24 2006.

[4] B. J. Landi, M. J. Ganter, C. D. Cress, R. A. DiLeo, and R. P. Raffaelle, "Carbon nanotubes for lithium ion batteries," *Energy & Environmental Science,* vol. 2, pp. 638-654, 2009.

[5] M. Conte, A. Iacobazzi, M. Ronchetti, and R. Vellone, "Hydrogen economy for a sustainable development: state-of-the-art and technological perspectives," *Journal of Power Sources,* vol. 100, pp. 171-187, Nov 30 2001.

[6] D. Wenger, W. Polifke, E. Schmidt-Ihn, T. Abdel-Baset, and S. Maus, "Comments on solid state hydrogen storage systems design for fuel cell vehicles," *International Journal of Hydrogen Energy,* vol. 34, pp. 6265-6270, Aug 2009.

[7] L. Alejo, R. Lago, M. A. Pena, and J. L. G. Fierro, "Catalytic partial oxidation of methanol: H-2 production for fuel cells," *3Rd World Congress on Oxidation Catalysis,* vol. 110, pp. 623-632, 1997.

[8] D. Browning, P. Jones, and K. Packer, "An investigation of hydrogen storage methods for fuel cell operation with man-portable equipment," *Journal of Power Sources,* vol. 65, pp. 187-195, Mar-Apr 1997.

[9] N. Edwards, S. R. Ellis, J. C. Frost, S. E. Golunski, A. N. J. van Keulen, N. G. Lindewald, and J. G. Reinkingh, "On-board hydrogen generation for transport applications: the HotSpot methanol reformer," *Journal of Power Sources,* vol. 71, pp. 123-128, 1998.

[10] B. Emonts, J. B. Hansen, S. L. Jorgensen, B. Hohlein, and R. Peters, "Compact methanol reformer test for fuel-cell powered light-duty vehicles," *Journal of Power Sources,* vol. 71, pp. 288-293, 1998.

[11] P. J. de Wild and M. J. F. M. Verhaak, "Catalytic production of hydrogen from methanol," *Catalysis Today,* vol. 60, pp. 3-10, Jul 10 2000.

[12] B. Lindstrom and L. J. Pettersson, "Hydrogen generation by steam reforming of methanol over copper-based catalysts for fuel cell applications," *International Journal of Hydrogen Energy,* vol. 26, pp. 923-933, Sep 2001.

[13] D. L. Trimm and Z. I. Onsan, "Onboard fuel conversion for hydrogen-fuel-cell-driven vehicles," *Catalysis Reviews-Science and Engineering,* vol. 43, pp. 31-84, 2001.

[14] J. D. Holladay, E. O. Jones, M. Phelps, and J. L. Hu, "Microfuel processor for use in a miniature power supply," *Journal of Power Sources,* vol. 108, pp. 21-27, Jun 1 2002.

[15] A. S. Patil, T. G. Dubois, N. Sifer, E. Bostic, K. Gradner, M. Quah, and C. Bolton, "Portable fuel cell systems for America's army: technology transition to the field," *Journal of Power Sources,* vol. 136, pp. 220-225, 2004.

[16] A. V. Pattekar and M. V. Kothare, "A microreactor for hydrogen production in micro fuel cell applications," *Journal of Microelectromechanical Systems,* vol. 13, pp. 7-18, Feb 2004.
[17] G. G. Park, S. D. Yim, Y. G. Yoon, C. S. Kirn, D. J. Seo, and K. Eguchi, "Hydrogen production with integrated microchannel fuel processor using methanol for portable fuel cell systems," *Catalysis Today,* vol. 110, pp. 108-113, Dec 15 2005.
[18] A. Kundu, J. H. Jang, H. R. Lee, S. H. Kim, J. H. Gil, C. R. Jung, and Y. S. Oh, "MEMS-based micro-fuel processor for application in a cell phone," *Journal of Power Sources,* vol. 162, pp. 572-578, Nov 8 2006.
[19] D.-E. Park, T. Kim, S. Kwon, C.-K. Kim, and E. Yoon, "Micromachined methanol steam reforming system as a hydrogen supplier for portable proton exchange membrane fuel cells," *Sensors and Actuators A - Physical,* vol. 135, pp. 58-66, 2007.
[20] J. D. Holladay, E. O. Jones, R. A. Dagle, G. G. Xia, C. Cao, and Y. Wang, "Miniaturization of a hydrogen plant," *Microreactor Technology and Process Intensification,* vol. 914, pp. 162-178, 2005.
[21] Y. Kawamura, N. Ogura, T. Yahata, K. Yamamoto, T. Terazaki, T. Yamamoto, and A. Igarashi, "Multi-layered microreactor system with methanol reformer for small PEMFC," *Journal of Chemical Engineering of Japan,* vol. 38, pp. 854-858, Oct 2005.
[22] J. Y. Won, H. K. Jun, M. K. Jeon, and S. I. Woo, "Performance of microchannel reactor combined with combustor for methanol steam reforming," *Catalysis Today,* vol. 111, pp. 158-163, Feb 15 2006.
[23] K. Yoshida, S. Tanaka, H. Hiraki, and M. Esashi, "A micro fuel reformer integrated with a combustor and a microchannel evaporator," *Journal of Micromechanics and Microengineering,* vol. 16, pp. S191-S197, Sep 2006.
[24] A. Mitsos, B. Chachuat, and P. I. Barton, "What is the design objective for portable power generation: Efficiency or energy density?," *Journal of Power Sources,* vol. 164, pp. 678-687, Feb 10 2007.
[25] K. R. Westerterp, "Multifunctional Reactors," *Chemical Engineering Science,* vol. 47, pp. 2195-2206, Jun-Aug 1992.
[26] J. R. Salge, B. J. Dreyer, P. J. Dauenhauer, and L. D. Schmidt, "Renewable hydrogen from nonvolatile fuels by reactive flash volatilization," *Science,* vol. 314, pp. 801-804, November 3, 2006 2006.
[27] G. A. Deluga, J. R. Salge, L. D. Schmidt, and X. E. Verykios, "Renewable hydrogen from ethanol by autothermal reforming," *Science,* vol. 303, pp. 993-997, Feb 13 2004.
[28] L. F. Brown, "A comparative study of fuels for on-board hydrogen production for fuel-cell-powered automobiles," *International Journal of Hydrogen Energy,* vol. 26, pp. 381-397, Apr 2001.
[29] C. E. Thomas, B. D. James, F. D. Lomax, and I. F. Kuhn, "Fuel options for the fuel cell vehicle: hydrogen, methanol or gasoline?," *International Journal of Hydrogen Energy,* vol. 25, pp. 551-567, Jun 2000.
[30] L. S. Wang, K. Murata, and M. Inaba, "Steam reforming of gasoline promoted by partial oxidation reaction on novel bimetallic Ni-based catalysts to generate

hydrogen for fuel cell-powered automobile applications," *Journal of Power Sources,* vol. 145, pp. 707-711, Aug 18 2005.

[31] M. Muller, C. Muller, F. Gromball, M. Wolfle, and W. Menz, "Micro-structured flow fields for small fuel cells," *Microsystem Technologies,* vol. 9, pp. 159-162, Jan 2003.

[32] G. W. Roberts, P. Chin, X. L. Sun, and J. J. Spivey, "Preferential oxidation of carbon monoxide with Pt/Fe monolithic catalysts: interactions between external transport and the reverse water-gas-shift reaction," *Applied Catalysis B-Environmental,* vol. 46, pp. 601-611, Nov 28 2003.

[33] S. Srinivas, A. Dhingra, H. Im, and E. Gulari, "A scalable silicon microreactor for preferential CO oxidation: performance comparison with a tubular packed-bed microreactor," *Applied Catalysis a-General,* vol. 274, pp. 285-293, Oct 28 2004.

[34] T. Kim, "Micro methanol reformer combined with a catalytic combustor for a PEM fuel cell," *International Journal of Hydrogen Energy,* vol. 34, pp. 6790-6798, Aug 2009.

[35] E. C. Wanat, K. Venkataraman, and L. D. Schmidt, "Steam reforming and water-gas shift of ethanol on Rh and Rh-Ce catalysts in a catalytic wall reactor," *Applied Catalysis a-General,* vol. 276, pp. 155-162, Nov 25 2004.

[36] Y. H. Wang and D. Y. Wu, "The experimental research for production of hydrogen from n-octane through partially oxidizing and steam reforming method," *International Journal of Hydrogen Energy,* vol. 26, pp. 795-800, Aug 2001.

[37] R. O. Idem and N. N. Bakhshi, "Production of Hydrogen from Methanol .1. Catalyst Characterization Studies," *Industrial & Engineering Chemistry Research,* vol. 33, pp. 2047-2055, Sep 1994.

[38] R. O. Idem and N. N. Bakhshi, "Production of Hydrogen from Methanol. 2. Experimental Studies," *Industrial & Engineering Chemistry Research,* vol. 33, pp. 2056-2065, 1994.

[39] B. A. Peppley, J. C. Amphlett, L. M. Kearns, and R. F. Mann, "Methanol-steam reforming on Cu/ZnO/Al2O3. Part 1: The reaction network," *Applied Catalysis a-General,* vol. 179, pp. 21-29, Apr 5 1999.

[40] M. P. Harold, B. Nair, and G. Kolios, "Hydrogen generation in a Pd membrane fuel processor: assessment of methanol-based reaction systems," *Chemical Engineering Science,* vol. 58, pp. 2551-2571, Jun 2003.

[41] N. G. Valente, L. A. Arrua, and L. E. Cadus, "Structure and activity of Sn-Mo-O catalysts: partial oxidation of methanol," *Applied Catalysis a-General,* vol. 205, pp. 201-214, 2001.

[42] C. S. Cao, G. Xia, J. Holladay, E. Jones, and Y. Wang, "Kinetic studies of methanol steam reforming over Pd/ZnO catalyst using a microchannel reactor," *Applied Catalysis a-General,* vol. 262, pp. 19-29, May 10 2004.

[43] K. Geissler, E. Newson, F. Vogel, T. B. Truong, P. Hottinger, and A. Wokaun, "Autothermal methanol reforming for hydrogen production in fuel cell applications," *Physical Chemistry Chemical Physics,* vol. 3, pp. 289-293, 2001.

[44] D. L. Damm and A. G. Fedorov, "Conceptual study of distributed CO2 capture and the sustainable carbon economy," *Energy Conversion and Management,* vol. 49, pp. 1674-1683, Jun 2008.

[45] S. Velu, K. Suzuki, M. P. Kapoor, F. Ohashi, and T. Osaki, "Selective production of hydrogen for fuel cells via oxidative steam reforming of methanol over CuZnAl(Zr)-oxide catalysts," *Applied Catalysis a-General,* vol. 213, pp. 47-63, 2001.

[46] J. Agrell, H. Birgersson, and M. Boutonnet, "Steam reforming of methanol over a Cu/ZnO/Al2O3 catalyst: a kinetic analysis and strategies for suppression of CO formation," *Journal of Power Sources,* vol. 106, pp. 249-257, Apr 1 2002.

[47] J. C. Amphlett, R. F. Mann, B. A. Peppley, and C. P. Thurgood, "A deactivation model for methanol-steam reformation on Cu/ZnO/Al2O3 catalyst for optimizing the production of fuel-cell hydrogen," *Catalyst Deactivation 2001, Proceedings,* vol. 139, pp. 205-212, 2001.

[48] M. V. Twigg and M. S. Spencer, "Deactivation of supported copper metal catalysts for hydrogenation reactions," *Applied Catalysis a-General,* vol. 212, pp. 161-174, Apr 30 2001.

[49] W. C. Shin and R. S. Besser, "Toward autonomous control of microreactor system for steam reforming of methanol," *Journal of Power Sources,* vol. 164, pp. 328-335, 2007.

[50] G. D. Stefanidis and D. G. Vlachos, "High vs. low temperature reforming for hydrogen production via microtechnology," *Chemical Engineering Science,* vol. 64, pp. 4856-4865, Dec 1 2009.

[51] M. Schuessler, M. Portscher, and U. Limbeck, "Monolithic integrated fuel processor for the conversion of liquid methanol," *Catalysis Today,* vol. 79, pp. 511-520, Apr 30 2003.

[52] L. Pan and S. Wang, "A compact integrated fuel-processing system for proton exchange membrane fuel cells," *International Journal of Hydrogen Energy,* vol. 31, pp. 447-454, 2006.

[53] B. Nair and M. P. Harold, "Hydrogen generation in a Pd membrane fuel processor: Productivity effects during methanol steam reforming," *Chemical Engineering Science,* vol. 61, pp. 6616-6636, October 2006 2006.

[54] S. G. Kandlikar, "Fundamental issues related to flow boiling in minichannels and microchannels," *Experimental Thermal and Fluid Science,* vol. 26, pp. 389-407, Jun 2002.

[55] A. V. Pattekar and M. V. Kothare, "A radial microfluidic fuel processor," *Journal of Power Sources,* vol. 147, pp. 116-127, Sep 9 2005.

[56] K. N. Theologos, A. I. Lygeros, and N. C. Markatos, "Feedstock atomization effects on FCC riser reactors selectivity," *Chemical Engineering Science,* vol. 54, pp. 5617-5625, Nov 1999.

[57] C. Mirgain, C. Briens, M. Del Pozo, R. Loutaty, and M. Bergougnou, "Modeling of feed vaporization in fluid catalytic cracking," *Industrial & Engineering Chemistry Research,* vol. 39, pp. 4392-4399, Nov 2000.

[58] W. W. Deng, J. F. Klemic, X. H. Li, M. A. Reed, and A. Gomez, "Liquid fuel microcombustor using microfabricated multiplexed electrospray sources," *Proceedings of the Combustion Institute,* vol. 31, pp. 2239-2246, 2007.

[59] D. C. Kyritsis, B. Coriton, F. Faure, S. Roychoudhury, and A. Gomez, "Optimization of a catalytic combustor using electrosprayed liquid hydrocarbons for mesoscale power generation," *Combustion and Flame,* vol. 139, pp. 77-89,

Oct 2004.
[60] J. R. Salge, G. A. Deluga, and L. D. Schmidt, "Catalytic partial oxidation of ethanol over noble metal catalysts," *Journal of Catalysis,* vol. 235, pp. 69-78, Oct 1 2005.
[61] J. M. Meacham, M. J. Varady, D. Esposito, F. L. Degertekin, and A. G. Fedorov, "Micromachined ultrasonic atomizer for liquid fuels," *Atomization and Sprays,* vol. 18, pp. 163-190, 2008.
[62] J. M. Meacham, M. J. Varady, F. L. Degertekin, and A. G. Fedorov, "Droplet formation and ejection from a micromachined ultrasonic droplet generator: Visualization and scaling," *Physics of Fluids,* vol. 17, pp. 1006051-1006058, Oct 2005.
[63] J. M. Meacham, C. Ejimofor, S. Kumar, F. L. Degertekin, and A. G. Fedorov, "Micromachined ultrasonic droplet generator based on a liquid horn structure," *Review of Scientific Instruments,* vol. 75, pp. 1347-1352, May 2004.
[64] B. S. Gottfried, C. J. Lee, and K. J. Bell, "Leidenfrost Phenomenon - Film Boiling of Liquid Droplets on a Flat Plate," *International Journal of Heat and Mass Transfer,* vol. 9, p. 1167, 1966.
[65] S. Zhang and G. Gogos, "Film Evaporation of a Spherical Droplet over a Hot Surface - Fluid-Mechanics and Heat Mass-Transfer Analysis," *Journal of Fluid Mechanics,* vol. 222, pp. 543-563, Jan 1991.
[66] H. Fujimoto and N. Hatta, "Deformation and rebounding processes of a water droplet impinging on a flat surface above leidenfrost temperature," *Journal of Fluids Engineering-Transactions of the Asme,* vol. 118, pp. 142-149, Mar 1996.
[67] S. Chandra and C. T. Avedisian, "Observations of Droplet Impingement on a Ceramic Porous Surface," *International Journal of Heat and Mass Transfer,* vol. 35, pp. 2377-2388, Oct 1992.
[68] R. S. Miller and J. Bellan, "Direct numerical simulation of a confined three-dimensional gas mixing layer with one evaporating hydrocarbon-droplet-laden stream," *Journal of Fluid Mechanics,* vol. 384, pp. 293-338, Apr 10 1999.
[69] S. R. Turns, *An Introduction to Combustion*, 2nd ed. Boston, MA: McGraw Hill, 2000.
[70] B. Abramzon and W. A. Sirignano, "Droplet Vaporization Model for Spray Combustion Calculations," *International Journal of Heat and Mass Transfer,* vol. 32, pp. 1605-1618, Sep 1989.
[71] W. A. Sirignano, "Fuel droplet vaporization and spray combustion theory," *Progress in Energy and Combustion Science,* vol. 9, pp. 291-322, 1983.
[72] A. L. Hines and R. N. Maddox, *Mass Transfer: Fundamentals and Applications*. Englewood Cliffs, NJ: Prentice-Hall, 1985.
[73] K. K. Varanasi, H. L. Clack, and R. S. Miller, "On preferential diffusion of binary component liquid droplets evaporating in a two-phase mixing layer," *International Journal of Multiphase Flow,* vol. 30, pp. 1235-1257, Oct 2004.
[74] E. Santacesaria and S. Carra, "Kinetics of catalytic steam reforming of methanol in a CSTR reactor," *Applied Catalysis,* vol. 5, pp. 345-358, 1983.
[75] Y. T. Choi and H. G. Stenger, "Kinetics, simulation and optimization of methanol steam reformer for fuel cell applications," *Journal of Power Sources,* vol. 142, pp. 81-91, Mar 24 2005.

[76] B. A. Peppley, J. C. Amphlett, L. M. Kearns, and R. F. Mann, "Methanol-steam reforming on Cu/ZnO/Al2O3 catalysts. Part 2. A comprehensive kinetic model," *Applied Catalysis a-General,* vol. 179, pp. 31-49, Apr 5 1999.

[77] K. P. Hapgood, J. D. Litster, S. R. Biggs, and T. Howes, "Drop penetration into porous powder beds," *Journal of Colloid and Interface Science,* vol. 253, pp. 353-366, Sep 15 2002.

[78] N. Alleborn and H. Raszillier, "Spreading and sorption of droplets on layered porous substrates," *Journal of Colloid and Interface Science,* vol. 280, pp. 449-464, Dec 15 2004.

[79] J. K. Lee, J. B. Ko, and D. H. Kim, "Methanol steam reforming over Cu/ZnO/Al2O3 catalyst: kinetics and effectiveness factor," *Applied Catalysis a-General,* vol. 278, pp. 25-35, Dec 28 2004.

[80] F. P. Incropera and D. P. DeWitt, *Fundamentals of Heat and Mass Transfer*, 5th ed.: John Wiley & Sons, 2002.

[81] E. G. Services, I. Parsons, and S. A. I. Corporation, "Fuel Cell Handbook," U. S. D. o. Energy, O. o. F. Energy, and N. E. T. Laboratory, Eds., 2000.

[82] T. Kim and S. Kwon, "Design, fabrication and testing of a catalytic microreactor for hydrogen production," *Journal of Micromechanics and Microengineering,* vol. 16, pp. 1760-1768, 2006.

[83] A. Mitsos, M. M. Hencke, and P. I. Barton, "Product engineering for man-portable power generation based on fuel cells," *Aiche Journal,* vol. 51, pp. 2199-2219, Aug 2005.

[84] V. Agarwal, S. Patel, and K. K. Pant, "H-2 production by steam reforming of methanol over Cu/ZnO/Al-2) catalysts: transient deactivation kinetics modeling," *Applied Catalysis a-General,* vol. 279, pp. 155-164, Jan 28 2005.

[85] N. S. Kaisare, J. H. Lee, and A. G. Fedorov, "Hydrogen generation in a reverse-flow microreactor: 2. Simulation and analysis," *Aiche Journal,* vol. 51, pp. 2265-2272, Aug 2005.

[86] S. H. Chan and H. M. Wang, "Thermodynamic and kinetic modelling of an autothermal methanol reformer," *Journal of Power Sources,* vol. 126, pp. 8-15, Feb 16 2004.

[87] D. L. Damm and A. G. Fedorov, "Batch Reactors for Hydrogen Production: Theoretical Analysis and Experimental Characterization," *Industrial & Engineering Chemistry Research,* vol. 48, pp. 5610-5623, Jun 17 2009.

[88] M. Kaviany, *Principles of Heat Transfer in Porous Media*, 2nd ed. New York: Springer-Verlag, 1995.

[89] J. H. Ferziger and M. Peric, *Computational Methods for Fluid Dynamics*, 3rd ed. Berlin: Springer-Verlag, 2002.